UC Berkeley
UC Berkeley Electronic Theses and Dissertations

Title
Single Nanowire Probe for Single Cell Endoscopy and Sensing

Permalink
https://escholarship.org/uc/item/9m28d2gd

Author
Yan, Ruoxue

Publication Date
2010

Peer reviewed|Thesis/dissertation

eScholarship.org Powered by the California Digital Library
University of California

Single Nanowire Probe for Single Cell Endoscopy and Sensing

By

Ruoxue Yan

A dissertation submitted in partial satisfaction of the

requirements for the degree of

Doctor of Philosophy

in

Chemistry

and the Designated Emphasis

in

Nanoscale Science and Engineering

in the

Graduate Division

of the

University of California, Berkeley

Committee in charge:

Professor Peidong Yang, Chair
Professor Angelica Stacy
Professor Xiang Zhang

Fall 2010

Single Nanowire Probe for Single Cell Endoscopy and Sensing

Copyright © 2010

by

Ruoxue Yan

Abstract

Single Nanowire Probe for Single Cell Endoscopy and Sensing

By

Ruoxue Yan

Doctor of Philosophy in Chemistry

and the Designated Emphasis in Nanoscale Science and Engineering

University of California, Berkeley

Professor Peidong Yang, Chair

The ability to manipulate light in subwavelength photonic and plasmonic structures has shown great potentials in revolutionizing how information is generated, transformed and processed. Chemically synthesized nanowires, in particular, offers a unique toolbox not only for highly compact and integrated photonic modules and devices, including coherent and incoherent light sources, waveguides, photodetectors and photovoltaics, but also for new types of nanoscopic bio-probes for spot cargo delivery and in-situ single cell endoscopy and sensing. Such nanowire probes would enable us to carry out intracellular imaging and probing with high spatial resolution, monitor in-vivo biological processes within single living cells and greatly improve our fundamental understanding of cell functions, intracellular physiological processes, and cellular signal pathways. My work is aimed at developing a material and instrumental platform for such single nanowire probe.

Successful optical integration of Ag nanowire plasmonic waveguides, which offers deep subwavelength mode confinement, and conventional photonic waveguides was demonstrated on a single nanowire level. The highest plasmonic-photonic coupling efficiency coupling was found at small coupling angles and low input frequencies. The frequency dependent propagation loss was observed in Ag nanowire and was confirmed by quantitative measurement and in agreement with theoretical expectations. Rational integration of dielectric and Ag nanowire waveguide components into hybrid optical-plasmonic routing devices has been demonstrated. This capability is essential for incorporating sub-100nm Ag nanowire waveguides into optical fiber based nanoprobes for single cell endoscopy.

The nanoprobe system based on single nanowire waveguides was demonstrated by optically coupling semiconductor or metal nanowire with an optical fiber with tapered tip. This nanoprobe design requires minimal instrumentation which makes it cost efficient and readily adaptable to average bio-lab environment. These probes are mechanically robust and flexible and can withstand repeated bending and deformation without significant deterioration in optical performance, which offers an ideal instrumental platform for out subsequent effort of using these nanoprobes in chemical sensing as well

as single cell endoscopy and spot delivery. Parameters affecting the coupling efficiency and output power of the nanoprobe were studied and chemical etched of single mode fiber with small cone angle was established to be optimized for highly effective optical nanoprobes.

The versatility of the nanoprobe design was first tested by transforming the nanowire probe into a pH sensor with near-field photopolymerization of a copolymer containing pH sensitive dye on the tip of the nanowire. The pH-sensitive nanoprobe was able to report the pH difference in micro-droplets containing buffer solution with the excitation of light waveguided on the nanoprobe with internal calibration, fast response time and good photostability and reversibility. Such nanoprobe sensors are ideal for high definition spatial and temporal sensing of concentration profile, especially for the kinetic processes in single cell studies for which chemical probes of minute sizes and fast response are desired.

The nanoprobe was then applied into spot cargo delivery and in-situ single cell endoscopy. It was demonstrated that nanowire-based optical probe can deliver payloads into the cell with a high spatiotemporal precision, guide and confine visible light into intracellular compartments selectively and detect optical signals from the subcellular regions with high spatial resolution. The nanoprobe was proven to be biocompatible and non-invasive. The effective optical coupling between the fiber optics and the nanowire enables highly localized excitation and detection, limiting the probe volume to the close proximity of the nanowire. None the less, this versatile technique does not rely on any expensive or bulky instrumentation, and relies only on micromanipulator and optical microscope that are readily available in most biological labs. The different functions can be further integrated to make the whole nanoprobe system more compact and even portable.

In addition, my research also includes the first demonstration of the synthesis of the longitudinal heterostructured SiO_2/Al_2O_3 nanotubes and the nanofluidic diode device based on the discontinuity of their internal surface charge. Comprehensive characterization shows that the nanotubes has heterostructured inner tube walls, as well as a discontinuity of surface charge. The ionic transport through these nanotube heterojunctions exhibits clear current rectification, a signature of ionic diode behavior. The development of such nanofluidic devices would enable the modulation of ionic and molecular transport at a more sophisticated level, and lead to large-scale integrated nanofluidic networks and logic circuits.

Table of Contents

Chapter 1
Introduction: Synthetic One-dimensional Photonic Nanostructures and Their Interface with Living Cells

Nanowires, by definition, typically have cross-sectional dimensions that can be tuned from 2 to 200 nm, with lengths spanning hundreds of nanometers to millimeters. These subwavelength structures represent a new class of semiconductor materials for investigating light generation, propagation, detection, amplification and modulation. After more than a decade of research, nanowires can now be synthesized and assembled with specific compositions, heterojunctions and architectures. This has lead to a host of nanowire photonic devices including photodetectors, chemical and gas sensors, waveguides, light emitting diodes (LEDs), microcavity lasers, solar cells and non-linear optical converters. A fully integrated photonic platform using nanowire building blocks promises advanced functionalities at dimensions compatible with on-chip technologies. Most recently, the interface between nanowires and living cells has also attracted intensive research interests. The small footprints of the nanowires insure their minimal invasiveness in cellular environment, yet their versatility in target cargo delivery, cross membrane optical communication and chemical/biological sensing offers a novel platform for understanding intercellular processes with high precision in both space and time domain.

This chapter provides an overview of the historic aspects of chemically synthesized nanowires, from III-V and II-IV semiconductor nanowires, to recently emerged metallic nanowires, as well as their rational synthesis, assembly, novel photonic properties, and biological applications.

1.1 **Development of Nanowire Photonics - An Overview**

Photonics involves the control of photons in free space or in matter. Manipulation of photons in semiconductor bulk crystals and thin films has culminated with breakthroughs like light emitting diodes and lasers. The continuing success of photonic technologies relies on the discovery of novel optical materials and miniaturization of the optoelectronic devices that feature better performance, low cost, and low power consumption. For the past few decades, worldwide efforts in nanomaterials research has led to a rich collection of nanostructures where size, shape and composition can be readily controlled. Many of such nanostructures exhibit fascinating optical properties that could have significant impact in the future of the photonic technology.

1.1.1 Semiconductor Nanowires

Quantum dots, which are the classical example of semiconductor nanostructures, exhibit tunable optical properties. As size of the quantum dots decreases, the bandgap would increase due to the quantum confinement, and the quantum dots exhibit blue-shifted light emission. These 3-dimensionally confined nanostructures have been actively explored for the development of new light-emitting and biological-imaging technologies[1]. However, since the 1990s another important class of semiconductor nanostructures has emerged; structures with cross-sections between 2-200 nm and lengths of several micrometers and longer. They were initially called "nanowhiskers"[2], and later popularized as "nanowires"[3]. Different from quantum dots, these structures are confined only in two dimensions allowing electrons, holes or photons to propagate freely along the third dimension. The large aspect-ratio of these new semiconductor nanostructures has brought forth the ability to bridge the nanoscopic and macroscopic world. This nano-macro interface is central for integrating nanoscale building blocks for electrical or optoelectronic device applications. Conventional photonic platforms often consist of large aspect-ratio features such as interconnects and waveguides, typically with micrometer dimension. Thus, as semiconductor nanowires emerged they were immediately recognized as one of the essential building blocks for nanophotonics.

Since their first introduction in 1990s, semiconductor nanowires have been extensively studied and much insight has been gained on tuning their electrical and optical properties by controlling their size and dimensions. In addition, the one-dimensional nature of a nanowire permits material synthesis in traditionally inaccessible compositional regions, which has been recently demonstrated in single crystalline InGaN nanowires with tunable bandgap from UV to NIR[4]. Such nanowires with tunable electronic structures hold great promise in photovoltaics, solid state lighting as well as solar-to-fuel energy conversion. Today, growth techniques for semiconductor nanowires have advanced to a level where desired composition, heterojunctions and architectures can be readily synthesized. The assortment of 1-dimensional nanostructured optoelectronic devices includes photodetectors, chemical and gas sensors, waveguides, non-linear optical converters, light emitting diodes (LEDs) and microcavity lasers.

1.1.2 Metal Nanowires

A recent addition to the nanowire-based photonic tool-box is metal, or "Plasmonic" nanowires. Plasmonics is a subfield of nanophotonics which is primarily concerned with the manipulation of light at the nanoscale, based on the properties of propagating and localized surface plasmons, which are defined as the collective oscillations of the electron gas in a conductor. Optical waves can couple to these electron oscillations in the form of propagating surface waves or localized excitations, depending on the geometry. Much like the optical modes of a conventional dielectric fiber, a broad continuum of SPP modes can be confined on a metallic wire and guided along the wire axis[5,6]. However, as opposed to dielectric waveguides[7], of which the diffraction limit constrains the dimension to be larger than about $\lambda/2$ (where λ is the wavelength, giving dimensions of about 750 nm for telecommunications applications), thin metal wires can maintain propagation of

SPP modes localized to dimensions comparable to the wire diameter d, even when it is much smaller than the optical wavelength λ. Therefore, SPPs represent one of the most promising structures for next-generation nanoscale photonic applications such as light-on-a-chip.

Over the last decade, various metal structures have been explored for plasmon propagation. Optical excitation of one dimensional plasmon propagation at the metal–air interface of a thin metal strip was achieved with grating coupler or attenuated total reflection (ATR) coupler. Scattering of the plasmons at holes or ordered nanoparticle arrays acting as local defects enables guiding of the plasmons[8,9]. These Plasmonic waveguides, although maintains highly confined electromagnetic field dictated by the SPP modes, suffers from high inherent losses and short propagation lengths. Insulator–metal–insulator (IMI) waveguides, where a long, thin metal stripe is sandwiched between two insulator layers, has been demonstrated to have remarkably long propagation lengths due to long-range surface plasmon (LRSP) modes[10-14]. However, this low propagation loss of LRSP is associated with low spacial mode confinement, therefore it is not as useful for the purpose of subwavelength photonic integration. On the other hand, the reverse geometry of IMI – Metal-insulator-metal (MIM) waveguides, where a long, thin insulator stripe is sandwiched between two metal layers, has exhibited superior special confinement compared to IMI waveguide[15-17]. However, it still remains a fundamental challenge for the MIM structure to achieve deep two-dimensional subwavelength confinement without substantial sacrifice of the propagation length[18].

In this context, synthetic metal nanowires offer a unique opportunity for developing nanoscale plasmonic waveguides due to their two-dimensional sub-100nm mode confinement and lower inherent losses compared to fabricated metal structures. Plasmon propagation in chemically synthesized gold and silver nanorods and nanowires of as low as 25 nm in diameter has been achieved, with a much improved propagation compared to thin-film based metal stripes of the similar dimensions[5,19-21]. Similar to light propagation in optical fibres, plasmon propagation is not limited to a straight line, but electromagnetic radiation contained in the plasmon can be bent and split using appropriate plasmonic structures[5]. These observations show the great opportunity to manipulate plasmons in the same way that light has been manipulated in optics, but using much smaller components. Moverover, the mechanical strength and flexibility of chemically synthesized metal nanowires, paired with the ease for surface functionalization, enables them to be fabricated into free-standing plasmonic probes/sensors in physiological environment for intercellular imaging, targeting and sensing.

1.2 **Rational Synthesis of Nanowires**

1.2.1 Synthesis of Semicondutor Nanowires

The creation of seminconductor nanowires through a bottom-up approach is heavily dependent on the controlled synthesis of one-dimensional, single-crystalline, high optical-quality materials. The “Vapor-Liquid-Solid” (VLS) growth, which promotes the seeding and oriented growth by introducing a catalytic liquid alloy phase which can

rapidly adsorb a vapor to supersaturation levels, has achieved the most success in producing various semiconductor nanowires in relatively large quantities. Originally proposed by Wagner and coworkers at Bell lab in the early 1960's[22] to explain gas phase silicon whisker growth in the presence of a liquid gold droplet, the VLS growth mechanism has been re-examined and developed over the past two decades by Lieber[23,24], Yang[25], Samuelson[26] and many other research groups. In the early 1990s, III-V "nanowhiskers" were synthesized and investigated by scientists at Hitachi[2]. Recent advances in both physical[23] (laser ablation, thermal evaporation) and chemical deposition techniques (chemical vapor transport and deposition, and metal-catalyzed molecular beam epitaxy) has allowed the development of a broad range of inorganic nanowire compositions (e.g. Si, Ge, ZnO, CdS, GaN, GaAs, InP), including group IV[27,28], II-VI[29,30], and III-V[31,32] compound and alloy crystal structures.[4,33,34] It is also worth mentioning that the Buhro group was able to grow III-V nanowires in a solution using a similar solution-liquid-solid process[35].

Understanding of the VLS mechanism led to nanowire growth with precise control over nanowire length, diameter, growth direction[36], morphology and composition. Nanowire diameter, typically from several nanometers to several hundred nanometers, is determined by the size of the metal alloy droplets. The length of these nanowires can be easily controlled from micrometers up to millimeters. Consequently, nanowire arrays with uniform size can be readily obtained by using monodispersed metal nanoparticles[37]. Precise orientation control during nanowire growth can be achieved by applying conventional epitaxial crystal growth techniques to this VLS process, known as vapor-liquid-solid epitaxy (VLSE). This VLSE process is particularly powerful in controlled synthesis of high quality nanowire arrays and single wire devices[38]. For example, highly oriented ZnO and GaN nanowire arrays can be epitaxially grown off a properly selected substrate such as sapphire and $LiAlO_2$ (Figure 1.1 A, B) [36,39]. A similar level of growth control has been achieved for III-V systems. Early work at Hitachi demonstrated good positional control of InAs and GaAs nanowires[40,41] through metal thin film patterning. Within the past 10 years, great progress has been made in elucidating fundamental III-V nanowire growth mechanism[42,43] as well as precise positional control of nanowire growth using advanced lithography processes. Recent work, notably from the groups at Lund University and Philips Research Laboratories, has shown beautifully the growth of highly ordered array of III-V nanowires with different compositions[44] (Figure 1.1 C). Importantly, due to the nature of free-standing nanowire growth, these nanowires and their heterojunctions are usually dislocation free and can readily accommodate large lattice mismatches unlike thin film growth[45]. Therefore, semiconductor nanowire growth also enables direct integration of optically active semiconductors (e.g. III-V compounds) onto silicon substrates[46-49]. This capability represents a significant advantage over conventional thin film technology.

While vapor-liquid-solid process has been very successful in making semiconductor nanowires of various compositions, the use of metal in the growth process inevitably introduces a potential problem of contamination. This has been a key concern when considering nanowire technologies for large scale optoelectronics industry. To mitigate

this problem, efforts have been devoted towards nanowire growth without using metal particles or thin films[50]. For example, the team at Hokkaido University has used selective-area metalorganic vapor phase epitaxy (SA-MOVPE) to grow ordered arrays of III-V nanowires and their heterojunctions (Figure 1.1 D)[51-53]. This is a metal catalyst-free process, and therefore effectively avoids the metal contamination issue.

Another important task in semiconductor nanowire synthesis is the precise control and full-range tunability over the composition of doped and alloyed nanowires, which are of particular interest due to their potential applications in high efficiency solid-state lighting and photovoltaics. Recent progress in our group has demonstrated broad tunability in nanowire synthesis for systems that traditionally endure inevitable phase separation in bulk and thin film forms, due to the ability of the nanowire morphology to accommodate strain-relaxed growth. As shown in (Figure 1.1 D, E), single-crystalline $In_xGa_{1-x}N$ nanowires has been synthesized across the entire compositional range from $x = 0$ to 1 by low-temperature halide chemical vapor deposition and were shown to have tunable emission from the near-ultraviolet to the near-infrared region[4].

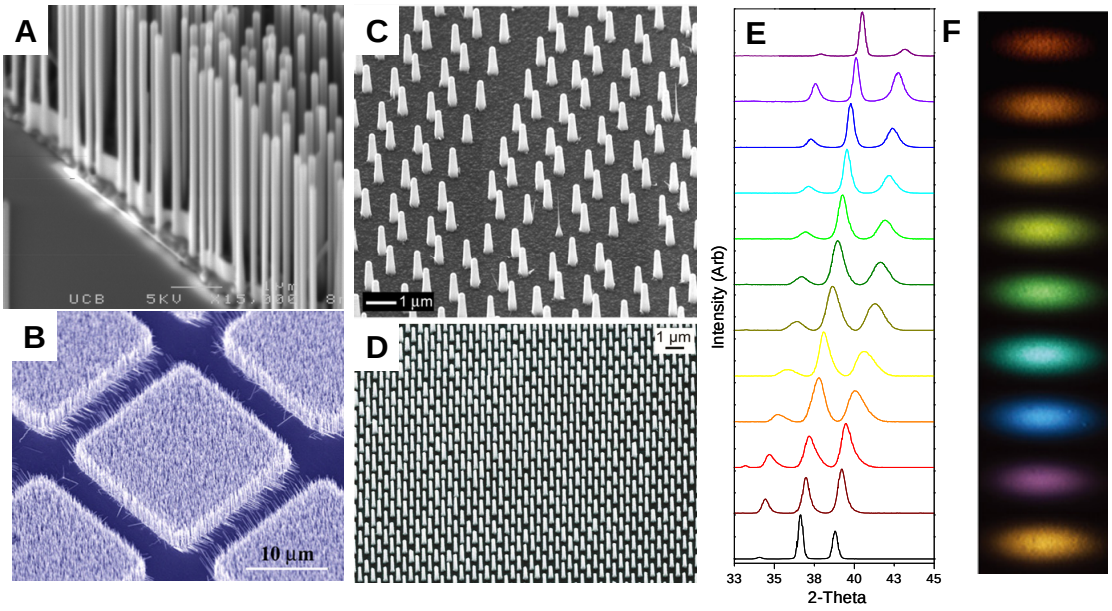

Figure 1.1 Scanning electron microscopy (SEM) images of ZnO **(A)**, GaN **(B)**, InP **(C)** and InP/InAs/InP core-multishell **(D)** nanowire arrays. **(E),** X-ray diffraction (XRD) for InGaN nanowires with different In concentration. **(F)** CCD camera image of the visible photoluminescence (PL) emission of $In_xGa_{1-x}N$ nanowire (x=0-0.6).

Yet another critical breakthrough in the development of nanowire building blocks is the controlled growth of nanowire heterostructures, including co-axial[54-57] and longitudinal variation[58-61](Figure 1.2 A-B). Typically, direct overgrowth on nanowire side surface leads to co-axial heterostructures while sequential nanowire VLS growth produces longitudinal heterostructures. The ability to form diverse heterostructures sets nanowires apart from other nanomaterials, such as quantum dots and carbon nanotubes, and

represents a substantial advantage for the development of increasingly powerful and unique nanoscale electronic and optoelectronic devices[62]. Finally, highly controlled architecture modulation can also be realized via the VLS growth mode to form complex branching structures. For example, single crystalline GaP 'nanotrees' can be grown through a sequential-seeding technique where each level of branching is controlled in terms of branch length, diameter and density[63]. More recently, it was discovered that highly branched PbS nanowires (Figure 1.2 C) can be readily synthesized through a dislocation-driven growth mechanism using a simple chemical vapor transport setup[64,65].

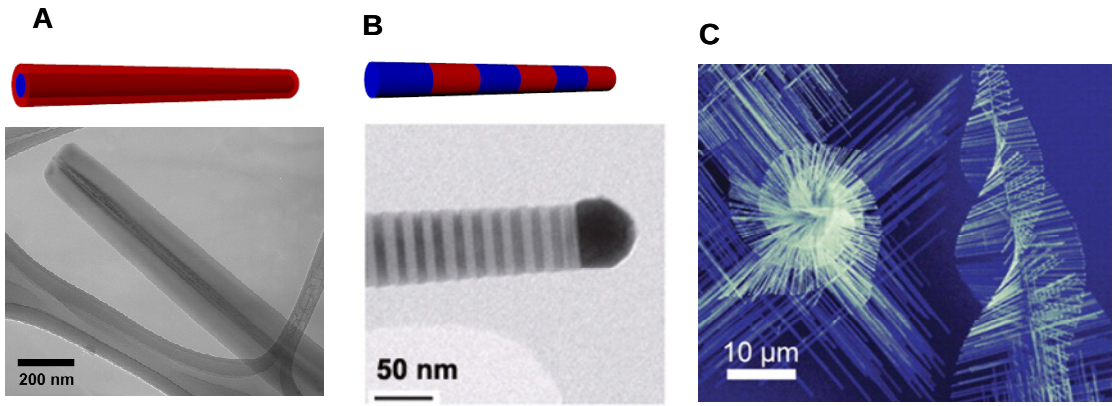

Figure 1.2 A, TEM image of a GaN/AlGaN core-sheath nanowire. **B,** TEM image of a InP superlattice nanowire. **C,** SEM image of PbS highly branched nanowires.

1.2.2 Synthesis of Plasmonic Nanowires

All metal nanowires are capable of supporting surface plasmons, however, silver nanowire is most technologically significant, because it has the lowest ohmic loss and longest propagation length, which is the most important prerequisite for high efficiency plasmonic waveguide, and its plasmonic resonance is close to optical frequencies, so that the optical excitation of its SPP modes would be relatively easy. However, the 1D growth of silver nanowire was challenging due to the isotropic nature of its cubic crystal symmetry. The synthesis of single crystalline Ag nanowires was first realized through templated solution process. Ordered silver nanowire arrays have been obtained by electro- or chemical deposition in self-ordered porous membranes such as anodized alumina membrane[66,67] and polycarbonate membranes[68] (Figure 1.3A and B). The diameters and lengths of these templated Ag nanowires can be controlled by varying the pore size and thickness of the alumina membrane. Although the nanowires synthesized using this method are usually polycrystalline, single crystals has also been obtained, nevertheless, they contain a certain extent of lattice defects such as twin boundaries and stacking faults, as well as relatively rough surfaces.

A template-less polyol method that generated bicrystalline Ag nanowires was developed by Xia and co-workers by reducing silver ion with ethylene glycol in the presence of poly(vinyl pyrrolidone) (PVP)[69-71] (Figure 1.4 A). PVP acted as a polymeric capping reagent to aid the 1D growth of the Ag nanowire with uniform diameters of 30-60 nm and lengths up to 50 µm, which can be further adjusted in a larger range by modifying the

seeding parameter and the growth temperature and duration. The resultant Ag nanowires have high crystal quality and atomically smooth surface (Figure 1.4 B and C), yielding them ideal for constructing low-loss integratable plasmonic waveguides.

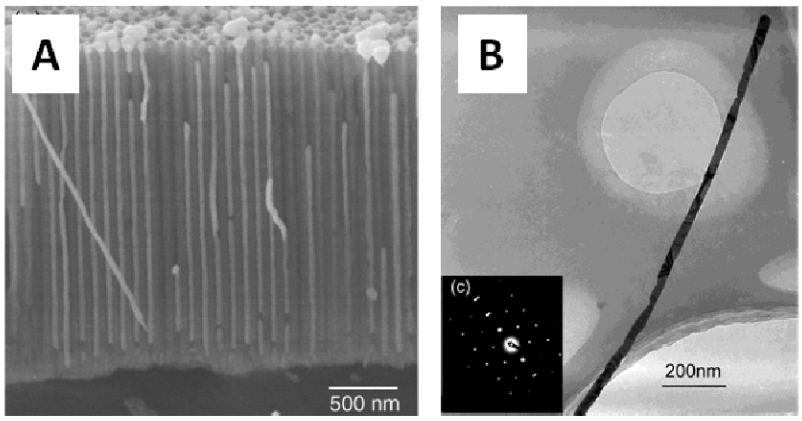

Figure 1.3 A, Side view SEM image of Ag of a silver-filled alumina membrane. **B,** TEM image and selected-area electron diffraction (SAED) pattern of an individual Ag nanowire after removing AAM.

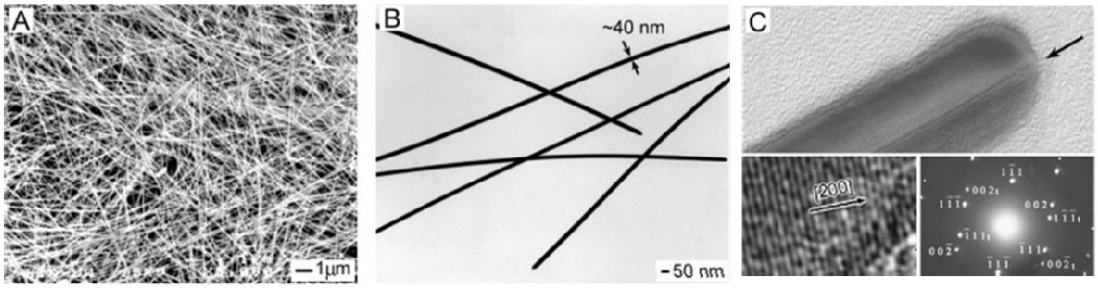

Figure 1.4 SEM **(A)** and TEM **(B)** images of Ag nanowire that were synthesized by polyol method at 160°C. **C,** High-resolution TEM image of the end of an individual nanowire, with the arrow indicating a twin plane parallel to its long axis. The inset shows the corresponding convergent-beam electron diffraction pattern.

1.3 **Nanowire Assembly with Optical Means**

Although a high level of composition and orientation control in semiconducting nanowires can be achieved by epitaxial growth, assembling these nanowires into highly integrated and functional two- or three-dimensional heterogeneous material systems with high spatial and angular precision remains a major challenge and relies heavily on post-synthesis integration of various nanowires. At present, several post-synthesis nanowire assembly techniques have been investigated, including using electric[72] and magnetic fields, laminar flow in microfluidic channels[73,74], Langmuir–Blodgett compression[75,76] and microcontact printing[77]. Although these techniques opened up the possibility to organize and align macroscopic arrays of nanowires, they lack the ability to address single nanostructures, and then to position them with arbitrary precision. The

three-dimensional manipulation of single nanowires remains an active area of research in nanowire assembly. Direct manipulation of nanowires in a liquid medium is even more challenging.

One possible solution is to manipulate nanowires with "optical traps" or "optical tweezers" – tightly focused laser beams capable of holding and moving microscopic dielectric objects in three-dimensions. Since their introduction in 1986[78], the optical tweezer has become an important tool for the manipulation of objects ranging in size from tens of nanometers to tens of micrometers[79]. Optical trapping is especially appealing for nanowire manipulation and integration since it can be carried out directly in a liquid medium with high spatial positioning accuracy (< 1 nm)[80]. Recent work with a focused infrared single-beam optical trap has shown that it is possible to optically trap, transfer and assemble high-aspect-ratio semiconductor nanowires into arbitrary structures at room temperature, at both physiological pH and ionic strength[81]. A schematic of the assembly procedure is shown in Figure 1.5A-B. Further precision-controlled nanowire arrangements, in 2- and 3-dimensions, have been demonstrated by holographic optical trapping[82]. Using these methods, complex and robust nanowire structures functioning as active photonic devices can be constructed in physiological environments (Figure 1.5C), thereby offering new forms of chemical, mechanical and optical probes in studying living cells.

Equally important to the precision control of nanowire assemblies is the massive parallel differentiation and manipulation of individual nanowires with arbitrary composition. In this context, optoelectronic tweezers[83] (OET) have emerged as a powerful tool for addressing individual semiconducting and metallic nanowires with diameters less than 20nm through optically induced dielectrophoresis (DEP) force[84]. Compared to optical tweezers, optoelectronic tweezers operates at an optical power density that is orders of magnitude lower, transports individual nanowires with much greater speed and are capable of addressing multiple nanowires simultaneously. Maximum trapping speeds for an individual silicon nanowire with 100-nm diameter and 5-μm length approach 135 μm/s with a peak-to-peak trapping voltage of 20 V. This is approximately four times the maximum speed achievable by optical tweezers and is reached with 5–6 orders of magnitude less optical power density than optical tweezers. Figure 1.5D-F shows the schematic OET device structure with an individual nanowire trapped at the laser spot and a large array of silver nanowires assembled with traps created by photopatterned virtual electrodes. Adding to the merits of an OET is the ability to separate semiconducting and metallic nanowires, which suggests a broad range of applications for the separation and heterogeneous integration of one-dimensional nanoscale materials. In order to realize the integration of nanowires into large scale optoelectronic devices and systems, assembly techniques that are scalable, massively parallel, low-cost, and high through-put must be developed. In particular, addressability and precise registration of individual features within a multi-layer optoelectronic platform remains to be challenging. This is also believed to be one of the potential road blocks that would dictate whether any of the nanowire electronic or optoelectric technologies could eventually be commercially viable.

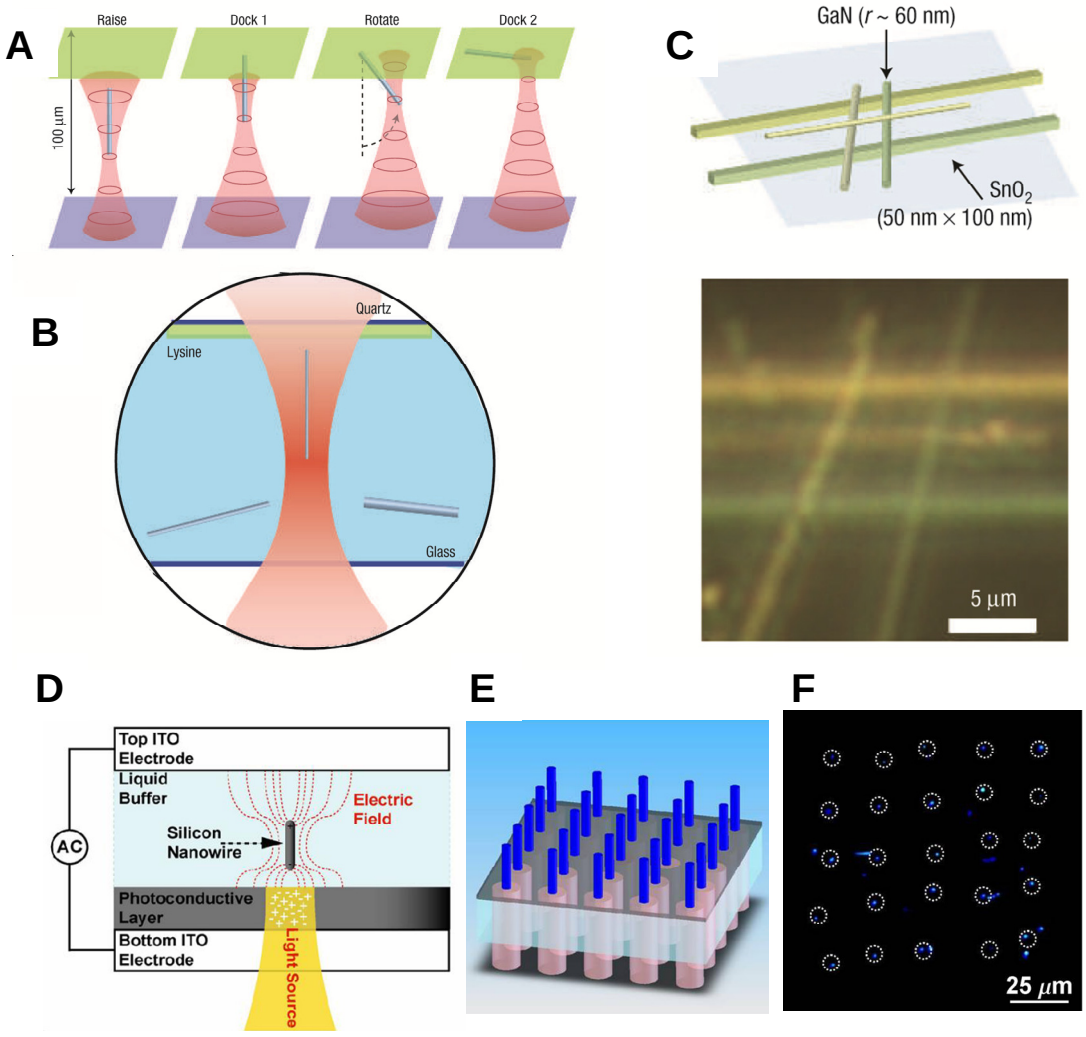

Figure 1.5 A, Schematic of optical trapping procedure for nanowire docking at a surface. **B,** Schematic of experimental chamber cross section. The top surface consists of a fused silica coverslip (blue) coated with lysine or gold (green). The bottom surface consists of a rectangular glass coverslip. Due to gravity, free nanowires sink to the bottom surface, where they can be picked up with the optical trap. **C,** Schematic (top) and optical darkfield image (bottom) of a three dimensional nanowire assembly consisting of SnO_2 nanoribbons and GaN nanowires in a fluid chamber. **D,** Optoelectronic Tweezer (OET) device structure with an individual nanowire trapped at the laser spot (ITO, indium tin oxide). Typical laser intensity used here is about 100 W/cm^2. **E and F,** A 5X5 single silver nanowires array formed using traps created with a digital micromirror spatial light modulator and positioned with a computer-mouse-controlled graphical user interface.

1.4 **Nanowire Laser/LEDs**

Inorganic semiconductor nanowires represent one class of important nanostructures as optical gain media that could potentially outperform their thin film counterpart. The unique characteristics of semiconductor nanowires, such as one-dimensional geometry, dislocation-free single crystalline nature, high index of refraction, and atomically smooth surface, allow for sufficient end-facet reflectivity, and photon confinement in a volume of just a few cubic wavelengths of material. To date, optically pumped coherent laser emission has been detected from a number of different nano-cavities of binary semiconductors, including ZnO (λ~385nm) epitaxial arrays[39], combs[85], tetrapods[86], single nanowires and nanoribbons[87], ZnS (337 nm)[88] nanoribbons, CdS (490 nm)[89], GaN (380 nm)[90] and GaSb (1550 nm)[91] nanowires, and GaN ring resonators[92]. Nanowire lasing under optical pumping was first observed in ZnO by the Yang group[39]. Since then nanowire photonics has branched into a flurry of research avenues. Well-faceted nanowires with diameters from 100 nm to 500 nm support predominantly axial Fabry-Perot waveguide modes (separated by $\Delta\lambda = \lambda^2/[2Ln(\lambda)]$ (Figure 1.6A), where L is the cavity length and $n(\lambda)$ is the group index of refraction). Significant scattering loss prevents smaller wires from lasing. The large refractive index difference between the semiconductor material and its surrounding dielectric environment enables the photonic confinement in the nanowire cavities. These structures act as waveguides for specific axially guided modes and provide sufficient resonant feedback for low gain threshold values and high quality factors. Hence, modal gain in nanowire can be achieved and the nanowires can serve as excellent resonant cavities for light amplification. Typical output of an optically-pumped single ZnO nanowire laser was recently measured to be several tens of microwatts[93]. By placing these nanowires in external cavities such as photonic crystals[94] or fabricating distributed Bragg reflectors with high reflectivity, it is possible to further reduce their lasing threshold. Far-field imaging indicates that PL and lasing emission are localized at the ends of nanowires, which suggests strong waveguiding behavior that is consistent with axial Fabry-Perot modes (Figure 1.6B). Theoretical simulation of the nanowire far field emission predicts that the angular emission intensity of these nanowire lasers is highly dependent on the mode type within (i.e. TE, TM or HE[95]). Analysis of interference pattern[96] from the wire end facets suggests that the nanowire laser emission might be non-directional. This is in contrast with macroscopic lasers, where directional emission is expected.

Beyond nanowire lasers, confined core-sheath nanowire heterostructures provide a unique geometry for applications in optoelectronics. Quantum confinement has measurable effects if the diameter of the gain medium is reduced in size below the Bohr exciton radius of the semiconductor. Effective carrier/exciton confinement has been demonstrated for a core-sheath GaN/AlGaN heterostructure (Figure 1.2A), in which the active GaN material has a diameter as small as 5 nm, and is surrounded by a thick sheath of $Al_{0.75}Ga_{0.25}N$ with a larger bandgap and lower refractive index[54], creating a structure with simultaneous exciton and photon confinement (waveguiding). When optically pumped, the core provides a gain medium while the sheath acts as a Fabry-Perot optical cavity. Recently, room temperature tunable lasing has been demonstrated in multi-quantum-well (MQW) core/shell nanowire heterostructures[56] (Figure 1.6C). The

co-axial heterostrucutrue consists of a GaN nanowire core, which functions as the primary part of the optical cavity, and epitaxial InGaN/GaN MQW shells, which serve as the composition-tunable gain medium. Optical excitation of individual MQW nanowire structures yielded lasing with InGaN quantum-well composition-dependent emission from 365 to 494 nm (Figure 1.6D). Similarly, NIR lasing has also been demonstrated in GaAs/GaAsP coaxial core-shell nanowires[97-99]. However, realization of a reliable, electrical injected nanowire nanolaser remains to be one of the major challenges due to issues such as nanoscale metal-semiconductor contacts. Other technical difficulties also include high gain heterojunction or multiple quantum wells formation within single nanowires and effective surface passivation to eliminate undesirable recombination pathways. It is also not clear at this point what would be the best approach to integrate these nanowire gain materials with a low-loss cavity design. Electrically injected nanowire nanolasers could offer many benefits such as low threshold current, low power consumption, large-scale integration, and fast modulation bandwidth. And since their footprints are comparable to electronic transistors, they are attractive for intra-chip optical interconnect applications.

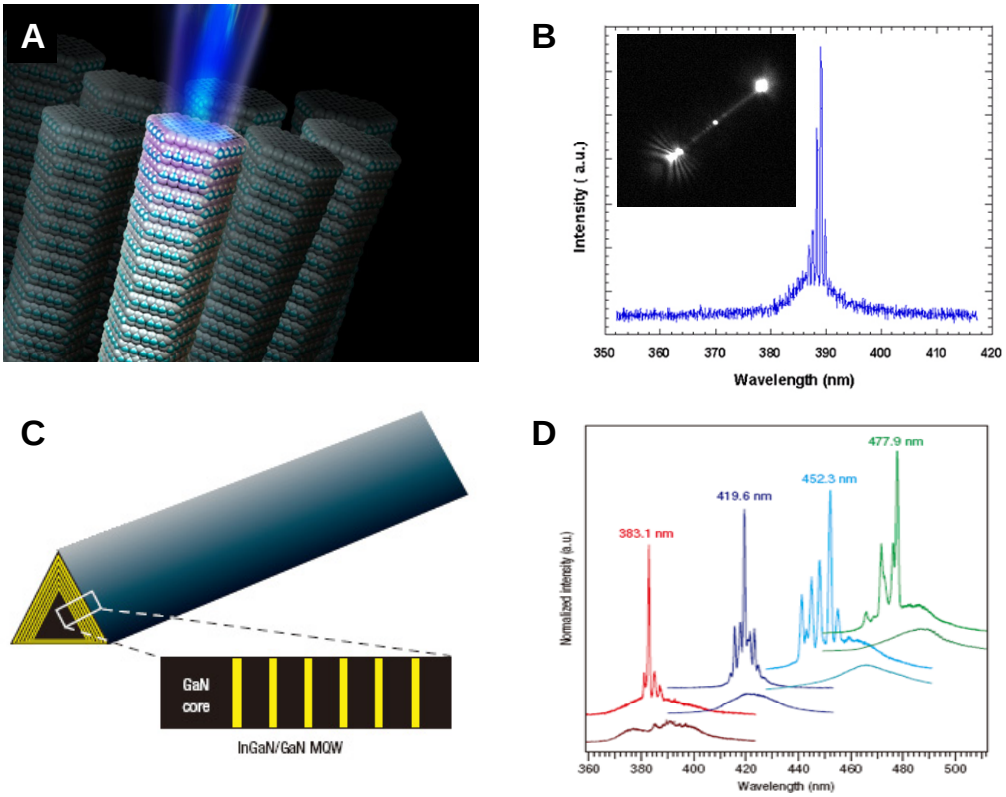

Figure 1.6 A, Schematic of an optically pumped nanowire laser cavity. **B,** Lasing spectrum from an individual ZnO nanowire, inset is the far-field optical image of a lasing GaN nanowire. **C,** Schematic diagram of an MQW nanowire and magnified cross-sectional view of a nanowire facet highlighting InGaN/GaN MQW structure. The InGaN layer is indicated in yellow color. **D,** Normalized lasing spectra collected from 4 representative MQW nanowire structures with increasing indium composition pumped at ~250 kW cm^{-2} and~700 kW cm^{-2}, respectively.

In addition to optically pumped nanowire lasers, electrically driven spontaneous emission has also been realized in nanowire-based light-emitting diodes (LEDs), which require the crossing of a p-type and n-type nanowire or the simultaneous electrical contacts to both the p- and n- part of an individual heterostructured nanowire. The first example of nanowire LED was demonstrated using the vertical GaAs pn-junction arrays by the Hitachi team. To date, nanowire LEDs have been successfully realized in a variety of cross-nanowire junctions[88,100-102], longitudinal[103] and co-axial heterostructures[55] with electroluminescence (EL) emission ranging from near infra-red to ultraviolet. In particular, multicolor LED has been fabricated on a single substrate by contacting different n-type nanowires, including GaN (UV), CdS (green), and CdSe (near infrared), with Si nanowire or lithographically patterned Si strips as a common p-type material[101], enabling easy interfacing with conventional silicon microelectronics.

1.5 **Nanowire Waveguides and Non-linear Optical Mixing**

In the previous sections, we have discussed the synthesis and assembly of semiconductor nanowires, and the promising developments of these chemically synthesized nanowires into nanoscale light sources (lasers and LEDs). However, to perform logic operations including computing, communication, and sensing in future integrated photonic circuits, photons generated by these nanowire light sources must be efficiently captured and precisely delivered to other nanowire optical components that assume various functions such as photodetectors, frequency converters, filters and switches. The development of nanowire subwavelength waveguides is an important step towards on-chip routing of optical signals to carry out these complex tasks. In contrast to lithographically-defined waveguides, chemically synthesized binary oxide nanowires have several features that make them viable photonic waveguides, including inherent one-dimensionality, single crystallinity, large refractive index, low surface roughness, high flexibility, large material diversity and, in principle, the ability to operate both above and below the diffraction limit.

Among available oxide nanowires, tin dioxide (SnO_2) nanoribbons have proven to be excellent subwavelength waveguides[104]. A nanoscale mimic of a conventional fiber optic, the high refraction index (n=2.1) SnO_2 nanoribbon with typical dimensions between 100 and 400 nm, can efficiently guide both its own visible photoluminescence and visible/UV emissions from other nanowires and fluorophores. Losses ranged from 1 to 8 dB mm^{-1} for wavelengths between 450 and 550 nm, depending on ribbon cross-sectional area. These values are higher than those for conventional optical fibers, but is sufficient for integrated planar photonic applications such as short-distance on-chip signal routing and distribution. For example, optical linkages between active nanowires (GaN and ZnO) and passive nanowires (SnO_2) can be formed via tangential evanescent coupling (Figure 1.7A-B).

Adding to the versatility of SnO_2 nanoribbon waveguides is that they are excellent short-pass filters that exhibit different cut-off wavelengths depending on their cross-section. For example, cross-sectional dimensions of the 465, 492, 514, 527, and 580 nm nanowire filters are 310 nm by 100 nm (0.031 μm^2), 280 nm by 120 nm (0.034 μm^2),

350 nm by 115 nm (0.040 μm^2), 250 nm by 225 nm (0.056 μm^2), and 375 by 140 nm (0.052 μm^2), respectively. Therefore, nanoribbons of different cut-off frequencies can be integrated with a common multi-mode core waveguide ribbon to produce an optical router based on input color. Assemblies such as multi-branched hubs and grids have already been implemented in nanowire-based electronic logic, which suggests that similar nanowire architectures could be potentially used in integrated optical logic[105] and all-optical switching[106].

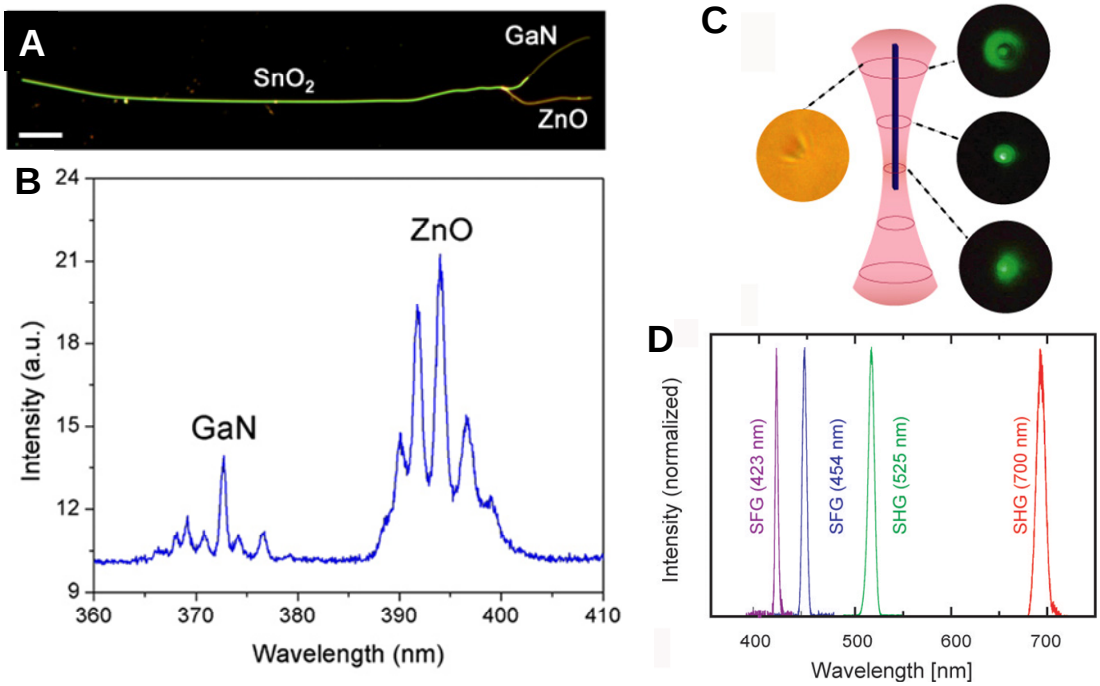

Figure 1.7 A, Dark-field image illustrating the coupling geometry of two nanowire lasers (GaN and ZnO) to a common SnO_2 nanoribbon waveguide. Scale bar=25 μm. **B,** Spectra recorded at the left terminus of the SnO_2 nanoribbon after simultaneous nanowire laser injection at the right terminus. Both laser pulses are guided through the SnO_2 waveguide and emerge as two resolvable packets (dictated by their band gaps) of modes. **C,** Bright field (left) and SHG (right) images of an optically trapped single $KNbO_3$ nanowire. Waveguiding of the SHG signal (green) leads to diffraction rings at the distal (top) end of the nanowire which acts as a subwavelength aperture. **D,** Panchromatic wavelengths generated by the nonlinear optical processes (SHG & SFG) within individual $KNbO_3$ nanowires. It shows SFG signals (λ= 423 nm, 454 nm with 800/900 nm and 800/1050 nm fundamental beams respectively) and SHG signals (λ= 525 nm, 700 nm), obtained from a single $KNbO_3$ nanowire by introducing fundamental beams at a variety of different frequencies via the tunable femtosecond pump.

One additional advantage that semiconductor nanowires have over their silica counterpart[107] is their ability to efficiently guide light in water and other liquid media due to their higher refractive index[108]. This becomes especially important if these nanowires need to be interfaced with liquid media for on-chip chemical or biological spectroscopic analysis. An even more daunting task is the development of a tunable, coherent radiation source that is stable in physiological conditions. One way to achieve this goal is by using

a nanoscale nonlinear optical mixing component that coherently converts arbitrary input laser into desired frequency. This has been recently achieved with individual potassium niobate ($KNbO_3$) nanowires[109], which exhibit efficient second harmonic generation (SHG), and act as frequency converters, allowing the local synthesis of a wide range of colors via sum frequency generation (SFG, Figure 1.7C-D). This tunable nanometric light source has also been used to implement a novel form of subwavelength microscopy, in which an infrared laser is used to optically trap and scan a nanowire over a sample. The availability of such tunable nanoscopic light sources in liquid environment points towards a wide range of potential applications in physics, chemistry, materials science and biology. Lastly, while it has been demonstrated that it is possible to perform efficient second/third harmonic generation and sum frequency generation within single nanowires, it is unclear at this stage whether it is possible to have optical parametric generation/amplification within single nanowires.

As demand for computer processing speed increases, on-chip optical data transfer promises to greatly enhance current electronic computation schemes. For an optical technology to be feasible, light must be confined and routed in dimensions much smaller than its wavelength to allow for sufficient miniaturization of chips. Indeed, dielectric waveguides has been pushed into subwavelength regime by employing high refractive index and nonlinear wavelength upconversion materials. However, the refractive limit still poses an insurmountable barrier for further miniaturization of dielectric nano-photonic components, whereas plasmonic devices are only limited in their size by the dimensions of the input–output coupler and the transmitting medium.

Although all conductive materials, such as metals, support plasmons, the coinage metals (that is, copper, silver and gold) have been most closely associated with the field of plasmonics as their plasmon resonances lie closer to the visible region of the spectrum, allowing plasmon excitation by standard optical sources and methods. Plasmon propagation has been demonstrated for chemically prepared silver and gold nanorods or nanowires with transverse and longitudinal dimensions of less than 100 nm and from 4 to 50 μm, respectively. Optical excitation of SPP mode can be achieved by total internal reflection (TIR) illumination[6,19], tightly focusing laser beam at one end of the nanowires[5] or on a metallic nanoparticle attaching to the surface of the nanowire that act as a scattering center[21]. A quantum emitter in the near-field of a Ag nanowire can also excite propagating SPPs as the optical dipolar near-field contains large momentum components matching those of SPPs[110,111]. Most recently, optical coupling between dielectric waveguide and Ag nanowire was also proved feasible towards SPP modes excitation and is the by-far the most integration friendly method for coupling SPPs into metal nanowires[112].

Ag nanowire, in particular, is an ideal candidate for plasmonic waveguide. On one hand, silver has the smallest known inherent metal loss of all metals for optical frequencies from visible, near IR to telecommunication wavelength. On the other hand, chemically synthesized Ag nanowires are single crystalline in nature and has atomically smooth surface, which would significantly reduce the ohmic loss resulted from grain-boundary

and surface scattering compared to microfabricated Ag waveguides based on polycrystalline thin films. The reported propagation lengths of 100 nm Ag nanowire is typically around 10μm for red and near IR wavelengths[6,112,113], whereas the propagation length of a 1μm wide, 70nm high fabricated Ag microstripe on glass is less than 4μm[12] at 633nm (13μm in numerical simulation[13]), ~1/3 of a 100nm diameter single crystalline Ag nanowire.

Similar to light propagation in optical fibres, plasmon propagation is not limited to a straight line, but electromagnetic radiation contained in the plasmon can be bent and split using appropriate plasmonic structures[5,21,113]. For example, a metallic wire branching into more than one path enables a plasmon to continue propagating down both paths of the wire, similar to an optical beamsplitter. Rational integration of dielectric and Ag nanowire waveguide components into hybrid optical-plasmonic routing devices has also been demonstrated[113]. These capabilities are essential for incorporating low-loss Ag nanowire waveguides as practical components into high capacity photonic circuits and can be extended to other inorganic dielectric waveguide systems such as Si, SiO_2, GaN, and Si_3N_4.

1.6 **Nanowire Photodetectors and Photovoltaics**

Nanostructures that efficiently detect optical inputs and process them as electrical outputs are of great interest to improving nanoscale devices in opto-electronics. A linear nanowire photodetector/switch has been realized in ZnO[114], InP[115] and CdS[116] nanowires fabricated into a horizontal transistor configuration where an optical flux forces the wire from an insulating to a conducting state. The responsivities of typical InP nanowire photodetectors are as high as 3000 amperes/watt as a figure of merit. However, for better photosensitivity at the nanometer scale, large amplification is often required to detect light at low levels (i.e. single photons) with reasonable response times. Recently, avalanche multiplication of the photocurrent has been reported in nanoscale p–n diodes consisting of crossed silicon–cadmium sulphide nanowires[117]. The high sensitivity nanowire avalanche photodiodes (nanoAPDs) exhibited detection limits of less than 100 photons ($\lambda <$ 500 nm) and subwavelength spatial resolution of 250 nm. Currently, these nanoAPDs exhibit sensitivity that is comparable to that reported for conventional planar APD structures. Temporal response of these nanoAPDs was measured to be on the order of several micro-seconds, which is considerably slower than large-area commercial Si APDs[118]. Use of core-shell nanowires could further enhance gain, improve detection sensitivity and device stability. Additionally, these nanoAPDs may be fabricated into crossed nanowire arrays which can be addressed independently without cross-talk. NanoAPDs and arrays offer substantial promise in diverse areas ranging from nanopositioning, integrated photonics, and near-field detection to real-time observation of single protein dynamics with integrated nanoAPDs in microfluidics[119].

Yet, another crucial component to the operation of any nano-photonic devices is the power supply. Solar cells are promising devices for inexpensive, large-scale solar energy conversion. With miniaturization, they might also be directly incorporated into nano-photonic systems as integrated power sources to form a self-powered system. The

use of semiconductor nanowires for photovoltaic applications is in itself advantageous: 1) it allows long absorption paths while short distances for carrier collection/transport can be maintained, i.e. light absorption and charge transfer can be orthogonalized; 2) Interpenetrating heterojunction interface is possible at the nanoscale, allowing efficient carrier extraction following light absorption; 3) strong light trapping can be achieved in high density nanowire arrays; and 4) modification of materials properties and cell efficiencies is possible through size and composition variation of the nanostructures.

The anodes of dye-sensitized solar cells[120] are typically constructed using thick films of TiO_2 or ZnO nanoparticles that are deposited as a paste and sintered to produce electrical continuity. The nanoparticle film provides a large internal surface area (characterized by a roughness factor, defined as the total film area per unit substrate area, of ~1,000) for the anchoring of sufficient chromophore (usually a ruthenium-based dye) to yield high light absorption in the 400–800 nm region, where much of the solar flux is incident. During operation, photons intercepted by the dye monolayer create excitons that are rapidly split at the nanoparticle surface, with electrons injected into the nanoparticle film and holes leaving the opposite side of the device by means of redox species (traditionally the I^-/I_3^- couple) in a liquid or solid-state electrolyte. Dye-sensitized solar cells fabricated from dense arrays of oriented, crystalline ZnO nanowires have been designed to improve charge collection efficiency[121]. The nanowire anode is synthesized by mild aqueous chemistry and features a surface area up to one-fifth as large as a typical nanoparticle cell. The direct electrical pathways provided by the nanowires ensure the rapid collection of carriers generated throughout the device, and a full sun efficiency of 2.5%[122] has been demonstrated, limited primarily by the surface area of the nanowire array. More recently, coaxial silicon nanowires (p-type/intrinsic/ n-type (p-i-n)) has yielded an apparent energy conversion efficiency of up to 3.4% under one solar equivalent illumination and is able to drive functional nanoelectronic sensors and logic gates[123]. These nanowire-based photovoltaic elements might find general usage as environmental friendly self-integrated power supply for ultra low power nano-photonic and diverse nanosystems. However, a scientific challenge remains as to whether it is possible to design and synthesize nanowires and their heterostructures with improved performance beyond existing silicon photovoltaic technology.

1.7 **Nanowire - Living Cell Interfaces**

Another emerging area of great interest is the interfacing of semiconductor nanowires with living cells. After years of nanowire research, we now have a good understanding of their electrical and optical functionalities. They can be used as transistors[62] and sub-wavelength optical waveguides[104,113]. Their cross-sections are much smaller than the typical cell dimensions, which means minimal invasiveness, while their high surface area ensures proper cell-nanowire communication. All of these considerations make the nanowire a powerful platform to interface with living cells for various purposes[124-126]. This includes interfacing with stem cells for precise delivery of small molecules, DNA and proteins, and their potential use as a universal platform for guided stem cell differentiation. In another tour-de-force demonstration, the Lieber group has successfully integrated high density silicon nanowire transistor arrays for the detection, stimulation

and inhibition of neuronal signal propagation[127]. In addition, the multiplexed signal recording capability of entire nanowire transistor arrays has enabled temporal shifts and signal propagation to be determined with very good spatial and temporal resolution. This research direction of interfacing nanowires and living cells (Figure 1.8) is certainly one of the most exciting topics at the moment, and is quickly unfolding. While it is true that the nanowire in this case is serving as a versatile technological tool or platform, many new discoveries are expected when such platforms are used to tackle real biological problems.

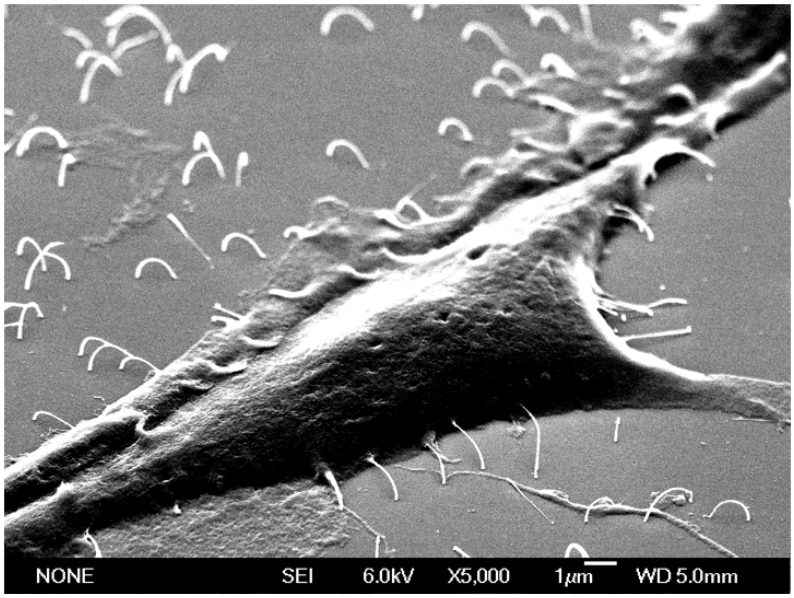

Figure 1.8 SEM images of individual cells sitting on silicon nanowires.

1.8 **Perspectives**

The ability to manipulate pulses of light within sub-micron volumes is vital for highly integrated light-based devices, such as optical computers, to be realized. Chemically synthesized nanowire represents an important class of photonic building blocks that exhibit sub-wavelength optical functionalities. While state-of-art lithography techniques are capable of fabricating nanostructured features with dimensions discussed in this article, chemically grown nanowires still possess unique advantages of being single crystalline, relatively defect free, having atomically smooth surface and being able to accommodate large lattice mismatches. Using a combination of nanolithographic tools, it is highly feasible to assemble photonic circuits (Figure 1.9) from a collection of nanowire elements that assume various functions, such as light generation, routing and detection. Since the range of nanowire material types now include active, passive, nonlinear and semiconducting inorganic crystals, as well as a rich variety of polymers, synthesizing from the bottom up offers novel design-by-choice schemes to facilitate the assembly of multi-functioning components on the same substrate. Because of their small footprint and

low power consumption, they can be self-powered, and readily embedded in cell phones or wrist-watches.

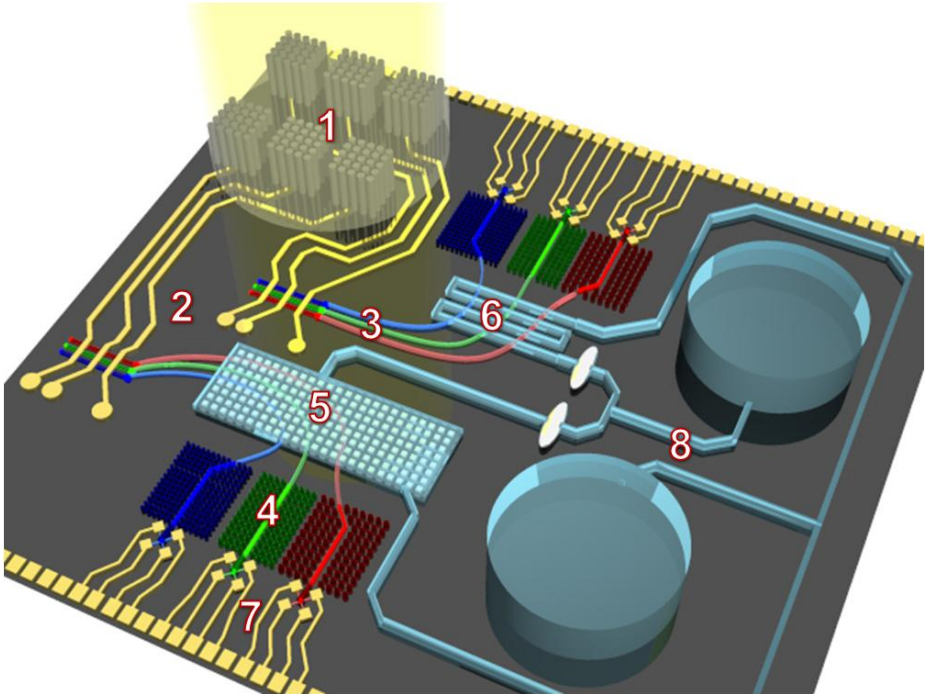

Figure 1.9 Future nano-photonic circuits for chemical analysis will require the integration of nanowire-based devices that assume different functions, such as nanowire solar cells as on-chip power supplies (1), laser diodes/LEDs as light sources(2), nanoribbons (3) and 2D photonic bandgap (PBG) nanowire arrays (4) as filters and waveguides to select and route input and output signals; (6), sample analysis chambers, such as silver nanocube arrays for SERS (5) or nanoribbon/sample intersection for absorption analysis; nanowire based photodectectors (7) and a microfluidic system for liquid sample transport (8).

On the other hand, while the fast development of nanoscience has provided numerous exciting opportunities for the electronics and photonics applications, it is also important to point out that certain nanoparticles are proving to be toxic, and nanowires are obviously reminiscent of asbestos and chrysolite. Therefore, a systematic evaluation of the environmental and health implications of the large-scale production of these materials is urgently needed[128].

The past decade has seen tremendous progress made in this exciting research field of semiconductor nanowires. However, many fundamental issues and questions still remain. While it has been demonstrated that nanowires can indeed have many different functionalities such as light emission, lasing, waveguiding, and non-linear optical mixing, it is important that quantitative comparisons be made with conventional thin film technology in terms of efficiency, fabrication cost and stability. Such benchmarking is important to gauge whether this new class of nanostructures is a viable candidate for the future generation of photonic technologies. Unfortunately, such benchmarking data is

critically lacking at this point. For example, one of the appealing features of nanowires is that they can be made into single crystalline, single domains, very well-facetted with low defects, all of which are critical for high optical quality. On the other hand, nanowires contain a significant amount of external surface area which potentially introduces a large density of surface trap states that are detrimental for light emitting processes. Naturally, such surface states need to be properly passivated, which is especially important in nanowire-based solid state lighting.

Another powerful approach towards subwavelength photonics is the use of the plasmonics that would arise at metal-dielectric interface. For example, a recent theoretical study of a semiconductor nanowire core--metal shell structure[129] showed that positive modal gain is achievable, pointing towards the feasibility of making a laser with all three dimensions less than one wavelength[130]. This line of research could further lead to the fabrication of single photon sources, and the development of hybrid plasmonic-photonic waveguides with strong mode confinement[131].

The development of a nanoscopic coherent light source could also lead to a new type of nanowire probe for *in-situ* single cell imaging, essentially a nanowire-based single cell endoscopy. Development of such nanowire probes would enable us to carry out intracellular imaging and probing with high spatial resolution (Figure 1.10), monitor in-vivo biological processes within single living cells and greatly improve our fundamental understanding of cell functions, intracellular physiological processes, and cellular signal pathways. Nanowires have several key features that make them promising for applications in cell endoscopy including minimal invasiveness, high flexibility, high refractive index, evanescent wave optical sensing, and nonlinear optical conversion capabilities. The nanowires used for these probes will generally have diameters below 100 nm and high aspect ratios, ensuring the non-invasiveness of the nanowire probes. The nanowires are also highly flexible and yet mechanically robust. The twisting and bending in these nanowires will not cause significant optical propagation losses[104], and will greatly facilitate the application of such probes in single cell imaging. Due to their high refractive index, nanowires also function as efficient sub-wavelength optical waveguides, even in high-index physiological liquids and/or living cell environments[108]. Waveguiding also enables highly localized excitation and detection, limiting the probe volume to the very tip of the nanowire (i.e. down to pico- and femtoliter). Additionally, the application of nonlinear optical nanowires into the probe platforms will introduce two important features[109]: subwavelength waveguiding and frequency conversion capabilities. This will enable the input of an IR beam at one end of the nanowire and the use of visible or UV output on the other end for the cell imaging/probing. The use of IR as an input beam would greatly benefit the entire imaging process in realistic physiological environments.

Such novel nanowire probes promise intracellular imaging with greatly enhanced three-dimensional spatial resolution as well as temporal resolution. In addition, these nanowire probes could be used for spot-delivery or extraction of chemicals (proteins/DNAs) from single living cells with much improved spatial resolution as

compared to conventional delivery/extraction methods. Considering such remarkable progress in nanowire photonics, many new discoveries should be expected down the road.

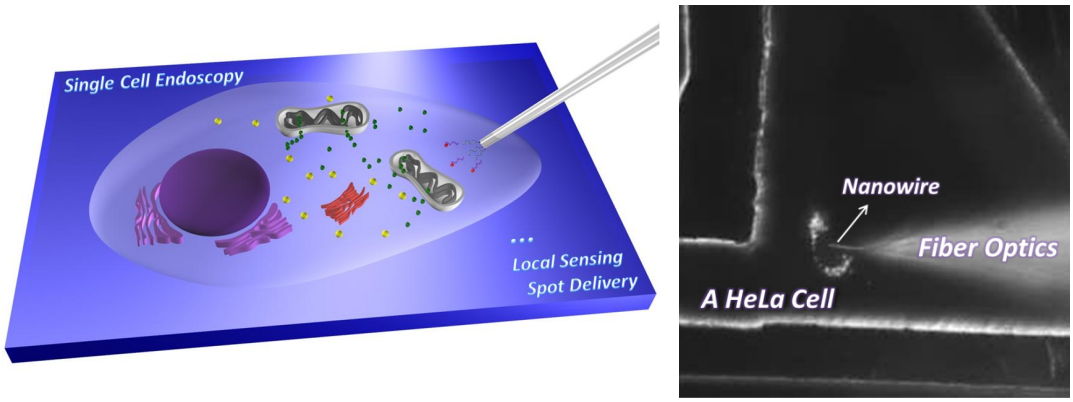

Figure 1.10 Nanowire-based Biological probe for endoscopy, spot delivery and sensing within a single living cell. The image on the right shows a single Human cancer cell (HeLa) was probed by an oxide nanowire probe attached onto an optical fiber tip.

All images are reproduced with the permission of Nature Publishing Group and the American Chemical Society

Chapter 2
Direct Photonic-Plasmonic Coupling and Routing in Single Nanowires

Recent research efforts have scaled down the plasmonic waveguides[5,6,20,132-134] from microscale metal stripes[135] to nanoparticles arrays[136,137] and nanowires[5,6,11,14,19,20], demonstrating the feasibility of sub-wavelength plasmonic optics. However, the inherent metal loss makes it impractical to transfer digital data across the entire photonic IC chip (~1mm) solely with plasmonic waveguides. It becomes increasingly important to be able to integrate plasmonic modules with low-loss, dielectric optical interconnects. In order to achieve such hybrid plasmonic-photonic circuit, it is critical to develop nanoscale plasmonic waveguides with reduced losses and small mode volume, and equally important, to ensure the compatibility with conventional optical circuitry.

In this context, chemically synthesized Ag nanowires have emerged as promising candidates for sub-wavelength plasmonic waveguides. The high crystallinity and atomically smooth surface of Ag nanowires should reduce the total propagation loss as compared to those microfabricated polycrystalline Ag waveguides. As a result, Ag nanowires are able to support surface plasmon propagation with two-dimensional subwavelength mode confinement. However, integrating the low-loss Ag nanowire waveguides into a plasmonic-photonic routing network requires a simple, efficient and versatile strategy to couple the light field in and out of the Ag nanowire so that the digital information can be launched and harvested.

The major challenge in optically exciting SPPs in Ag nanowires lies in the dispersion relation mismatch for SPPs and photons. To bridge the difference in the wave vector k_x along the propagation direction $\vec{x}$, at any given photon energy $\hbar\omega$, the photon momentum $\hbar k_x$ ($=\hbar\omega/c\sqrt{\varepsilon_0}$, ε_0 being the dielectric constant of the dielectric enviroment) has to increase by a $\hbar\Delta k_x$ in order to couple photons into SPPs. Various methods have been proposed to bridge this gap and launch propagating SPPs in Ag nanowires. The total internal reflection (TIR) illumination method utilizes a prism to match the momentum of SPPs and the incident photons[6,19]. Direct local excitation was demonstrated by focusing a laser on the end facets of the Ag nanowires[5] or on a metallic nanoparticle attaching to the surface of the Ag nanowire that act as a scattering center[21]. A quantum emitter in the near-field of a Ag nanowire can excite propagating SPPs as the optical dipolar near-field contains large momentum components matching those of SPPs[110,111]. However, these coupling schemes do not lead to easy interconnection with conventional optical components for photonic IC fabrication. The recently reported polymer-Ag coupling method is an important advance towards on-chip integration. However, it still has many

restrictions on the coupling conditions, including Ag nanowire orientation, position and incident light field polarization[112].

In this chapter, we discuss the optical coupling between a Ag nanowire plasmonic waveguide and a conventional dielectric nanowaveguide. Ag nanowire SPPs can be excited simply by contacting it with a SnO_2 nanoribbon that serves both as an unpolarized light source and a dielectric waveguide and with minimum restriction on the coupling conditions. SPPs can be launched into the Ag nanowire at arbitrary positions at any orientation.

This chapter will also discuss the measurement of the propagation-distance dependent waveguide spectra and frequency-dependent propagation length on a single Ag nanowire. The assembly of the metal-dielectric junction is completely reversible, making it possible to monitor the properties of a single Ag nanowire while varying the interconnection and propagation condition.

Finally, this chapter will describe the prototypical photonic-plasmonic routing devices which are essential for incorporating low-loss Ag nanowire waveguides as practical components into high capacity photonic circuits. This versatile coupling strategy represents a major step towards realizing photonic-plasmonic hybrid circuitry and has made possible the systematic far-field study on the SPP propagation in Ag nanowires.

2.1 **Plasmonic-Dielectric Coupling Device**

Single-crystalline SnO_2 nanoribbon have been established as efficient UV-NIR waveguides[86,104,108]. Their high aspect ratio, strength and flexibility enable their manipulation on surfaces, and can be assembled into optical networks and components. SnO_2 nanoribbons also exhibit photoluminescence with UV excitation and can act as a simultaneous nanoscale light source and waveguide. The Ag nanowires used in this work was synthesized by a modified polyol synthesis. The nanowires have 5 folding twinning planes along their axis, and they are bound by 5 atomically smooth single crystalline {100} surfaces.

Figure 2.1A illustrates schematically the device setup. A silver nanowire sits on top of a SnO_2 nanoribbon waveguide that bridges two oxidized Si substrates. A UV laser was focused on the lower right corner of a SnO_2 nanoribbon to excite the broad-band photoluminescence (PL) of SnO_2, which is then waveguided along the nanoribbon towards the Ag nanowire. At the metal-dielectric boundary, photons travelling in the SnO_2 waveguide are scattered with a broad distribution of wave vectors and offer the Δk_x needed to match the momentum of photons and SPPs. The SPPs are guided within the 100nm Ag nanowires and scatter back into free space photons at the distal ends of the wire.

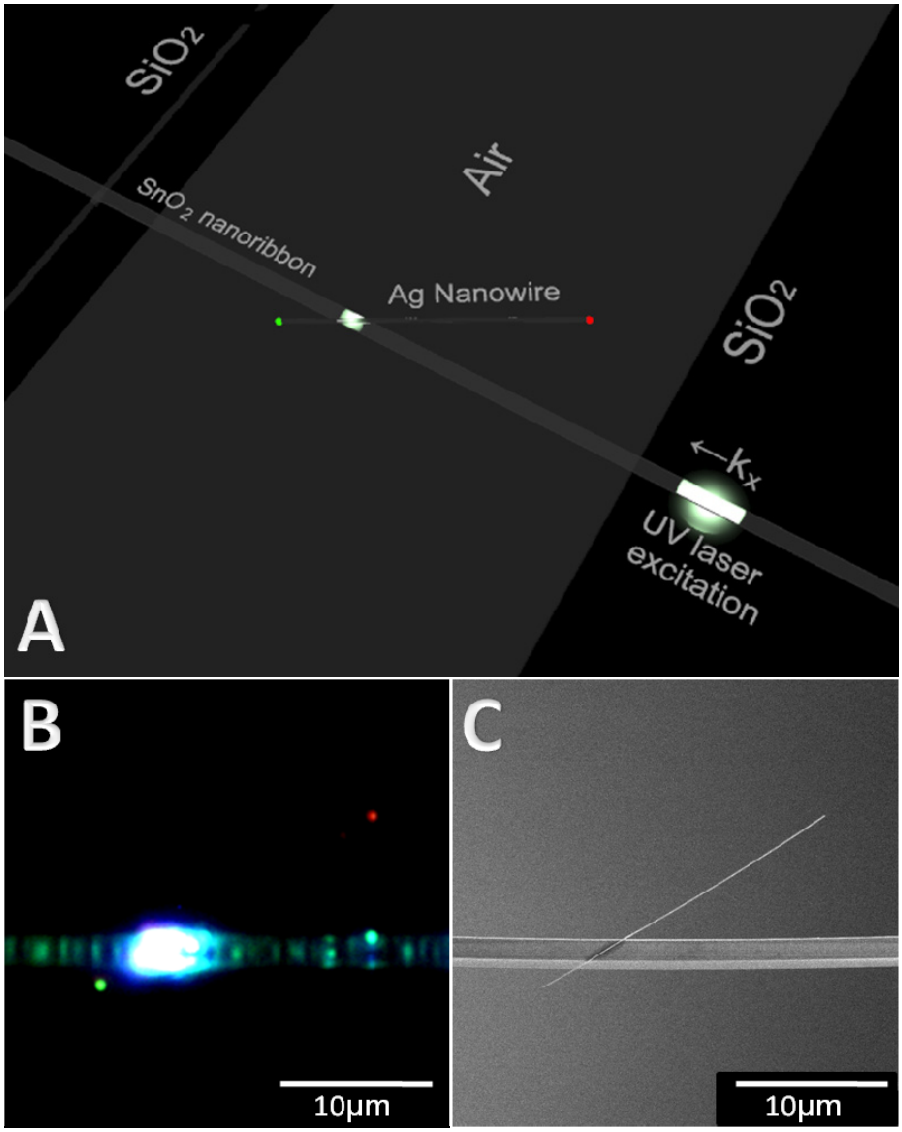

Figure 2.1 Excitation and propagation of plasmon modes in a Ag nanowire waveguide. A. 3D Schematic drawing of the photonic-plasmonic routing device showing a Ag nanowire/SnO_2 nanoribbon cross-junction structure suspended between two SiO_2/Si wafers. A UV laser beam was focused on the lower right part of the SnO_2 nanoribbon to excite broad band photoluminescence (PL). The PL is then waveguided along the nanoribbon to the metal-dielectric junction. Light scattered at junction was coupled into surface plasmon modes of the Ag nanowire, which then propagate along the wire and finally scattered back into free space photon at the two distal ends. **B**, Optical microscope image showing the waveguiding of the SnO_2 PL in the actual photonic-plasmonic routing device illustrated in a. The large bright spot is the metal-dielectric junction where the photons in the SnO_2 nanoribbon couple into SPPs of the Ag nanowire waveguide. The emission (green and red) from both tips of the Ag nanowire can be observed by eye. The SnO_2 nanoribbon was excited from the far right section (not shown). **C**, SEM image of the same device in B.

Figure 1b is a microscope PL image of the real device built according to the schematics in Figure 1a. A SnO_2 ribbon (*n=2.1*) rests horizontally in the image, bridging a trench between two Si substrates (not shown) with 500nm thermal oxide (*n=1.45*). The bright white PL of the nanoribbon was excited from the far right end of the ribbon with a 325 nm He:Cd laser and while the photons are waveguided along the ribbon, they scattered off the local defects and other scatter centers, outlining the profile of the ribbon in the PL image. The bright white scattering spot is the metal-dielectric junction and the end emissions from the 20μm long, 100nm diameter Ag nanowire appearing in the image as a green spot on the lower left and a red spot on the upper right side of the ribbon. Both the Ag nanowire and the SnO_2 ribbon were positioned with a triple-axis micromanipulator equipped with a tungsten probe under a dark-field microscope. The Scanning Electron Microscope (SEM) image of the device is shown in Figure 1c.

2.2 Materials and Methods

2.2.1 SnO_2 Nanoribbon Synthesis

SnO2 nanoribbon waveguides were synthesized using a chemical vapor transport method previously described[138]. SnO powder was heated in a quartz tube reactor at 1100 ºC under 350 Torr of flowing argon (50 sccm). Milligram quantities of ribbons were collected on an alumina boat near the center of the reactor and deposited onto clean substrates by dry transfer.

2.2.2 Ag Nanowire Synthesis

The Ag nanowires were synthesized by reducing $AgNO_3$ with Ethylene Glycol (EG) in the presence of Poly(vinyl pyrrolidone) (PVP) [70]. Three stock solutions for the Ag nanowire synthesis were prepared at room temperature by dissolving 50mg NaCl, 50mg $AgNO_3$ and 200mg PVP (50,000g/mol) in 20ml EG, respectively. 50μL $AgNO_3$ solution and 150μL NaCl solution was added to 5ml of PVP solution while stirring at room temperature in a 25ml flask. After 5 minutes, the flask was then transferred to an oil bath at 170-180˚C, heated for ~5 mins till the mixture turned from white to orange, and injected with additional 0.5-2 ml of $AgNO_3$. After heating for 10-15 more minutes, the product was collected and washed with EG and ethanol to remove excess PVP. The purified nanowires were stored in ethanol. The product was then drop-cast on a PDMS substrate for manipulation. The synthesis yield large quantity of nearly pure Ag nanowires with nearly monodispersed diameter (100 nm) and lengths up to 50 μm.

2.2.3 Optical Characterization

A HeCd laser (Melles Griot, Irvine, CA) provided unpolarized continuous wave (CW) UV excitation (325 nm) for the photoluminescence of SnO_2 waveguide. CW diode lasers (532 nm, 650nm and 980nm) supplied visible lights for the propagation length measurement. The lasers were either focused to a beam diameter of 50μm on the SnO_2 nanoribbons or coupled to an optical fiber.

Intensity maps and color images were recorded with two microscope-mounted cameras (iXon, Andor Technology, Belfast, Northern Ireland and CoolSnap cf, Photometrics, Tucson, AZ). The tip-emission spectra measurement was performed with an inverted microscope (Olympus, IX71). Signal was collected through a 60x microscope objective lens (NA=0.7) and captured by a 1,340x400 pixel, back-illuminated CCD (Princeton Instruments, Spec-10:400B) and spectrometer (Princeton Instruments, SpectraPro 2300i).

Manipulation and Probe fabrication for the propagation length measurement: For nanoribbon manipulation, we used a three-axis commercial micromanipulator equipped with tungsten probes (≈400 nm tip diameter). The probe utilized for exciting the ribbon waveguide was fabricated by attaching a SnO_2 nanoribbon to a chemically-etched[139] multi-mode UV-IR optical fiber with epoxy adhesive.

2.3 **Angular Dependence of Plasmonic-Dielectric Coupling Efficiency**

The coupling between the SnO_2 nanoribbon and the Ag nanowire was observed regardless of their relative positions and orientations, however, the coupling efficiency depends heavily on the coupling angle, which is defined as the angle between the propagation directions of SPPs in the metal nanowire and photons in the original dielectric waveguide. Figure 2.2A-D shows the waveguiding images of a Ag nanowire with different coupling angles (labeled on the images) to the SnO_2 nanoribbon. The two sets of images were from the same Ag nanowire and SnO_2 nanoribbon. The distance of propagation from the coupling point to the distal end of the Ag nanowire were also kept the same so that propagation loss are the same and the intensity of the Ag nanowire end emissions can be directly compared as a measure of the energy input into the Ag nanowire. With a smaller the coupling angle (22˚), more energy was coupled non-radiatively into the Ag nanowire, resulting in a brighter distal end emission; whereas with a large coupling angle (90˚), the majority of energy coming out from the SnO_2 ribbon at the junction was lost by scattering into free space.

Although the absolute coupling efficiency between the SnO_2 nanoribbon and the Ag nanowire is difficult to measure, the relative coupling efficiency (η_c), which is defined here as the ratio between the total light input into the Ag nanowire ($I_{in,Ag}$) and the total light output from the SnO_2 ($I_{out,SnO2}$) at the Ag-SnO_2 junction, can be estimated from the intensity of the Ag nanowire end emission and the radiative coupling loss resulting from the scattering at the wire-ribbon junction.

The amount of photons lost from the SnO_2 nanoribbon at the metal-dielectric junction either couples non-radiatively as SPPs into the Ag nanowire, or lost radiatively as free space photons through scattering. And the relative coupling efficiency η_c denotes the percentage of photons coupled into the Ag nanowire in the total output from SnO_2 nanoribbon due to the presence of the metal-dielectric junction. So η_c can be expressed as $\eta_c = I_{in,Ag}/(I_{in,Ag} + I_{scatter})$.

With the micromanipulator, we are able to change the orientation of a single Ag nanowire with respect to the SnO_2 nanoribbon. And η_c of a given coupling angle and input photon frequency can be estimated from the corresponding waveguiding images which gives the spacial intensity map of the free-space photons given out from the coupling system. The scattering loss $I_{scatter}$ can be measured directly from integrating the scattering spot at the junction. The integrated tip emission intensity $I_{out,Ag}$ relates to $I_{in,Ag}$ through $I_{out,Ag} = \eta_{out} \cdot I_{in,Ag} e^{-x/L}$, where η_{out} is the out coupling efficiency from the guided SPP modes to free space photons at the tip of the Ag nanowire, L is the propagation length and x *i*s the distance from the junction to the distal end of the Ag nanowire, which can be measured from the images. Plugging $I_{out,Ag} = \eta_{out} \cdot I_{in,Ag} e^{-x/L}$ into $\eta_c = I_{in,Ag}/(I_{in,Ag} + I_{scatter})$, the relative coupling efficiency can be expressed as $\eta_c = \frac{I_{out,Ag} \cdot e^{x/L}}{I_{out,Ag} \cdot e^{x/L} + \eta_{out} I_{scatter}}$. Here the η_{out} is a constant for a given Ag NW at the given wavelength, and we assume η_{out} to be 100% in our calculation to give a lower bound estimation of η_c. Using the average propagation lengths measured from a number of Ag nanowires for 980nm, 650nm and 532nm, we can back out the $I_{in,Ag}$ for each wavelengths and coupling angles, and subsequently calculate the relative coupling efficiency η_c.

Figure 2.2D shows the angular dependence of photonic-plasmonic coupling efficiency at 980nm. Here η_c is largely dependent on the coupling angle. Smaller coupling angle favors the coupling of the photons in the dielectric waveguide into SPPs in the Ag nanowire with a smaller scattering loss, resulting in a higher η_c. This is true for all 3 wavelengths (532nm, 650nm and 980nm) that we tested.

The angle dependence of coupling efficiency can be understood in terms of photonic-plasmonic mode matching. As we have discussed, at a given frequency ω, the momentum of the SPPs ($\hbar k_{SPP,x}$) in Ag nanowire is always larger than the momentum of the photon ($\hbar k_x$) in the dielectric waveguide along the SPP propagation direction $\vec{x}$. In order for the photons to couple into SPPs, a certain mechanism has to exist to provide the extra momentum $\hbar\Delta k_x = \hbar k_{SPP,x} - \hbar k_x$ to bridge this gap. In our coupling scheme, photons travelling in the SnO_2 waveguide are scattered at the metal-dielectric junction with a broad distribution of wave vectors that peaks at $k_x' = k_x$, or $\Delta k_x = 0$. That is to say, the smaller the momentum mismatch $\hbar\Delta k_x$ is, the more photons with required momentum $\hbar k_x' = \hbar(k_x + \Delta k_x) = \hbar k_{SPP,x}$ there would be, and consequently, the higher the coupling efficiency. That is exactly what happens at small coupling angles (θ) where the momentum of photonic modes in the dielectric waveguide $(\hbar k_x = \hbar\omega/c\sqrt{\varepsilon_0}\cos\theta)$ along the SPP propagation direction are large and better matched to the plasmonic modes. As the coupling angle increases, $\hbar k_x$ grows smaller, and it would be more difficult for the photons to obtain the large extra Δk_x needed to couple into SPPs.

The photonic-plasmonic coupling efficiency is also frequency dependent. The estimated η_c for 20˚ coupling angle is 56% for 980nm input photons, 43% for 650nm, and 15% for 532nm.

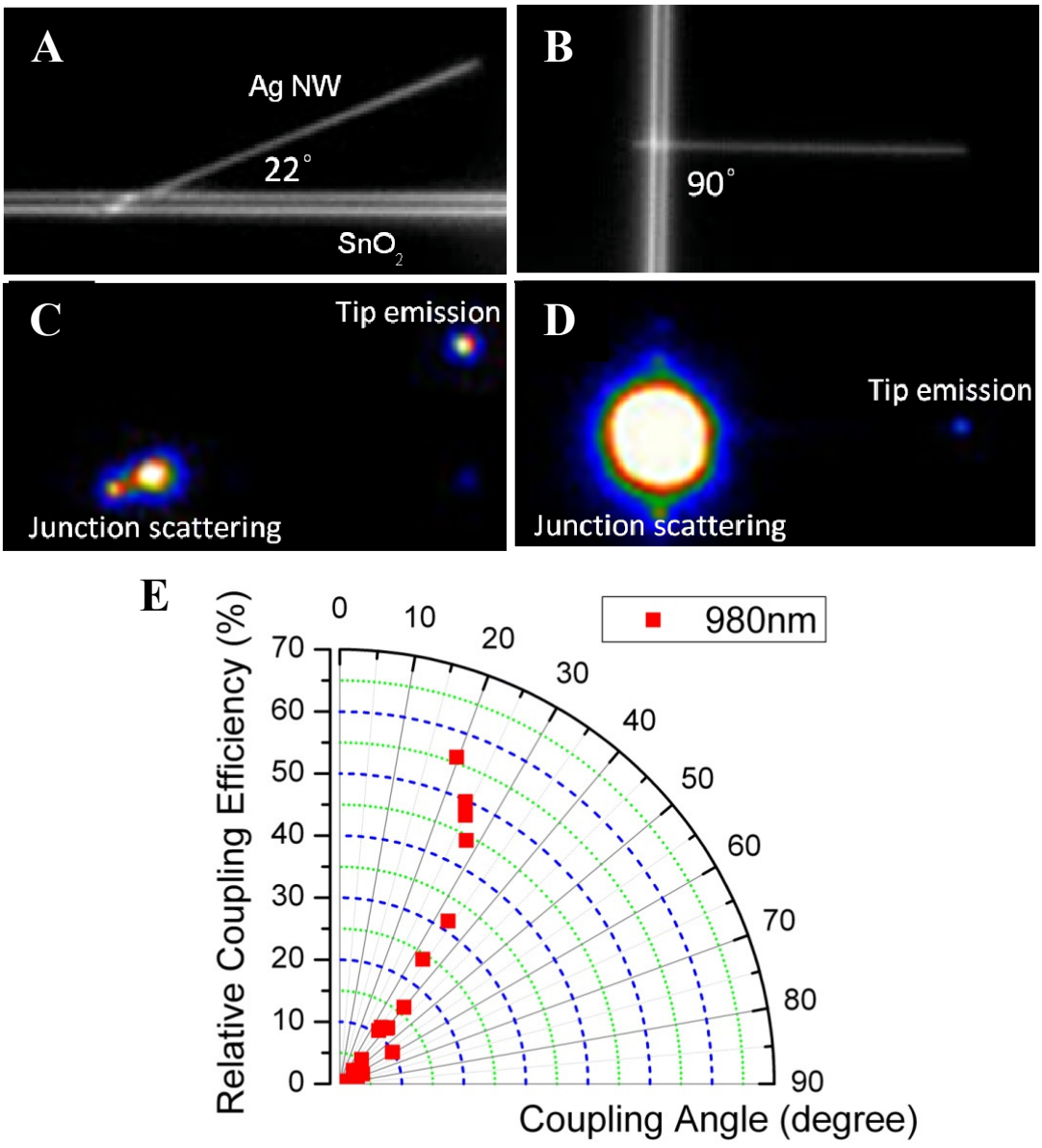

Figure 2.2 Angle dependence of Ag nanowire-SnO_2 nanoribbon coupling. A-B. Dark field images of a single Ag nanowire coupling to a SnO_2 nanoribbon at 22˚ and 90˚ angle, respectively. The distances of propagation were the same for the two geometries. **C.** Waveguiding image corresponding to the coupling setup in **a** with a 22˚ coupling angle. The bright spots on the lower left corner were the scattering at the Ag-SnO_2 junction, and spot on the upper right was the tip emission from the distal end of the Ag nanowire. **D.** Waveguiding image corresponding to the coupling setup in **B** with a 90˚ coupling angle. The big bright spot on the left was the scattering loss at the Ag-SnO_2 junction, and faint spot on right was the tip emission from the distal end of the Ag nanowire. All images in this figure were taken by a false-color camera that gives only the intensity profiles in the view. **E.** Angular dependence of Ag nanowire-SnO_2 nanoribbon coupling efficiency at 980nm.

Similar to the angle dependence, the frequency dependence of coupling efficiency is also related to momentum matching. The lower input photon frequency (ω) is, the closer the SPP dispersion curve to the light line, thus the smaller the required Δk_x is. As a result, higher coupling efficiency is always found with lower photon frequency.

2.4 **Plasmonic Waveguiding Spectra**

When squeezing the propagating SPPs into a highly confined geometry like a 100nm Ag nanowire, one central question is how the SPP propagation properties are modified compared to the bulk and other less confined geometries. One phenomenon that has been well-known for metal films[140] and metal micro-stripes[12] is a frequency dependent propagation loss. The attenuation of the electromagnetic field along the propagation direction arises from two sources: the *radiative* and *non-radiative loss*. The radiative loss is attributed to back-coupling of SPPs into photons, and is characteristic for asymmetric two-interface systems, as with TIR coupled devices[140]. Non-radiative loss, on the other hand, is due to absorption within the metal owing to the finite conductance of metal at optical frequencies. This is the dominant contribution to our system where the Ag nanowire is in a symmetric dielectric environment. The non-radiative loss depends on the dielectric function of the oscillation frequency of the SPPs. As the frequency of the incident photon decreases from visible to the near infra-red (NIR), the real part of the Ag dielectric constant ($\mathrm{Re}\{\varepsilon_{Ag}\}<0$) becomes more negative, while the imaginary part $\mathrm{Im}\{\varepsilon_{Ag}\}$ remains roughly constant. As the frequency of the incident photon decreases from visible to the near infra-red (NIR), the real part of the Ag dielectric constant ($\mathrm{Re}\{\varepsilon_{Ag}\}<0$) becomes more negative, while the imaginary part $\mathrm{Im}\{\varepsilon_{Ag}\}$ remains roughly constant. As a result, the electromagnetic field decays faster inside the metal, thus less metal absorption or Joule heating is expected.

For the Ag nanowires studied here, the frequency dependence of SPP propagation loss is clearly observed, as indicated by the color difference in the end emissions from the Ag nanowire in Figure 2.1B. As the distance of SPP propagation (d_p), defined here by the distance between the silver wire tips and the coupling point on the SnO_2 ribbon, increases, the high-frequency components damp faster than the low frequency ones, so the frequency distribution of the SPPs is expected to red-shift with increasing d_p. Here, the left silver end-facet is just 3μm from the SnO_2 ribbon, while the right end-facet is more than 10μm from the SPP launching point, thus more red-components are expected from the right emission end-facet, as observed in the experiment.

To further confirm the frequency-dependence of the propagation loss in Ag nanowires, we measured the tip emission spectra from a single Ag nanowire as a function of d_p and compared them to the SnO_2 ribbon emission which serves as the input signal. Using the triple-axis micromanipulator, we were able to pick the Ag nanowire up from the SnO_2 ribbon, move it along the original orientation of the Ag nanowire, and put it back on the SnO_2 ribbon, so that different segments of the Ag nanowire came in contact with the SnO_2 waveguide. The true-color image of the device (Figure 2.3A) and corresponding spectrum of the tip emission (Figure 2.3B) were recorded at each position. Great care was

taken to make sure that d_p was the only variable in the setup with the orientation of the Ag nanowire unchanged when the Ag nanowire was moved to a new position. Also, the particular position on the SnO_2 ribbon used for coupling was chosen to be free from large scattering centers that would increase background scattering signals.

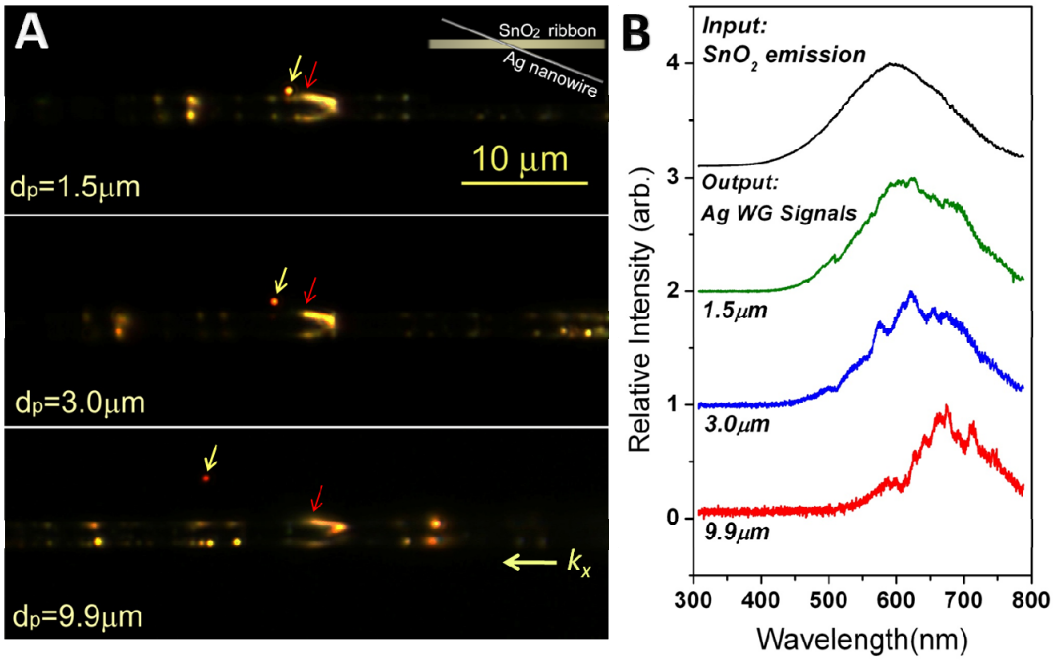

Figure 2.3 Dependence of Ag nanowire waveguide spectra on the propagation distance (d_p). A, True color optical microscope images showing Ag nanowire/SnO_2 nanoribbon junctions of different propagating distance fabricated by micromanipulation. The coupling angle of the Ag/SnO_2 junction was kept constant, so that the coupling efficiency would be the same for all three images. The yellow arrow in each image points to the distal end emission point of the Ag nanowires, whereas the red arrow points to the starting point of the SPPs propagation. The distance in between the yellow and red arrows in each image is the actual distance of propagation d_p. The color of the end emission from the Ag nanowire contained more red-components with increasing d_p. The schematic of the setup is shown in the inset at the upper right corner. **B,** Emission spectra of the Ag nanowire corresponding to the images in **A**, and the PL spectrum of the SnO_2 ribbon (input signal) used in the experiment.

The color images (collected with a 60x Olympus objective and a true color camera) in Figure 2.3A show a gradual change in the Ag nanowire tip emission colors from yellow, which is very close to the PL of the particular ribbon used here, to orange, and finally red when the distance of propagation, d_p, from the coupling point to the wire tip increased from 1.5μm to 3.0μm and 9.9μm. Figure 2.3B compares the spectra of both the SnO_2 ribbon PL emission, which is the input signal, to the tip emission spectra corresponding to the images in Figure 2.3A. The input PL spectra taken from the tip of the SnO_2 ribbon was a smooth Gaussian peak extend from 400nm to 800nm and with the maximum at

590nm. The tip emission spectrum for the lowest d_p =1.5μm resembles the input spectrum generally, but already starts to show a steep slope at the high frequency side of the peak, a red-shift of the left intensity-cutoff wavelength to 430nm, as well as a slight red-shift of the peak position, indicating an attenuation at the high frequency end. The red shift of the peak position was more prominent for the tip spectra for longer d_ps, with the emission maximum at ~620nm for d_p =3.0μm, and ~670m for d_p =9.9μm. The red-shift of the intensity-cutoff wavelength on the high-frequency side was also significant at these longer d_ps. For d_p =3.0μm, the intensity-cutoff was at ~440nm and was at ~510nm for d_p =9.9μm, a red-shift of more than 100nm compared to the input spectrum. All these signs clearly demonstrate a much smaller propagation loss as the frequency decreases.

2.5 Frequency Dependent Propagation Length

In a metal waveguide, the internal damping of SPP propagating away from the excitation along the propagation direction, $\vec{x}$, decreases exponentially as $I=I_0\, e^{-x/L}$. L, the propagation length, is defined by the characteristic length after which the intensity decreases to 1/e and is a measure of the propagation loss at a given frequency. L is determined by the imaginary part of the complex plasmon wave vector k_x, given by $L = \frac{1}{2Im\{k_x\}}$. To quantitatively measure the propagation length in our Ag nanowires, we designed an experimental setup illustrated in Figure 2.4A. Similar to the coupling device used before, a SnO_2 nanoribbon was used to excite the SPP propagation in the Ag

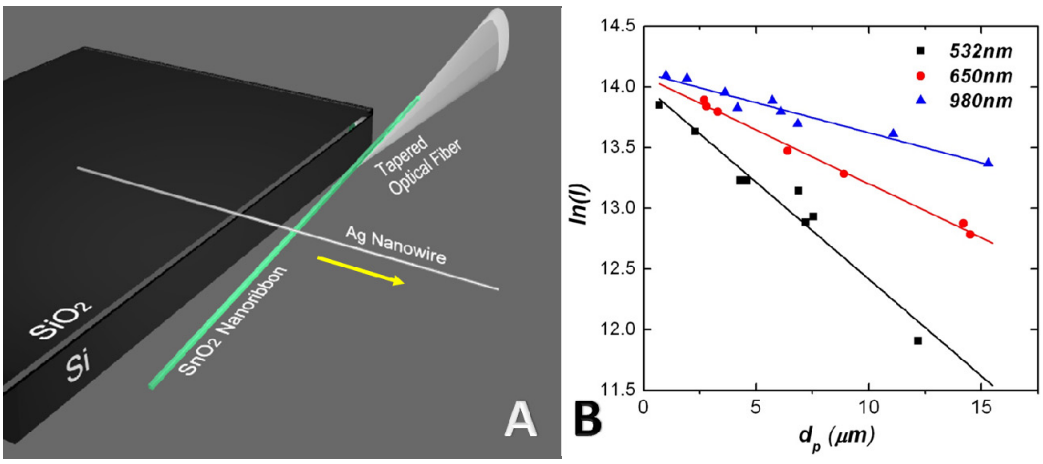

Figure 2.4 Frequency dependence of Ag nanowire SPP propagation length (*L*). **A,** Schematic of the experimental setup for measuring propagation length. A Ag nanowire is sitting on the edge of a thermal oxide substrate. Lasers of different frequencies were coupled into the Ag nanowire through a scanning SnO_2 nanoribbon probe attached to the end of an optical fiber. The yellow arrow indicates the sliding direction of the nanoribbon probe. **B,** Plot of *ln(Intensity)* as a function of propagation distance d_p at 2 visible wavelengths: **532nm** (green) and **650nm** (red); and an IR wavelength: **980nm**. The propagation lengths for the 3 wavelengths were 6.2μm, 11.3μm and 20.2μm, respectively.

nanowire, but here the input signal was no longer the broad-band PL of SnO_2. Fixed to the tapered tip of an optical fiber coupled to the visible and NIR lasers, a SnO_2 nanoribbon served as a dielectric waveguide to deliver laser photons to the Ag nanowire. This probe made of a SnO_2 nanoribbon and an optical fiber was then mounted on a micromanipulator with a ~15˚ angle to the focus plane of a dark-field microscope and is capable of scanning in three directions with 0.1μm resolution. Figure 2.5A shows a dark field image of the probe when the tip of the SnO_2 nanoribbon was brought into focus. This probe was then brought into contact with a Ag nanowire sitting on the edge of an oxidized Si substrate.

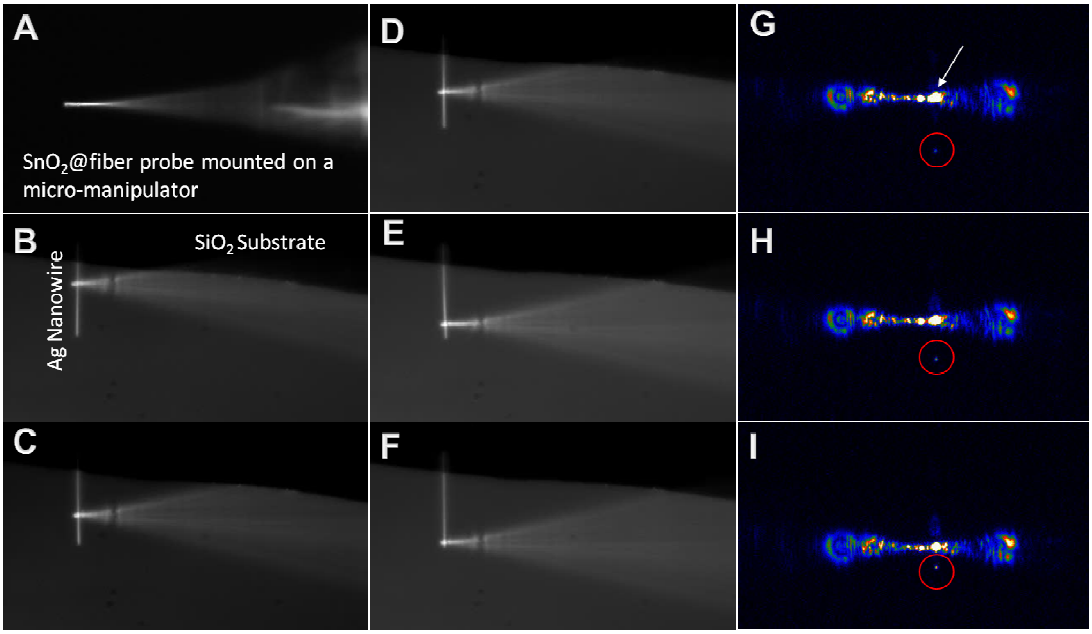

Figure 2.5 Optical image of the propagation loss measurement setup. A, Dark field image of the SnO_2 nanoribbon probe mounted on an x-y-z stage. The probe was ~30˚ to the focal plane of the camera. **B-F,** dark field images taken when the probe was gliding along a perpendicular silver nanowire that protrude from the edge of a SiO_2 substrate. The probe glided along the nanowire without deforming the nanowire or disturbing the coupling angle. **G-I,** Optical intensity map of the setup when the laser was coupled to the Ag nanowire through the SnO_2–Ag junction. The silver nanowire end emission intensity increased as distance of propagation decreased.

Figure 2.4A and 2.5 illustrate how this setup was used for the propagation length measurement. As the SnO_2 - Ag junction was moved towards the tip of the Ag nanowire, the distance for which the SPP modes had to travel before scattering back into photons at the end-facet of the Ag nanowire (d_p) decreased, and the tip emission intensity (I) increased accordingly. If we assume 1) the tip emission intensity was proportional to the intensity of the propagating SPPs modes, and 2) the dielectric-metal coupling efficiency remains constant as the SnO_2 nanoribbon was sliding on the Ag nanowire, the only variable in the process was d_p. We can estimate in this way the propagation length (L)

from the slope of the ln(I)- d_p plot. Here it should be noted that our assumption of the constant coupling efficiency is based on the fact that the probe can glide along the perpendicular Ag nanowire without bending the wire, moving the coupling point on the probe or disturbing the coupling angle, as shown in Figure 2.5B-F.

Figure 2.4B gives the typical ln(I)- d_p plots for 3 wavelength: 532nm, 650nm and 980nm. The propagation length calculated from the slop of the plots shows strong frequency dependence, increasing from 6.2μm for 532nm, to 11.3μm for 650nm and finally to 20.2μm for 980nm IR excitation. And the standard deviations from different wires were less than 0.4μm. Previous attempts to measure the propagation lengths in Ag nanowires through different approaches have set L_{628nm}= 9.1μm[112], L_{785nm}= 10.1±0.4μm[6], and L_{830nm}=3±1μm[5], respectively. While these results give reasonable estimations of the propagation lengths in their own systems and are in the same ballpark, they do not show a consistent trend and are hard to compare because of the different dielectric environments and measuring strategies in each case. Our measurement is the first systematic demonstration of the frequency dependence of propagation lengths in Ag nanowires, which agrees well with the trend we observed in the case of broad-band excitation, as well as the result from fabricated Ag microstrips[12]. The trend of increasing propagation length with wavelength extends to the telecommunication wavelength, according to the dispersion relation of the surface plasmon modes for a 100nm metal cylinder in vacuum[141].

One important advantage of chemically synthesized Ag nanowires compared to fabricated nanowires, is the remarkably lower ohmic loss. The propagation length of a 1μm wide, 70nm high fabricated Ag microstripe on glass is less than 4μm[12] at 633nm (13μm in numerical simulation[13]), ~1/3 of a 100nm diameter single crystalline Ag nanowire clad by air (11.3μm), or sitting on a substrate (9.1μm). Even for extended polycrystalline Ag films without lateral confinement, the propagation length of SPPs is 22μm at 515nm[140] and 60μm at 633nm[12], only 4-5 times larger than in our 100nm Ag nanowires. This observation echoes in the theoretical simulation results for Ag nano-waveguides. Although direct simulation with completely air-clad Ag nanowire (as in our experiment) is still absent, numerical simulation based on Drude-Lorentz dispersion model set the propagation length for a 120nm Ag nanowire sitting on a glass substrate at only 3.16μm[142] at 785nm when the Ag nanowire is considered a low-crystallinity medium. However, when dealing with a single crystalline Ag nanowire, the increased electron mean free path due to absence of the crystalline domain walls has to be considered[143], and the modified model matches very well with the experimental data of synthesized Ag nanowire[6] (10.1±0.4μm). The low ohmic loss in these chemically synthesized nanowires arises from (1) the single crystalline nature (2) chemical homogeneity or low impurity level, and (3) atomically smooth surfaces, all of which effectively reduce electron scattering during the collective oscillations in the metal.

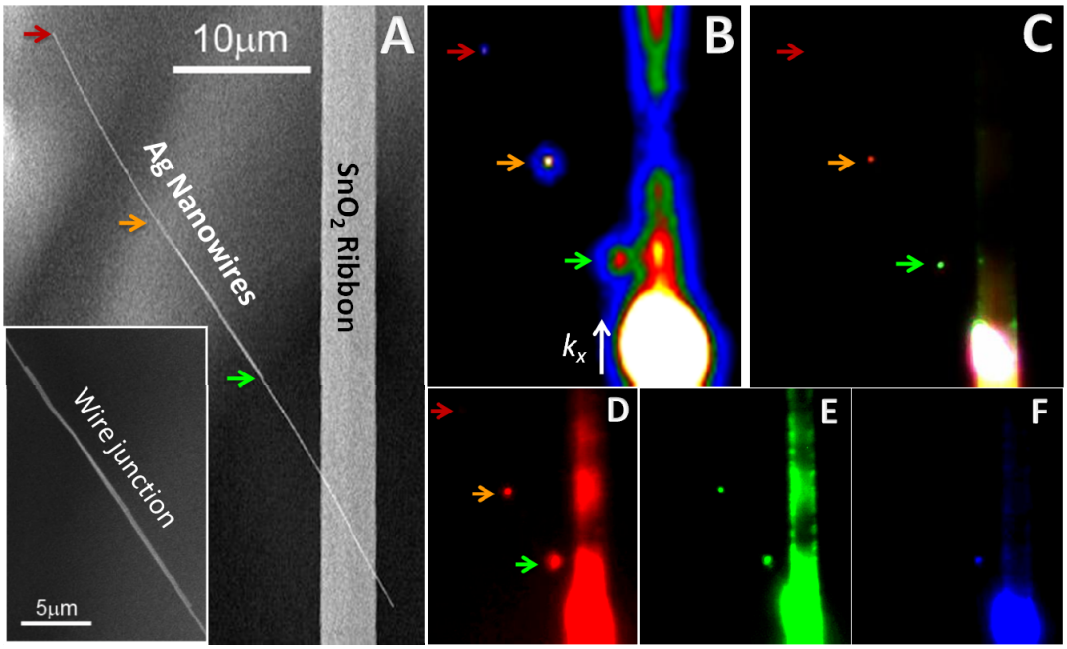

Figure 2.6 Dielectric-metal-metal (D-M-M) optical routing. A, SEM image of the D-M-M routing structure, showing a pair of overlapping silver nanowires couple to a SnO_2 ribbon. The overlapping length of the two Ag nanowires was 12μm. The inset shows the overlapping section of the two metal nanowires. The end of Ag nanowire-1 was marked by the orange arrow. The tips of Ag nanowire-2, which was not in direct contact with the ribbon were marked with the green and red arrows. **B,** Intensity map of the routing device when the PL of the SnO2 ribbon was excited from far below (out of scope) and coupled into nanowire-1 that's in direct contact with the ribbon and then propagate to nanowire-2, showing 3 distinct emission points at the 3 distal ends of the nanowires. **C,** The true color image of the same view as in **B**, the emission from the far end of nanowire-2 shown in the white dotted box was brought out by adjusting brightness of the area. **D-F,** the single R(red), G(green) and B(blue) color channels from **c**, showing a systematic decrease in propagation loss from blue to red optical frequencies. The colors are from the Bayer filter in the CCD image sensor (Sony ICX 205AK) of the Coolsnap cf camera.

2.6 **Plasmonic-Dielectric Routing**

The propagation length sets the upper size limit for any plasmonic feature on a photonic circuit. Another characteristic length, the decay length of electric field in surrounding dielectric environment, δ_d, which is typically on the order of half of the wavelength of light involved, dictates the maximum distance between any plasmonic or dielectric features that can have overlapping modes and couple to one another. Inter-wire coupling has been previous observed in a random assembly of Ag nanowires[5]. However, a rational integration of dielectric and Ag nanowire waveguide components into optical-plasmonic

routing devices, which is essential to incorporating Ag nanowire waveguides as practical components into highly integrated photonic circuits, is yet to be demonstrated.

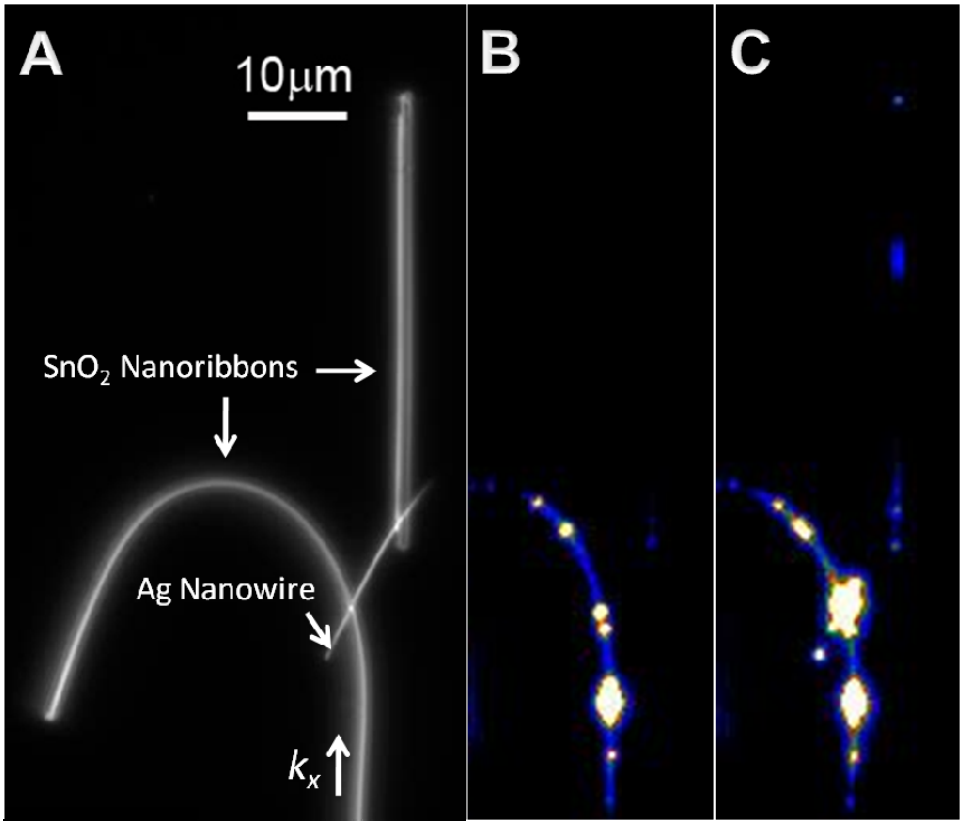

Figure 2.7 Dielectric-metal-Dielectric (D-M-D) optical routing circuit. A, Dark field optical image of the D-M-D coupling device, showing two SnO_2 nanoribbon bridged by a silver nanowire. **B,** Optical image of the intensity map of the device in the absence of the bridging Ag nanowire when the PL of the bent SnO_2 nanoribbon was excited from the bottom end (excitation spot not shown). No signal from the vertical ribbon was observed. **C,** Optical image of the intensity map of the device with the bridging Ag nanowire, showing a significant increase in the optical field in the vertical ribbon.

Here, both dielectric-metal-metal (DMM) and dielectric-metal-dielectric (DMD) coupling devices were designed and assembled to demonstrate the feasibility of optical-plasmonic routing. The device structure was illustrated in the SEM image in Figure 2.6A, showing a silver nanowire sitting on top of a SnO_2 ribbon, with a second silver nanowire attached to it with a 12μm overlap. The colored arrows points to the tips of the nanowires and the magnified image of the Ag nanowire junction is given in the inset. The surfactants on the Ag nanowires have been removed so that the two Ag nanowires were in direct contact. Figure 2.6B and C show the intensity map and true-color image of the routing of SnO_2 ribbon PL. SPPs are launched into the first Ag nanowire at the metal (Ag)-dielectric

(SnO_2) junction, and coupled into the second one evanescently without scattering loss along the metal-metal junction. They were scattered back into photons at the 3 discontinuities (wire tips) along the propagation direction, as marked by the color arrows whose positions are in accordance with Figure 2.6A. Despite the radiative losses at the wire tips, the SPP modes are able to propagate without complete attenuation to the farthest tip of the second wire that was 40μm away from the excitation (Ag-SnO_2 junction). This efficient plasmonic coupling between Ag nanowires in this routing device was a comprehensive result of the overlapping k_x, the long Ag-Ag junction, and the large SPP mode overlapping due to the minimum distance between the wires.

It should be noted that the dependence of the tip emission color on d_p in the single nanowire case is also observed in the coupling device. Figure 2.6D-F displays the red, green and blue color panel of the true color image in Figure 2.6C. The closer the tips were to the excitation, their emissions composed more high-frequency components. The blue components only exist at the first Ag nanowire tip that's 8μm from the excitation, while green ones survived 20μm of propagation, and the red ones were the only visible frequencies that were observable at farthest emission point, 40μm from excitation.

The design of the dielectric-metal-dielectric (DMD) coupling device is shown in the dark-field microscope image (Figure 2.7A). The two SnO_2 nanoribbons lying on an oxidized Si substrate were bridged with an Ag nanowire. The PL of the bent ribbon was excited from hundreds of micrometers away from the Ag-SnO_2 junctions to avoid direct excitation of the straight ribbon. In the absence of the Ag nanowire (Figure 2.7B), the propagating modes of the straight ribbon was not excited, with only a week scattering signal at the tip close to the bent ribbon. However, with the Ag nanowire bridging the two ribbons, the SPPs launched into the Ag nanowire couple back to guided optical modes in the straight ribbon, which then propagate 43μm to the distal end and scatter into free-space photons.

2.7 **Conclusions**

In conclusion, we have demonstrated the coupling between photonic and plasmonic waveguides at the single nanowire level. The frequency dependent propagation loss was observed in Ag nanowire and was confirmed by quantitative measurement and in agreement with theoretical expectations. Rational integration of dielectric and Ag nanowire waveguide components into hybrid optical-plasmonic routing devices has been demonstrated. This capability is essential for incorporating low-loss Ag nanowire waveguides as practical components into high capacity photonic circuits and can be extended to other inorganic dielectric waveguide systems such as Si, SiO_2, GaN, and Si_3N_4.

All images are reproduced with the permission of the National Academy of Sciences.

Chapter 3
Fabrication of Nanowire-based Optical Probes

The design of nanowire-based single cell endoscopy requires an instrumental platform, e.g. the nanowire-based optical nanoprobe, which is able to both physically direct the nanowire to designated sites inside a single living cell with precision control, and optically deliver and extract light to/from subcellular compartments. This process should have not only high spatial resolution, but also high temporal resolution. Additionally, the instrumentation of the nanoprobe design should be as simple, cost efficient and adaptable to average bio-lab environment as possible. Fabrication of such nanoprobe is the key to realize the anticipated functions of nanowire single cell endoscopy.

In the past several years, we have put tremendous efforts in design and fabrication of the nanoprobe system based on single nanowire waveguides and an optical fiber with tapered tip. The optical coupling of the optical fiber to both semiconductor and metal nanowire nanoprobes has been explored giving rise to two distinct versions of nanoprobes. Their fabrication processes, parameter optimizations, and mechanical/optical properties will be described in details in this chapter.

3.1 **Making Tapered Optical Fiber Tip**

There are two different methods that are commonly used to make sharp fiber tips: mechanical pulling and chemical etching (Figure 3.1). The instrumentation, mechanism of these two methods will be briefly reviewed. The pros and cons of each method for nanoprobe fabrication will be discussed in details.

3.1.1 Mechanical Pulling

The mechanical method for producing a tapered fiber tip relies on carefully controlled heating and pulling of an optical fiber until the point of rupture. Reliable and reproducible pulling is usually accomplished with a commercial micropipette puller (Figure 3.1A, left panel). Micropipette pullers are commonly used for creating tapered glass pipettes tips for biological applications, such as patch clamp experiments, and nucleus transferals. As illustrated in Figure 3.1A, right panel, an infra-red CO_2 laser (1.5μm) is focused on the optical fiber to locally heating the glass to a temperature of approximately 1600°C, slightly below the melting point of fused silica. Then, a reproducible tensile force is applying to the fiber. The fiber breaks at the point of heating, creating two tapered fiber tips with very fine points at the rupture location. The heating and pulling processes can be optimized by adjusting parameters such as heating time and pulling forces to obtain the desired taper and tip diameter of the optical fiber.

A major advantage of the mechanical pulling technique is the high reproducibility. Under a certain recipe, the angle and shape of the taper, as well as the tip diameter can be very consistent from trial to trial. In addition, the time required for producing two tapered fiber tips is only 1-2 minutes, which is a much faster process compared to chemical etching. Another important advantage of this technique is that the heated mechanical pulling creates very smooth surfaces on the tapered fiber, which has a significantly effect on increasing the effective contact area between the fiber and the nanowire. The increase in contact area in turn results in a stronger van der Waals interaction between the pair, making the probe more robust mechanically, and a stronger optically coupling of the waveguiding modes in the nanowire and in the fiber.

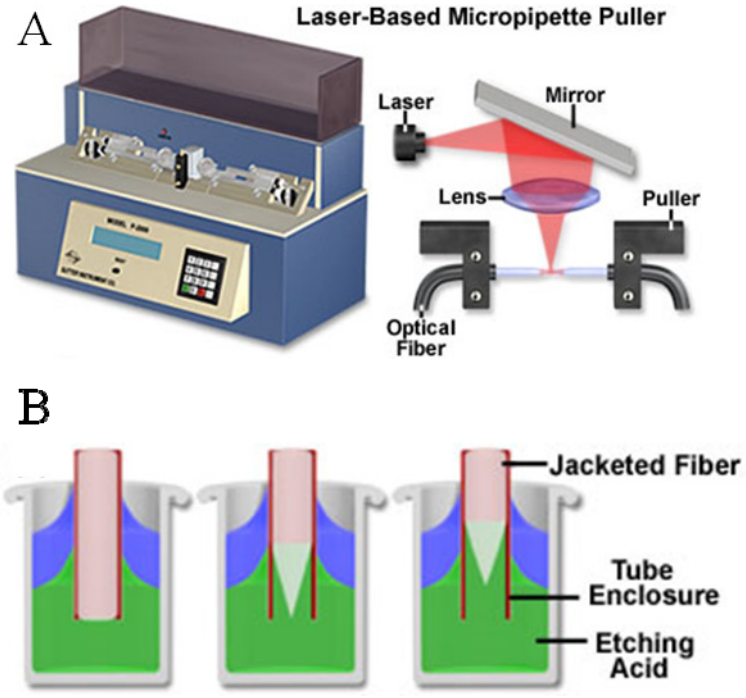

Figure 3.1 Tapering of optical fiber tip. A, Instrumentation and schematics of laser assisted mechanical pulling procedure for tapered optical fiber tip. **B,** Schematics illustrating the chemical etching procedure for tapered optical fiber tip.

A disadvantage of the technique is that the taper is usually much longer than on tips produced by chemical etching. Probes with a longer, more gradual taper typically have lower transmission efficiencies than those with shorter tapered regions, for a given tip aperture diameter. And a long thin taper is also more susceptible the probe to easy breakage during handling, probe fabrication and measurement. The most important disadvantage of this technique is that the pulling results in thinning of the optical fiber core as well as the cladding, which would distort the optical modes in the tapered region. This will be discussed in details in Section 3.3.

3.1.2 Chemical Etching

An alternative method of taper formation uses a powerful etchant, usually hydrofluoric acid (HF). The etchant is typically covered by a protective layer of a hydrophobic chemical (oil phase), which form a meniscus along the fiber tip during etching. Etching occurs at the point where the meniscus is formed along the fiber as it is dipped into the layered fluids. The existence of the oil phase also serves to prevent corrosion of the optic fiber above the tip region by the etchant vapor. This technique allows greater control of the cone angle produced on the optical fiber. The cone angle of the tapered fiber tip is controlled by the shape and contact angle of the meniscus, which is determined by the properties of the oil phase. This chemical etching method produces a much shorter taper compared to the pulling method. The large cone-angle tips provide at least an order of magnitude higher optical efficiency. However, the tip shape and its surface quality made from chemical etching are extremely sensitive to the etching environment. Air movement, temperature fluctuations, vibrations, and etchant concentration can have a strong influence on the shape and symmetry of the meniscus-etched probe, and on its surface roughness, resulting in a poor reproducibility.

To overcome the environmental sensitivity to some extent, a variation of chemical etching was developed. This method is termed "tube etching" which takes advantage of the different etching rates exhibited between the core material and the cladding surrounding an optical fiber. Instead of removing the polymer jacket from the fiber prior to etching, the cladded fiber end is immersed in the etchant (Figure 3.1B). Because the fiber jacket is resistant to degradation by HF solution, the entire etching process takes place inside the hollow tube formed by the jacket, as the fiber itself is reduced to a tapered geometry. One advantage attributed to tube etching over conventional chemical etching is the smoother glass surface and the reproducibility of the taper shape, probably due to the protective environment of the tube enclosure. One significant disadvantage of the chemical etching technique is the very hazardous chemicals (such as hydrofluoric acid) that are required for the etching process.

In our experiment, tapered optical fiber tips were fabricated by etching the fiber tips in the stack solution of hydrofluoric acid (HF, 49%) and 2,2,4-trimethylpentane (Sigma) for approximately 70 mins as previously described[144]. The cone angle of the tapered tip is controlled by finely adjust the duration of etching, which varies for fibers of different working frequency, which is due to the different doping level of these fibers. Shorter etching time generally result in more slowly tapered tip, or a smaller cone angle. On the contrary, longer etching time would result in sharper tapers. However, after the etching goes beyond a critical etching time, no further tip deterioration would occur and the tip would maintain its shape and cone angle which are determined by the properties of the polymer cladding and the oil phase. After the etching, fiber tips were rinsed with water and ethanol repeatedly, and then soaked in chloroform to remove the polymer buffer from the etched section to expose the fiber tip for further nanoprobe fabrication. We found that prolonged rinsing and soaking of the etched fiber in water is the most effective way to prevent surface roughness resulted from etch pits generated from small HF droplet

beaded up on the etched glass surface while drying. Soaking in water prior to drying would help dilute the HF solution that remains in the polymer tubing and reduce the concentration and size of the etch pits. Figure 3.2A shows the SEM images of an etched single mode optical fiber with a tip diameter of ~ 300 nm and a taper angle of 5°C, which is the optimized geometry for probe fabrication (See Section 3.3 for details). The glass surface of the fiber tip is very smooth for an etched fiber.

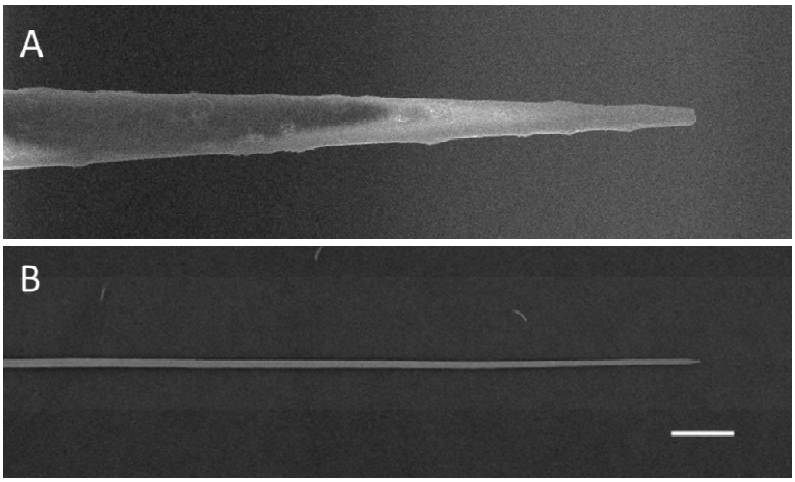

Figure 3.2 SEM images of the etched optical fiber and SnO_2 nanowires. A, SEM image of the fine tip of a single mode optical fiber chemically etched to a slowly tapered shape. The fiber tip has a tapering angle of 5º and end diameter of 300nm. **B,** SEM image of a typical SnO_2 nanowire used for nanoprobe fabrication, with an average diameter of 100nm. The nanowire is much smaller in dimension than etched optical fiber, thus less invasive to cell membranes. Scale bar: 1 μm.

3.2 **Semiconductor Nanoprobe Fabrication**

The nanowire probe was fabricated by bonding a SnO_2 nanowire (100-250 nm) (Figure 3.2B) to the tapered tip of a chemically etched single mode optical fiber with a cone angel of 3-5º (Figure 3.2A) and tip diameter of 300-500. The steps for fabricating the nanowire probe are illustrated in Figure 3.3A-C. First, a SnO_2 nanowire is picked up by the Tungsten (W) needle on a micromanipulator, which can move with 0.1μm steps in x-y-z directions. The SnO_2 nanowire is attaching to the W needle through van der Waals interactions. The nanowire is then aligned with the optical fiber and brought into contact to the tapered tip. The overlapping area and the van de Waals interactions between the nanowire with the optical fiber becomes much larger than that between the nanowire and the W needle, so that the nanowire is firmly attached to the glass surface and is easily detached from the metal needle. Apparently, the interaction between the glass and the nanowire depends on the effective contact area between the nanowire and the fiber, which is affected by the curvature and surface smoothness of the fiber, as well as the size, flexibility and surface quality of the nanowire. SnO_2 nanowires usually have a rectangular

or square cross sections, which guarantee a larger contact area than nanowires with round or hexagonal cross sections, like GaN, of similar dimensions. Nanowires with rectangular cross sections are also more flexible due to the thinning on one side. These belt or ribbon shaped nanowires almost always sit on the fiber with the fat side contacting the glass surface, conforming better to the curved surface of the tapered fiber.

The other end of the optical fiber was coupled to a laser so that the optical coupling between the nanowire and the tapered fiber tip can be monitored during the fabrication process. The relative position of the nanowire and fiber tip was then adjusted to minimize the scattering loss at the ribbon-fiber junction. The coupling is found to be most efficient when the nanowire is perfectly aligned with the optical axis of the fiber and when the very tip of the fiber, where the most light output is concentrated, overlaps with the nanowire.

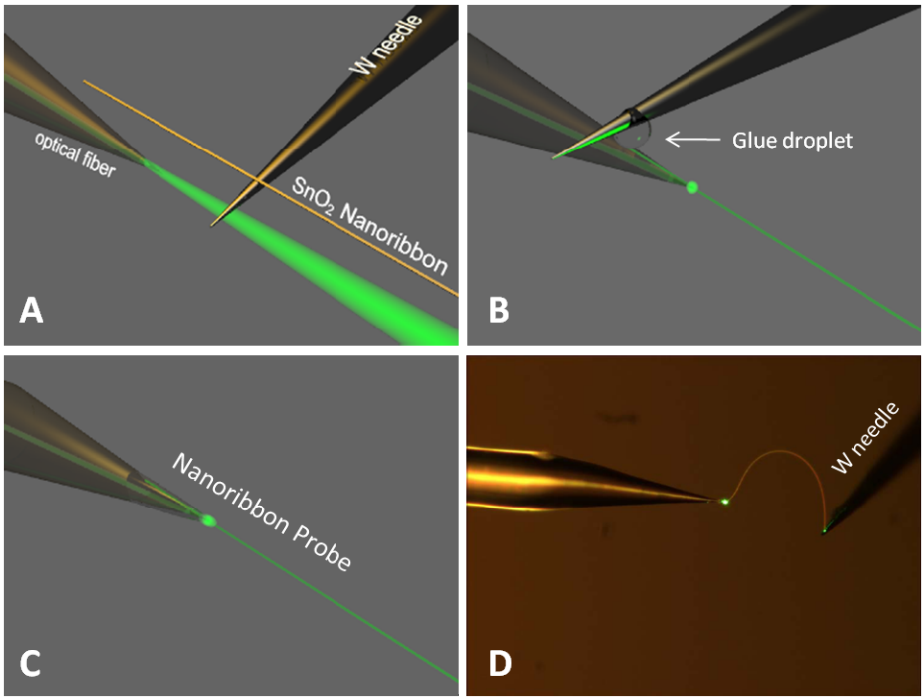

Figure 3.3 Procedure of nanoprobe fabrication. A, A SnO_2 nanowire is placed on the tapered tip of a single mode optical fiber with a tungsten needle mounted on a 3-axis micromanipulator. The blue laser coupled into the distal end of the fiber escapes at the tapered tip where the core of the optical fiber is exposed. **B,** A droplet of glue (Epoxy or Polydimethylsiloxane) was applied to the overlapping section between the nanowire and fiber. The blue laser is further coupled into the nanowire and re-emit at the tip of the nanowire instead. **C,** After the glue dried, the fiber and the nanowire were permanently bond together and the coupling was fixed.

Then a droplet of premixed epoxy glue (ITW Devcon) or Polydimethylsiloxane (PDMS, Sylgard® 184 Silicone Elastomer, Dow-Corning) was applied to the overlapping nanowire-fiber junction with the micromanipulator needle to bond them permanently. The epoxy glue is more viscous and applies thicker on the junction. It dries completely in ~30 mins at room temperature, and there is no post annealing required. However, the dried epoxy glue can be relatively brittle and there was found to be a higher chance of casualty during subsequent solution process with epoxy glued probes. The PDMS glue, on the other hand, is thinner in consistency and applies sheerer and more conformal. However, it requires post application annealing at 70°C for at least 2-3 hours. The transfer of the nanoprobe from the microscope to the furnace while the glue is still wet can be risky. So the fabrication success rate with the PDMS glue is generally lower. However, once the glue is dried, the PDMS bounded probes are more mechanically robust and flexible, so the lifetime of these probes are generally much longer. Another advantage of PDMS glue over epoxy is that PDMS is index matched to the optical fiber, and the PDMS layer would help smooth out minor surface roughness, reduce scattering loss and improve the optical coupling at the nanowire-fiber junction.

3.3 Optimization of the Nanowire-Fiber Coupling

To minimize the scattering loss at the nanowire-fiber junction and optimize the coupling efficiency, a number of issues have to be addressed, including the fabrication method of the tapered optical fiber, its tapering angle and surface smoothness.

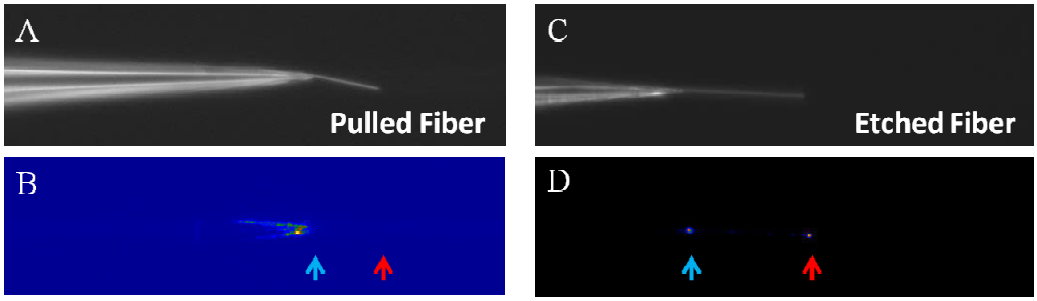

Figure 3.4 Nanoprobe coupling efficiency. A and B, Dark-field (A) and waveguiding (B) images of the nanoprobe fabricated from a pulled with a tapering angle of 12º. **C and D,** Dark-field (C) and waveguiding (D) images of the nanoprobe fabricated from an etched single mode optical fiber with rough (c) and smooth (d) surface and same tapering angle (4º). Blue and red arrows point to the tip of the optical fiber and nanowire, respectively.

Two different methods are commonly used to make sharp fiber tips: mechanically pulling the fiber while locally heating it with focused IR laser beam, and chemically etching the fiber with concentrated HF solution. Although the pulled fiber (Figure 3.4A) appears to have smooth surface that would minimize scattering loss from surface defects, the fiber core got stretched and thinned, which causes significant leakage of the waveguided modes throughout the tapered region (up to 50 μm from the tip). Thus, little light

propagated to the junction and was coupled into the nanowire (Figure 3.4B). The etched fibers (Figure 3.4C) have relatively rough surface due to etch pits which would give rise to surface scattering and reduce effective area of overlapping between the nanowire and the fiber. Nevertheless, the chemical etching does not deform the fiber core, which only starts to be exposed and tapered ~3μms from the tip. In this case, the light field is concentrated at the fiber tip where it is in physical contact with the nanowire (Figure 3.4D). Thus, the guided optical modes are effectively coupled with those in the nanowire.

We next investigated fibers of different mode structures for their ability of forming optical coupling with nanowires. Multimode fibers refer to those that carry more than one waveguiding mode. They usually have diameters in the 50-to-100 micron range for the light carry component. Multimode fiber offers high bandwidth at high speeds (10 to 100MBS - Gigabit to 275m to 2km) over medium distances. However, as illustrated in Figure 3.5A, light waves are dispersed into numerous paths, or modes, as they travel through the cable's core, which can cause signal distortion at the receiving end, resulting in a smudged special distribution profile of the output light intensity. As a result, the maximum optical output in a tapered multimode fiber is not concentrated at the tip although the input laser is a Gaussian beam. Light leaks out all over the tapered part of the optical fiber, with the maximum somewhere in the middle of the taper (indicated by the orange arrow in Figure 3.5B), and only a fraction of the total output was coupled into the nanowire.

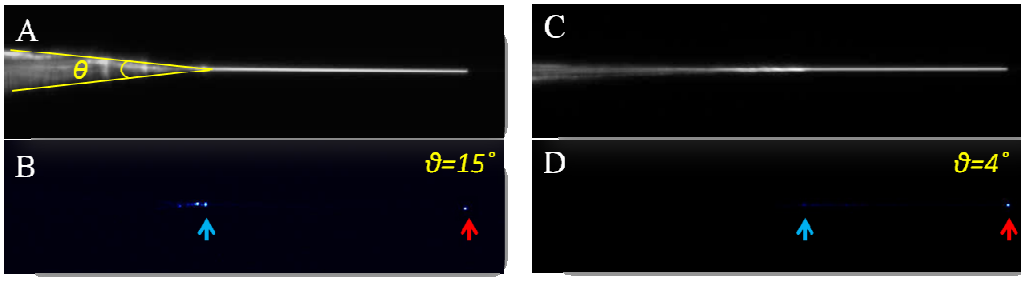

Figure 3.6 Dependence of optical coupling between nanowire waveguide and optical fibers on the cone angles of the fiber taper. A and B, Dark-field (A) and waveguiding (B) images of the nanoprobe fabricated from an etched single mode optical fiber a 15º cone angle. **C and D,** Dark-field (C) and waveguiding (D) images of the nanoprobe fabricated from an etched single mode optical fiber a 4º cone angle. Blue and red arrows point to the tip of the optical fiber and nanowire, respectively.

A better design of the nanowire probe is to use a single mode optical fiber. Single Mode cable is a single stand of glass fiber with a much smaller core diameter of 3-10 microns, depending on the working frequency, through which only the lowest order bound mode will propagate. Single mode fibers carries higher bandwidth than multimode fiber, but requires a light source with a narrow spectral width. Single-mode fiber also offers a higher transmission rate and up to 50 times more distance than multimode. The small core and single light-wave virtually eliminate any distortion that could result from

overlapping light pulses (Figure 3.5C), providing the least signal attenuation and the highest transmission speeds of any fiber cable type. In a tapered single mode fiber tip, the maximum optical output concentrates at the very tip where it has the best optical mode overlap with the nanowire. The effective overlapping ensure a much more efficient coupling at the nanowire-fiber junction. So for all the rest of the experiments, single mode optical fiber with a chemically etched taper was used for maximum coupling efficiency.

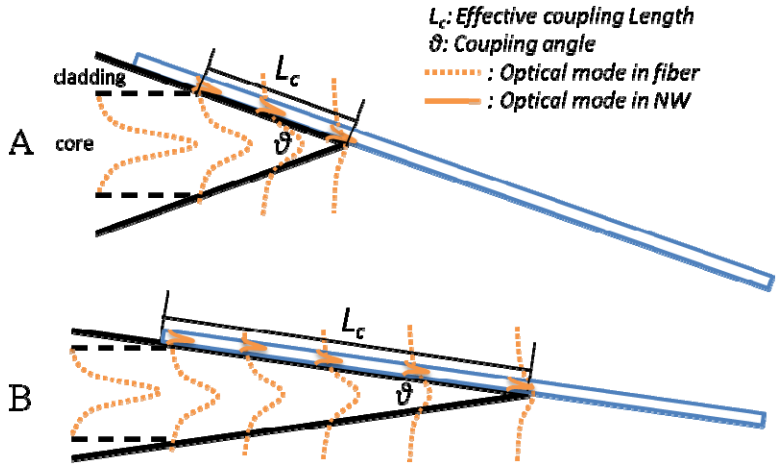

Figure 3.7 Dependence of nanowire-fiber coupling efficiency on the fiber tip taper angle. A, Schematic showing the optical mode overlapping of the nanowire and the optical fiber for fiber with a large taper angle. **B,** Schematic showing the optical mode overlapping of the nanowire and the optical fiber for fiber with a large taper angle. The solid black lines outline the side view of the optical fiber, and the sold blue lines outlined that of the nanowire. The black dashed lines outline the core of the optical fiber. The dashed orange lines and solid orange lines are the intensity profile of the optical modes of the single mode optical fiber and the nanowire, respectively, at different position near the nanowire-fiber junction.

We next examined the influence of the tapering angle on the coupling efficiency. Figure 3.6 presented two nanoprobes fabricated with etched fibers with the same level of roughness, but different cone angle of 15º and 4º, respectively. The fiber with small tapering angle (Figure 3.6 C and D) has much lower coupling loss at the junction than the one with larger tapering angle. This difference originates from the effective coupling length within which the optical modes in the fiber and the nanowire are overlapped. Single optical fibers are composed of a thin core (~3.5 μm in diameter for HP460 fiber from Thorlabs) and a thick cladding (~125 μm in diameter for HP460 fiber from Thorlabs). Illustrated in Figure 3.7, before the fiber tip tapers down to a critical diameter (the diameter of the core), the light carrying component of the fiber was not disrupted and the optical modes retains its original structure. When the taper progress to the critical diameter, the core is exposed and the optical mode confined in the core becomes more relaxed and starts to overlap with that of the nanowire. The effective coupling lengths

(L_c), throughout which the waveguiding modes of the nanowire and the nanoprobe overlap, depend on the cone angle of the taper. The longer L_c is, the more efficient the optical coupling will be. The coupling length for 4º tapered fibers is almost 4 times as long as that for 15º tapered fibers, resulting in a much more efficient coupling.

For fibers with small coupling angles, surface roughness from etch pits on the optical fiber is the major source of scattering loss at the nanowire-fiber junction. The smoother the fiber surface is, but less the scattering loss would be (Figure 3.8 C and D). Repeated rinsing with DI water and ethanol after the etching is an effective way to reduce such etching pits on the fiber surface.

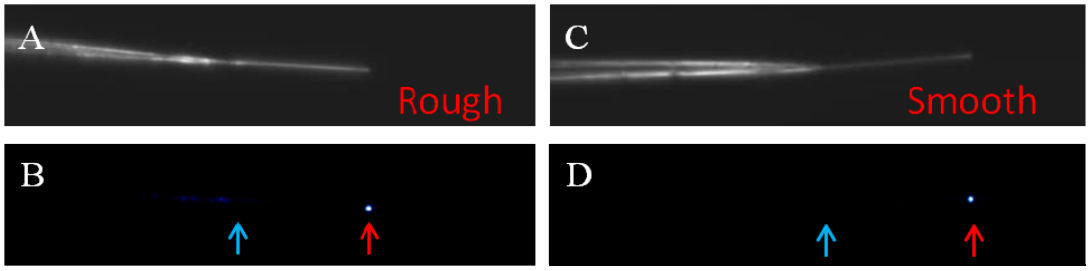

Figure 3.8 Nanoprobe coupling efficiency. A and B, Dark-field (A) and waveguiding (B) images of the nanoprobe fabricated from an etched single mode optical fiber with rough surface and a tapering angle of 4º. **C and D,** Dark-field (C) and waveguiding (D) images of the nanoprobe fabricated from an etched single mode optical fiber with smooth surface and a tapering angle of 4º. Blue and red arrows point to the tip of the optical fiber and nanowire, respectively.

3.4 Mechanical and Optical Properties of Semiconductor Nanoprobe

The overlapping of propagating modes between the fiber and the nanowire waveguide makes it possible for light traveling along the optical fiber to be coupled into the nanowire and propagates to the wire tip where it is re-emitted to the free-space (Figure 3.3D). Mechanical stability is a fundamental requirement for biological probes for intracellular sensing and imaging. The nanowire probe is extremely flexible due to its small size and high aspect ratio, yet is very robust mechanically, and can endure repeated deformation, bending and buckling without peeling off from the fiber. Figure 3.3D shows a SnO_2 nanowire being buckled with a tungsten needle, the nanowire was still firmly attached to the fiber tip. Figure 3.9C shows a SnO_2 nanowire being deformed by 30º with a tungsten needle, and the intensity of the nanowire tip emission did not show significant fall-off compared to that when it's free of mechanical deformation (Figure 3.9B), indicating that the optical coupling also remained undisturbed.

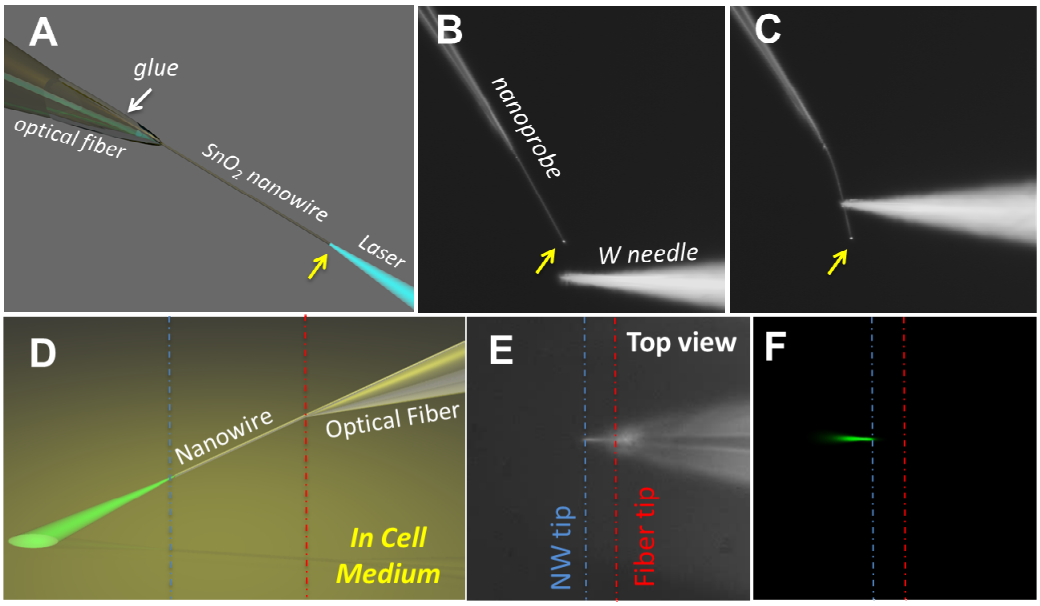

Figure 3.9 Design of nanowire-based optical probe for single cell endoscopy. **A,** 3D Schematic showing blue laser waveguided through a nanoprobe constructed by gluing a SnO_2 nanowire to the tip of a tapered single mode optical fiber. **B and C,** Flexibility and Robustness of the Nanoprobe. Dark field images of a nanoprobe, which was coupled to a 442nm blue visible laser, before **B** and during **C** deformation by a tungsten needle. The yellow arrows in **A-C** points to the nanowire tip where the waveguided light was emitted into free space. **D-F,** Intensity profile of the nanoprobe emission. Schematic drawing (**D**), dark field (**E**) and fluorescent (**F**) images of a nanoprobe immersed in cell culture medium that illuminated fluorescent proteins with the blue light emitted from the nanowire tip. (**E-F**) are the top view of a real nanoprobe device illustrated in (**D**).

Highly efficient optical coupling between the nanowire and the optical fiber is crucial in order for the nanoprobes to function as localized light sources. The coupling loss, which originates mainly from scattering and mode mismatch, can be suppressed by adjusting the tapering angle, smoothness and the intensity profile of the tapered tip of the optical fiber (see Section 3.3 for details). By optimizing these parameters, light escaping from the junction was kept at minimal level. To test the waveguiding capability of the nanoprobes in physiological environment and to visualize the intensity distribution of the tip emission, the nanoprobe was immersed in cell culture media, typically containing weakly fluorescent proteins that can be optically excited by the blue laser that was input into the fiber (Figure 3.9D). Despite the small dimensions (100-250nm) of the nanowires, the large increase in environmental refractive index (Δn~1.33) did not affect the optical coupling or light propagation, benefiting from the high refractive index of SnO_2. The profile of fluorescence intensity follows that of the nanoprobe emission (Figure 3.9E and F). For a highly efficient nanoprobe, the optical output is closely confined to the

nanowire tip, thus offering highly directional and localized illumination. On the contrary, a poorly coupled nanoprobe would have light leaking out all over the tapered optical fiber tip, resulting in a diffused and divergent output beam (Figure 3.10).

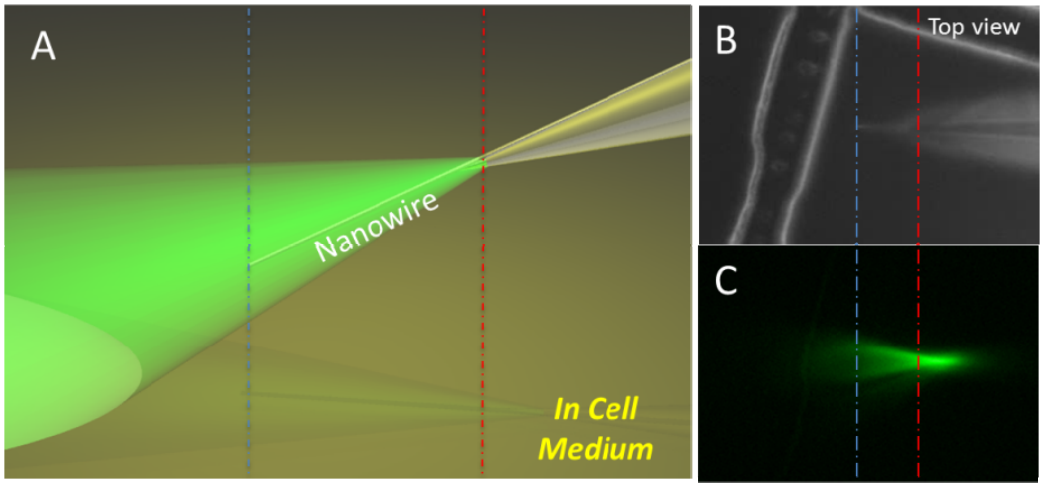

Figure 3.10 Illumination by the taped optical fiber. A, Schematic of the tapered optical fiber illuminating fluorescent proteins in the cell medium by the blue light (442 nm) delivered through it (nanoprobe with poor coupling between nanowire and tapered region of optical fiber. Blue and red dashed lines indicate nanowire and optical fiber tips, respectively. **B and C,** Dark-field image of the nanoprobe (tapered optical fiber) placed in the cell medium (**B**). Fluorescence image of the nanoprobe broadly illuminating fluorescent proteins in the cell medium by the blue light (**C**).

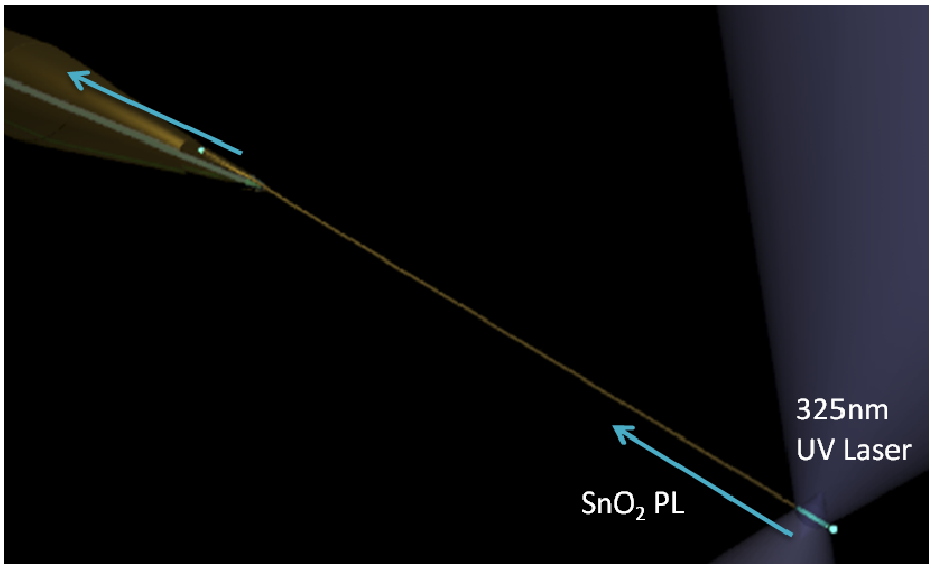

Figure 3.11 Optical signal collection through a semiconductor nanowire probe. 3D schematics of the experimental setup for the demonstration of the collection of the SnO_2 nanowire photoluminescence with the nanoprobe.

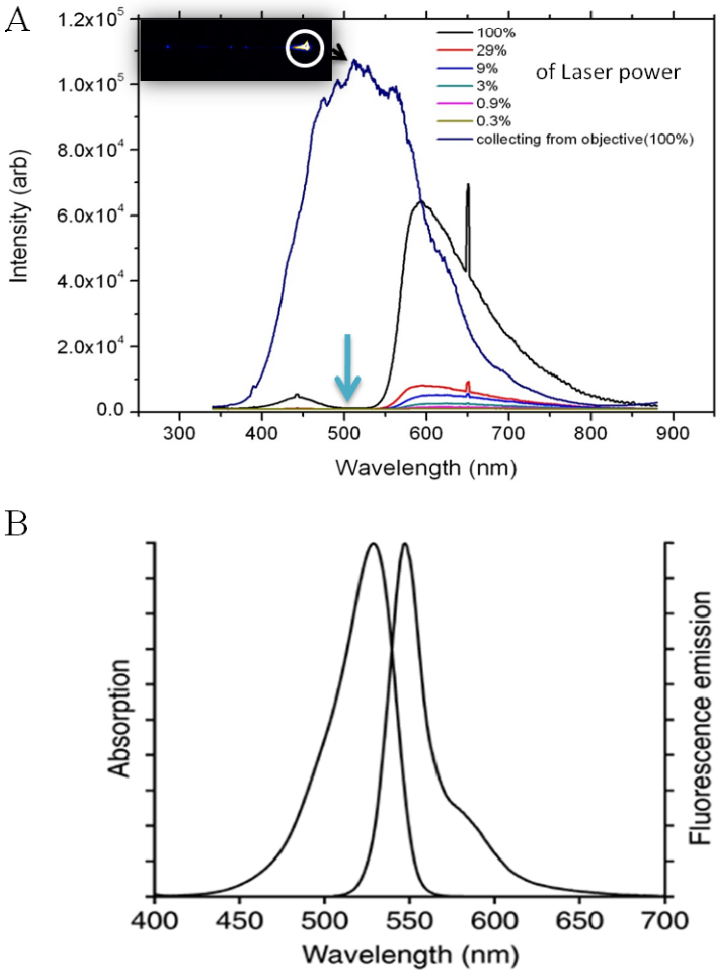

Figure 3.11 Optical signal collection through a semiconductor nanowire probe. **A,** SnO_2 photoluminescence spectrum collected through the microscope objective (dark blue) v.s. spectra collected through the nanoprobe under different laser intensity. The blue arrow points to the dip in the nanoprobe collected spectra that correspond to the absorption peak of R6G. Inset is the fluorescent image of the nanoprobe being illuminated at the nanowire tip (circled) by a focused UV laser. **B,** Absorption and fluorescence spectra of R6G.

The highly localized illumination offered by the nanoprobe enables its application as a micro "spot light" in air, in solution and even in cellular environment. The extremely concentrated light field combined with the small probe size, promise an ideal platform for single cell endoscopy. However, single cell endoscopy does not rely merely on subcellular illumination but on localized collection of the optical cellular response to the illumination as well. So it is necessary to explore the reverse process, in which the local light signal is collected through the nanowire tip and back coupled into the optical fiber that is connected with a spectrometer or a photodiode.

Figure 3.11 shows a prototypical experimental setup designed to investigate the feasibility of picking up local signal with the nanowire probe. A 325 nm Helium-Cadmium laser UV laser was focused on the tip of the SnO_2 nanowire. The photoluminescence (PL) of the SnO_2 propagates along the nanowire back to the nanowire-fiber junction, where the waveguiding mode of the nanowire couple with that of the optical fiber. The PL signal then propagates along the fiber to its distal end which is coupled to a nitrogen cooled UV-Visible spectrometer. We used multimode fiber for this experiment to avoid frequency cutoff, because the SnO_2 photoluminescence spans the entire visible spectrum and single mode fibers usually have narrow working frequency window.

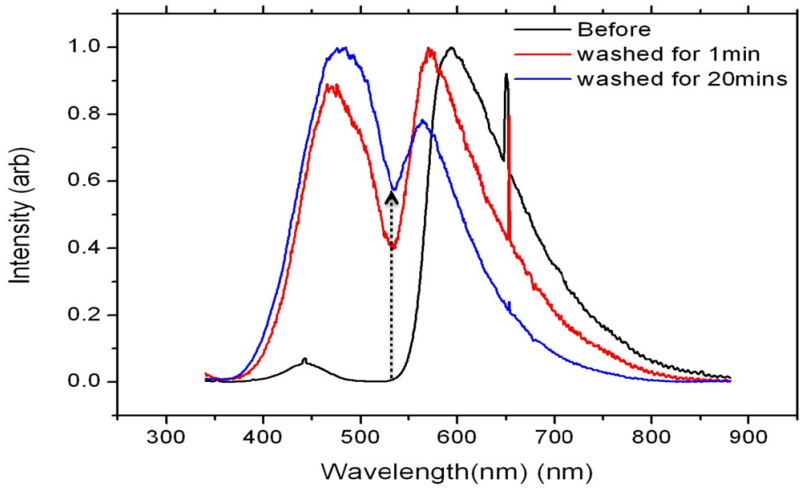

Figure 3.12 Normalized SnO_2 PL spectra collected through the nanoprobe before and after washing. The black curve corresponds to the spectrum prior to washing. The red and blue curves correspond to the spectra after the probe has been washed in ethanol for 1 and 20 mins, respectively. The dashed arrow points to the spectral dip that corresponds to the R6G absorption.

Prior to the experiment, we dipped the nanowire into 10 μM Rhodamine 6G (R6G) solution and then leave the probe air dried. There is a thin layer of R6G dye physically absorbed onto the nanowire surface. Such a thin layer of dye did not introduce significant change in the SnO_2 PL spectrum when the signal was collected through the microscope objective (Figure 3.11A. dark blue curve). The spectrum measured this way composed mostly of SnO_2 photoluminescence emitted into free space directly from the tip of the nanowire where it was excited. However, when the signal was collected through the nanoprobe, there existed a large dip in the spectrum from 450 nm to 550 nm, which corresponded to the absorption peak of R6G (Figure 3.11B). That can be attributed to the absorption of the SnO_2 PL while it propagated along the nanowire to the nanoprobe junction by the dye molecules absorbed throughout the entire nanowire. This observation offers direct evidence that the optical coupling between the nanowire and the optical fiber is strong enough to collect photos that propagate in the nanowire. And the SnO_2 PL collected directly from the tapered tip of the optical fiber does not overwhelm the

nanoprobe collected spectrum even for the multimode fiber with relatively large numerical aperture.

We then washed the dye-loaded nanoprobe in ethanol for 1 and 20 mins to partially remove the R6G molecules. As expected, the spectra collected from the nanoprobe after washing shows a significant decrease of the spectral dip from R6G absorption, although the position of the dip remains constant, with the deepest point at ~530 nm (Figure 3.12). The intensity of the SnO_2 PL peak at ~ 450 nm shows a consistent increase, also indicating a recovery of the broadband SnO_2 signal from the dye absorption.

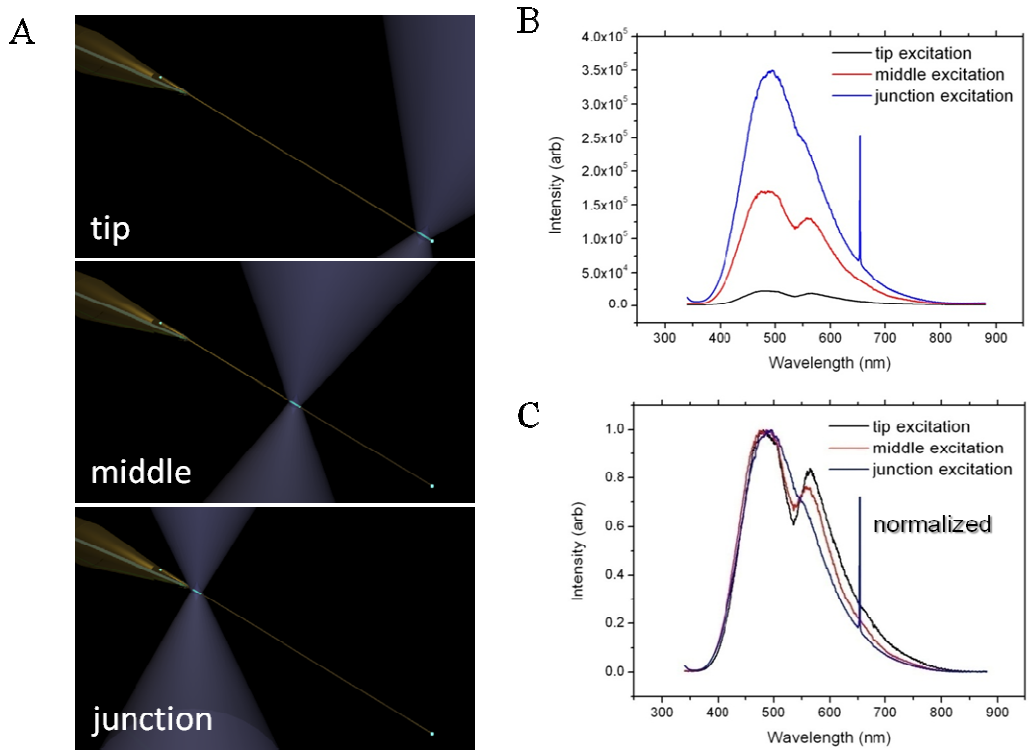

Figure 3.13 Nanoprobe spectra at different excitation position. A, Schematics showing the 3 positions of the laser excitation: Nanowire tip (upper), middle of the nanowire (middle), nanowire-fiber junction (lower). **B-C,** original and normalized spectra collected through the nanoprobe at positions corresponding to **A**.

Spectra measured when the laser excite the nanowire at different positions (Figure 3.13A) show 2 interesting trends as well. As shown in Figure 3.13B and C, as the laser excitation position moves from the tip of the nanowire to the junction, the signal intensity increase significantly and the dip due to the R6G absorption becomes less prominent. The intensity increase can be attributed to the shorter light path in the nanowire, which has a relatively high propagation loss, and an increased contribution from the far field direct collection through the tapered fiber tip of the SnO_2 PL emitted into the free space. Same reason can be used to explain the relaxation of the spectral dip. As the light path in the nanowire shortens, the amount of R6G along that path also decreases, resulting in a lower

absorption. As the far field component in the spectra increases, SnO2 PL dominate the spectrum and it resembles more of the spectrum collected from the far-field objective lens. This result indicated that in order to achieve the localized near field collection through the nanowire tip, the nanowire have to be long enough so that the far field background can be negligible. This critical nanowire length depends on the properties of the nanowire, the type and tip shape of the optical fiber, as well as the optical coupling at the junction.

3.5 **Metal Nanowire Probes**

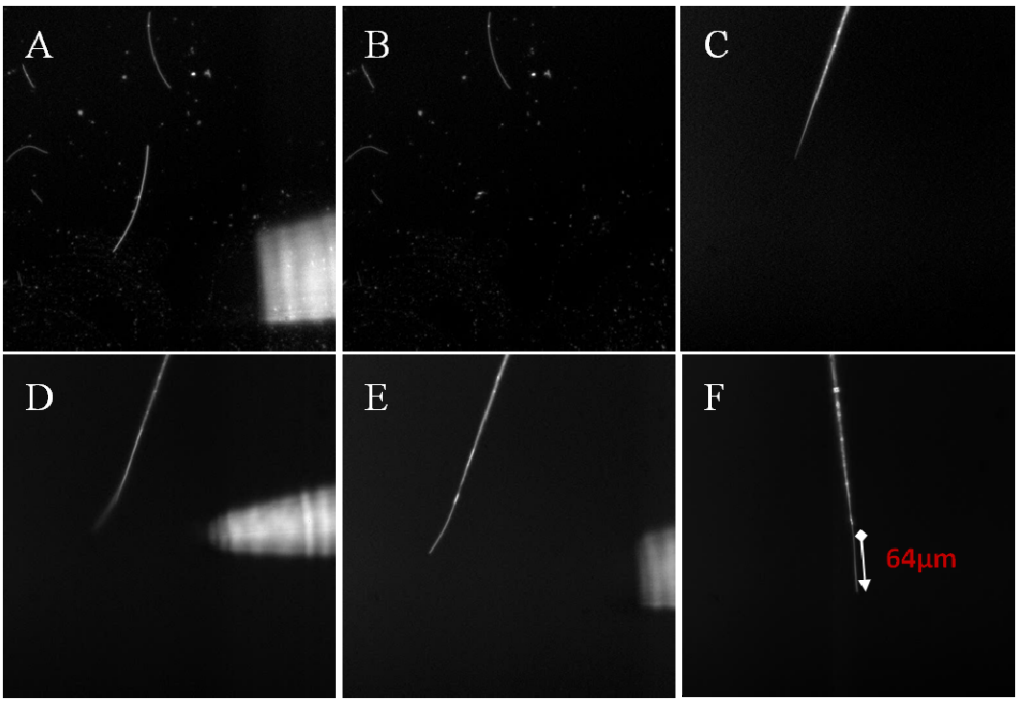

Figure 3.14 Fabrication Procedure of Ag nanowire probe. A, Dark-field image of a 140 μm long, 100 nm diameter Ag nanowire sitting on the substrate. **B,** Dark-field image of the substrate after the nanowire was picked up by the manipulator. **C,** Dark field image an extremely thin tapered single mode fiber tip. **D,** Dark-field image of the fiber tip with the Ag nanowire attached. **E,** Dark-field image of the nanoprobe after the Ag nanowire orientation was adjusted. **F,** Dark-field image of the nanoprobe after glue was applied. The protruding length of the nanowire from the fiber tip was measured 64 μm, and the overlapping section with the optical fiber is 76 μm.

In the previous chapter, we demonstrated that Ag nanowire as a low-loss plasmonic waveguide with tight spatial mode confinement in 2D, and that it can couple effectively upon physical contact with a dielectric nano-waveguide. In this section, we will show that Ag nanowire can also be optically coupled to a tapered optical fiber tip and fabricated into a plasmonic nanoprobe.

The fabrication procedure of plasmonic nanoprobe is illustrated in Figure 3.14. First, Ag nanowires dispersed in Ethanol was drop casted on to a soft substrate and a micromanipulator needle was used to pick up a Ag nanowire of suitable lengths and diameter (Figure 3.14A-B) and transfer the nanowire to the tapered tip of an optical fiber (Figure 3.14C). The large contact area between the glass and the nanowire make it easy for the nanowire to detach from the needle and attach to the fiber (Figure 3.14D). Ag nanowire is much softer, more flexible and generally smaller than semiconductor nanowires used previously. As a result, the nanowires often deflect or bent away from the optical axis of the fiber after attaching to it, and it is necessary to press the nanowire to the fiber so that the entire nanowire portion that is overlapping with the fiber tip is in close physical contact with the glass surface. Then PDMS or epoxy glue can be applied in the same fashion as in the case of semiconductor nanowires, and the bonding is usually strong enough for the nanowire to endure the surface tension during solution processes (Figure 3.14).

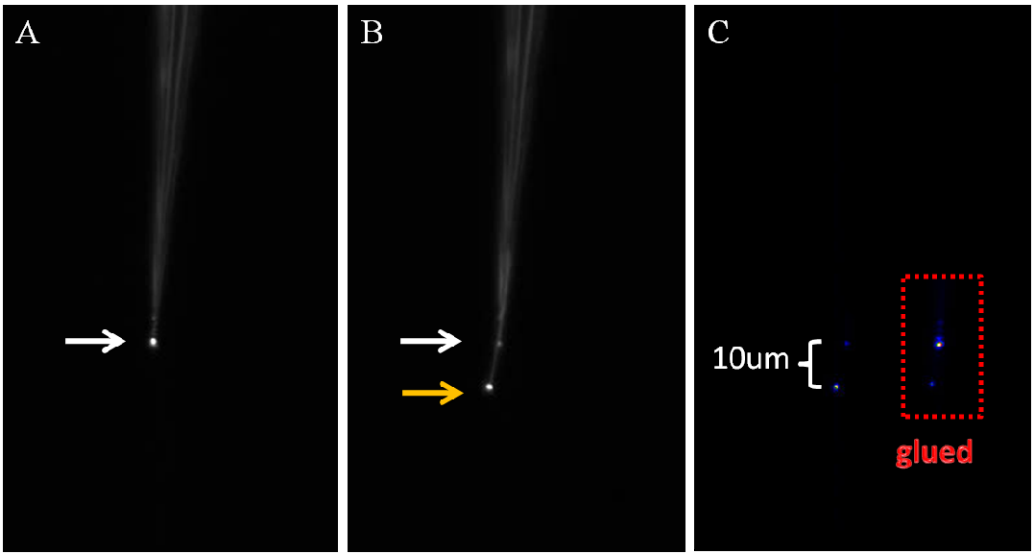

Figure 3.15 Optical Coupling between Ag nanowire and single mode optical fiber. A, Dark-field image of a bare tip of chemically etched single mode optical fiber coupled to a 650 nm red laser. **B,** Dark-field image of a Ag nanowire probe fabricated from the fiber in **A**. The white and yellow arrows points to the tip of the fiber and the tip of the nanowire, respectively. **C,** The waveguiding image of **B**. Inset is the waveguiding image of the probe after glue has been applied.

Figure 3.15 shows the optical images of a Ag nanowire probe with light propagation at different stage of fabrication. After Ag nanowire attachment, the majority of light output transferred from the tip of the fiber tip for a bare tapered optical fiber (Figure 3.15A) to the tip of the Ag nanowire (Figure 3.15B). This fiber-nanowire is amazingly high efficiency compared to the SnO_2-Ag coupling we discussed in the previous chapter. This is in part due to the angular dependence of the dielectric-metal coupling. The complete

overlap of the propagation direction of the optical modes in the fiber with that of the plasmonic modes in Ag nanowire is the optimized geometry for the most effective coupling. Fortunately, the Ag-glass interaction is much larger than SnO_2-glass interaction, plus Ag nanowire is considerably smaller and lighter than SnO_2 nanowire, so Ag nanowire has a very firm attachment to the glass surface, and unless the nanoprobe has to undergo solution processes, gluing is not a necessity.

However, unlike semiconductor nanowires for which glue application enhance the fiber-nanowire optical coupling by index matching and smoothing of surface defects that serve as scattering centers, in the case of Ag nanowire, the glue application has a negative effect (Figure 3.15C). This is because the plasmonic modes in Ag nanowire is very sensitive to its dielectric environment, and polymer coating at the junction brings a huge increase in the refractive index of the cladding dielectrics of the nanowire that makes the coupling less effective. Another possibility is that the polymer goes in between the nanowire and the fiber, creating a larger gap, which also decreases the effective overlapping of the plasmonic modes to the optical modes.

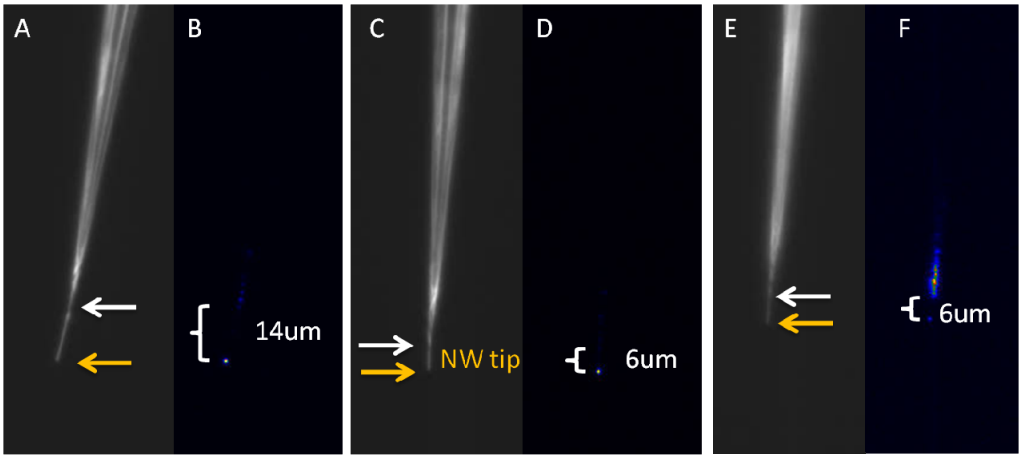

Figure 3.16 Dependence of the nanowire-fiber coupling efficiency on Ag nanowire length and diameter. A-B, Dark-field and waveguiding image of a Ag nanowire probe with a 14 μm nanowire protruding length and the Ag nanowire diameter of 120 nm. **C-D,** Dark-field image of the Ag nanowire probe with a 6 μm nanowire protruding and the Ag nanowire diameter of 120 nm. **E-F,** Dark-field image of the Ag nanowire probe with a 6 μm nanowire protruding length and the Ag nanowire diameter of 60 nm. The white and yellow arrows points to the tip of the fiber and the tip of the nanowire, respectively.

The total optical output intensity from the Ag nanowire doesn't solely depend on the coupling efficiency at the junction. It also depends on the length of the suspended portion, defined here as the protruding length, of the Ag nanowire, because when it comes to plasmonic waveguide, the propagation loss becomes too significant to overlook. For a simple comparison, we fabricated 2 nanoprobes with the same Ag nanowire and optical fiber, only with different protruding lengths (Figure 3.16 A and C). The apparent

coupling efficiency, which is defined as ratio between the nanowire tip emission and the sum of the nanowire tip emission and the scattering loss at the tip of the optical fiber, increases from 54% for the 14 μm probe (Figure 3.16 B) to 72% for the 6 μm probe (Figure 3.16 B). If we take the coupling loss at the junctions for the same nanowire and fiber as a constant, apparently the Ohmic loss of plasmon propagation in the Ag nanowire has a non-negligible contribution to the output intensity from the nanowire tip.

Another important factor for Ag nanowire-optical fiber coupling and output intensity is the diameter of the Ag nanowire. Figure 3.16 E-F shows a 60 nm Ag nanowire probe, for which the same optical fiber tip was used as in the previous 120 nm Ag nanowire probe. The junction coupling loss is appreciably larger and apparent coupling efficiency is abysmally lower at only 2%.

3.6 **Conclusions**

In this chapter, we have discussed the design and fabrication of the nanoprobe system based on single nanowire waveguides and an optical fiber with tapered tip. Of different types of optical fibers and method to taper the fiber tip, chemical etching of single mode fiber has demonstrated to be the best material for nanoprobe fabrication. The effective optical coupling of the tapered single mode optical fiber to both semiconductor and metal nanowire nanoprobes has led to the construction of highly efficient nanowire probes. These probes are mechanically robust and flexible and can withstand repeated bending, deformation and even buckling without significant deterioration in optical performance, which offers an ideal instrumental platform for out subsequent effort of using these nanoprobes in chemical sensing as well as single cell endoscopy and spot delivery.

Chapter 4
pH Sensitive Nanoprobe

The measurement and monitoring of chemical concentration gradients or spatial heterogeneities are crucial requirements in many area including catalytic and analytical chemistry, physiology, toxicology, cell biology and material science. For high definition spatial and temporal sensing of concentration profile, especially for the kinetic processes in single cell studies, chemical probes of minute sizes and fast response are desired. NSOM probes, which refers to metal coated tapered optical fibers with a small aperture, has found successfully application for submicrometer chemical sensors with excellent detection limits, photostability and fast response time[145,146]. Although these fiber tips can have subwavelength apertures that ensure a small sample volume, the probe tip optical throughput, which is proportional to the diameter of the aperture, **d**, divided by the wavelength of light, **λ**, raised to the fourth power, or Optical Throughput ~ $\mathbf{(d/\lambda)^4}$, becomes exceedingly low. In addition, although these probe tips tip can be as small as 100 nm at the very end, the reflective metal coating which is as thick as 100 nm limits the overall size of the tip dimension. In addition, these tips taper down from a large base and are impractical for procedures that require single cell insertion.

We have discussed in Chapter 3 the fabrication and properties of nanowire based optical nanoprobe. In this chapter, we are going to describe a technology of tansforming this optical nanoprobe into a pH sensor with internal calibration, fast response time and good photostability and reversibility when combined with near-field photopolymerization. The pH-sensitive nanoprobe was able to report the pH change in the micro-droplet (<10 pL in volume) containing buffer solution at different pH with the excitation of blue light waveguided on the nanoprobe.

4.1 **Property of Fluorescein and Its Derivatives**

Fluorescent pH indicators show increased sensitivity and flexibility over conventional chromogenic indicators (phenolphtalein, phenol red…) and microelectrode techniques. Fluorescein and its derivatives, which exhibit pH denpendent fluorescence, are often used in intracellular pH measurements that are performed in many cell viability assays and cell physiological studies, because of their pH sensitivity and high fluorescenc quantum yield.

Fluorescein and many of its derivatives exhibit multiple, pH-dependent ionic equilibria[147-149]. Figure 4.1[150] shows the ionic equilibria of underivatized Fluorescein. When the solution pH is above 9, both the phenol group and the carboxyl group are almost totally de-protonated. As the pH decrease, the phenol group with a pKa of 6.4 is first protonates to yield the fluorescein monoanion. Then the carboxylic group (pKa <5)

is acidified to produce the neutral species of fluorescein. Further decrease of pH generates a fluorescein cation (pKa ~2.1).

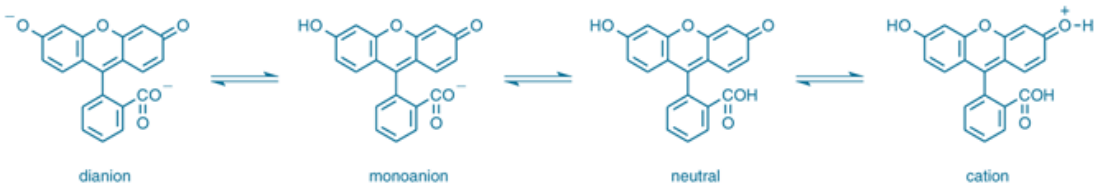

Figure 4.1 pH dependent ionic equilibria of underivatized fluorescein. The anions are the only fluorescent species.

Of all the ionic and neutral species of fluorescein, the monoanion and dianion are the only two that exhibit fluorescence, with quantum yields of 0.37 and 0.93, respectively[149]. The pH-dependent absorption spectra of fluorescein shown in Figure 4.2A[150] show a distinct blue shift due to the formation of protonated species as pH decrease, which is also accompanied by a decreased. However, since the quantum yield of the dianion is much higher than that of the monoanion for most fluorescein derivatives, its fluorescence dominate the emission spectra even in acidic solution. This is especially prominent when the excitation is close 490 nm, at which dianion has the highest absorption. The position and shape of the emission peak are relatively independent of pH (Figure 4.2B), but the fluorescence intensity is dramatically reduced at acidic pH due to the reduce in quantum yield of the majority fluorescent species. Chemical substitutions of fluorescein may result in red or blue shift of the absorption and fluorescence peaks, and may also affect the dissociation constant of the protonated specie, but spectral characteristics and their pH dependence are generally maintained.

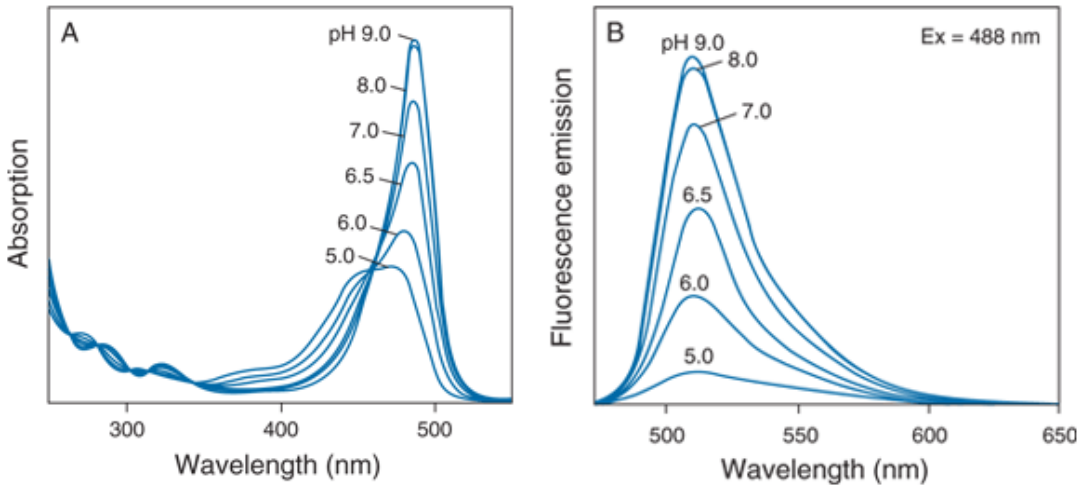

Figure 4.2 The pH-dependent spectra of fluorescein. A, absorption spectra. **B,** emission spectra.

4.2 **Synthesis of pH Sensitive Fluorescent Dye for Photopolymerization**

To incorporate the fluorescein dye into a polymer matrix, a fluorescein derivatives containing reactive substituent that can engage in facile polymerization reactions is required. However, such derivatives are not commercially available. Here, we synthesized the amide derivative of fluorescein, N-fluoresceinylacrylamide (FLAC), molecular structure shown in Figure 4.3, through the reaction of acryloyl chloride (Figure 4.3, middle), which contains a vinyl group for polymerization, and aminofluorescein, or fluoresceinamine (Figure 4.3, left), which contains an amine group on the phenyl ring as an anchor for facile coupling reactions[151].

The amide derivative, FLAC, was formed by reacting 2:1 stoichiometric quantities of acryloyl chloride with fluoresceinamine in dry acetone[145], which was obtained by drying HPLC-grade acetone in molecular sieve. The mixture was stirred for ~1 hr at room temperature until most of the product precipitated. The product was collected by filtration and washed by acetone and CH_2Cl_2, and then air-dried.

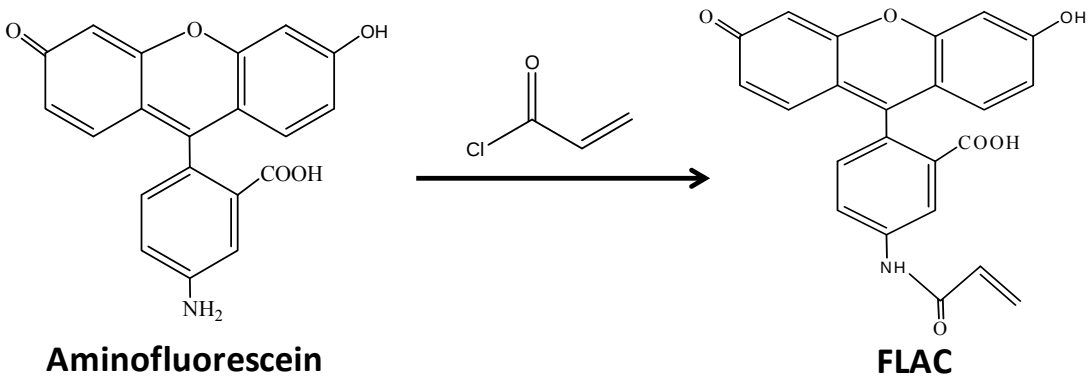

Figure 4.3 Acylation reaction of aminofluorescein.

The absorption spectra of FLAC (Figures 4.4) generally follow the shape of that of fluorescein and showed strong pH dependence. The dianion absorption reaches its maximum at 490 nm, while the monoanion absorption peaks at 440 nm. The fluorescence of the FLAC shows a significant increase compared to aminofluorescein (Figure 4.5), which can be attributed to the decrease in the intramolecular resonance of the nitrogen lone electron pair with the π-electron system of the ring, as well as in its participation in excited-state transfer processes. In FLAC, electron withdrawal by oxygen of the carbonyl group makes the amide nitrogen a much poorer source of electrons than the amine nitrogen.

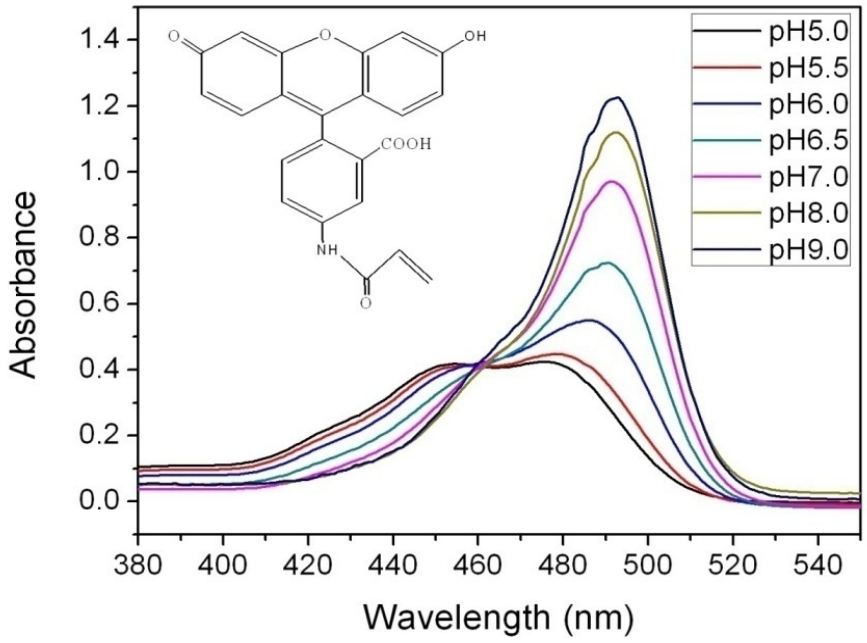

Figure 4.4 UV-Vis absorption spectra of FLAC in buffer solutions of different pH. Inset: molecular structure of FLAC in its protonated form.

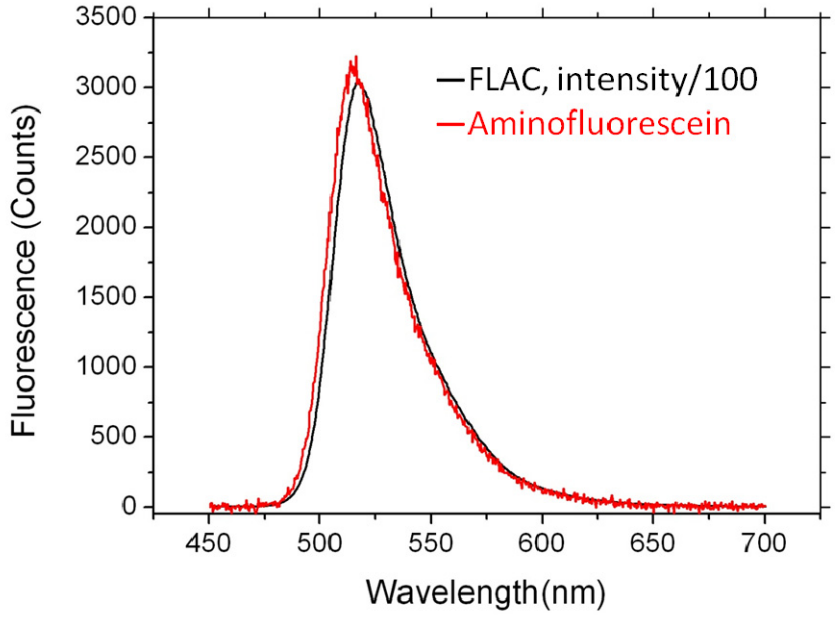

Figure 4.5 Fluoresent spectra of FLAC and aminofluorescein. The black curve is the FLAC fluorescence divided by 100. The red curve is the aminofluorescein spectrum. The buffer strengths of both solutions are 20 mM and the dye concentrations are both 16.7 μM. Excitation wavelength is 442 nm.

4.3 **Photopolymerization**

The pH sensitive nanoprobe was fabricated by capping the tip of the nanowire probe with the copolymer of acrylamide and FLAC in the presence of a crosslinker N,N-methylene bis(scrylamide) (Figure 4.6A) through photopolymerization, following the previous reported procedure[145].

The solution for polymerization on the fiber surface is a mixture that consists of three solutions[152]. 1. FLAC was dissolved in ethanol with a concentration of 15 mM. 2. Acrylamide was dissolved in 0.1M phosphate buffer (pH 7.4) with a concentration of 6.5M. 3. N, N-methylenebis(acrylamide) was also dissolved 0.1M phosphate buffer (pH 7.4), but with a concentration of 0.15 M. All the solutions were stored at 5°C. Then, 4 ml of FLAC solution was then mixed with 10 ml of acrylamide solution and 40 ml of N, N-methylenebis(acrylamide) solution to form the monomer stock solution. The stock solution can be stored in a refrigerator for about 1 month without evident polymerization.

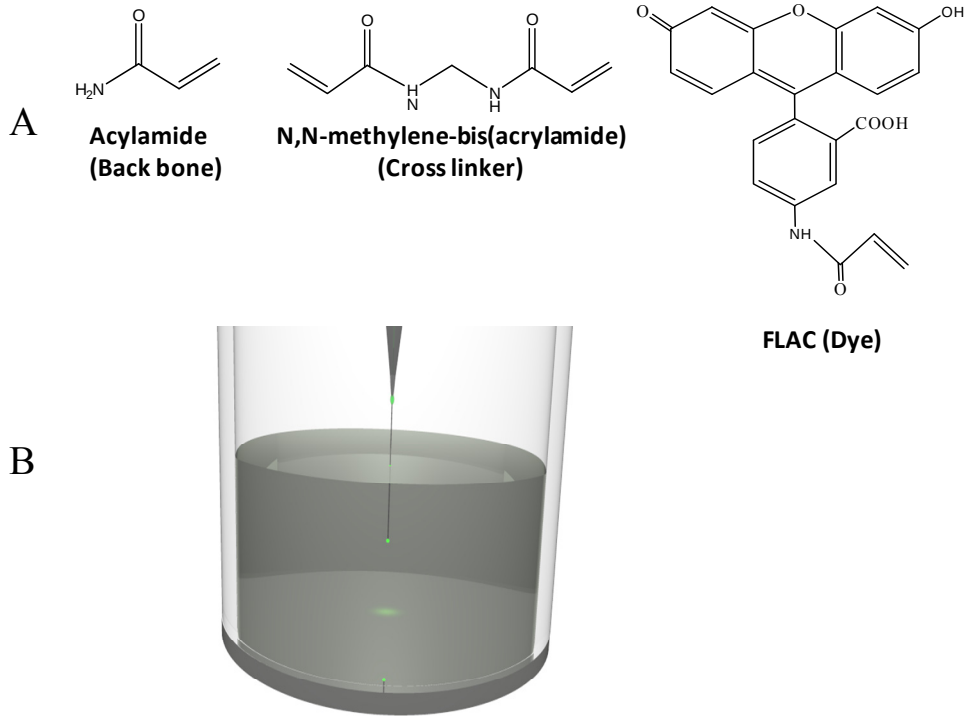

Figure 4.6 Surface photografting of pH sensitive polymer on nanoprobe tip. **A,** The molecular structures and functions of the 3 monomers. **B,** Schematic illustrating the photopolymerization process. The nanowire tip was inserted into the monomer solution while the opposite end of the optical fiber was connected with the 442 nm laser. Light emitted from the nanowire tip drove the polymer grafting on the end faces of the nanowire tip.

To ensure the grafting of the polymer on the nanowire surface, surface activation of the SnO_2 surface is necessary. The nanoprobe tips were first silanized with APTES (10%, pH 3.45) for about 1 hr and then dried in air for another hour[145]. To minimize possible dye attachment to the sidewall of the nanoprobe, only the tip region of the nanowire was immersed into the APTES solution. After silanization, nanowire tips were sensitized in a 0.2 M benzophenone/cyclohexane solution for about 15 min[153].

The photopolymerization of the monomer was performed in a passive N_2 environment at an elevated temperature (Figure 4.6B). The reactor used for photopolymerization was a small glass bottle with three holes in its cover, through which the N_2 flushing tubes and the nanoprobe tip was inserted into the monomer solution. An oil bath was used to control the reaction temperature at 50 ºC. Being a radical process, this graft polymerization is retarded by oxygen. So prior to the reaction, polymer solution was bubbled with N_2 for about 20 mins before laser light was directed into the fiber tip and the N_2 atmosphere was maintained during the reaction. Laser light of 442 nm from a HeCd laser was coupled into the fiber and transmitted to the tip where the photopolymerization was initiated directly on the silanized surface. Reaction time of 5-10 min was needed for the polymerization process. A XYZ translation stage was used to control the position of the nanoprobe so that only the tip was in contact with all the solutions and the junction was not immersed. Long nanowires a generally favored for the selective grafting process for easier control of the nanoprobe position by the translation state. After the polymerization, the nanoprobe was washed in water and ethanol in turn to remove unpolymerized dye.

Figure 4.7 Fabrication of pH sensitive nanoprobe. A, dark field image of a probe before the coating of fluorescent polymer. **B,** waveguiding of 442nm laser coupled into the probe. **C,** Dark field image of a probe after polymer coating. **D,** PL image of the dye-coated probe in air. Scare bar: 5 μm

The advantage of photo grafting to thermal grafting is that by photopolymerization, the effective sensor size is controlled by the area from which the light exits, which in the case

of the nanoprobe is the tip of the nanowire. Figure 4.7 show the dark field, waveguide and fluorescence images of a nanoprobe before and after the photopolymerization.

4.4 Calibration Curve

Nanoprobe pH sensors were tested with eight different buffer solutions from pH 4 to 9. The nanoprobe was mounted on the micromanipulator and inserted into microdroplets of buffer solutions of different pH pre-patterned on a PDMS substrate. The 442 nm HeCd laser beam was coupled into the fiber as optical excitation to the fluorescent polymer. A 50x long working distance objective (Nikon) was used to collect the fluorescent signal from the tip of the nanowire, while the tip of the optical fiber was kept out of the field of view. The tip emission spectra of the nanoprobe showed strong pH dependence (Figure 4.7). At high pH, polymer fluorescence was dominant by the 515 nm emission from the dianion of FLAC, while at low pH, emission from the monoanion appeared as a shoulder around 550nm.

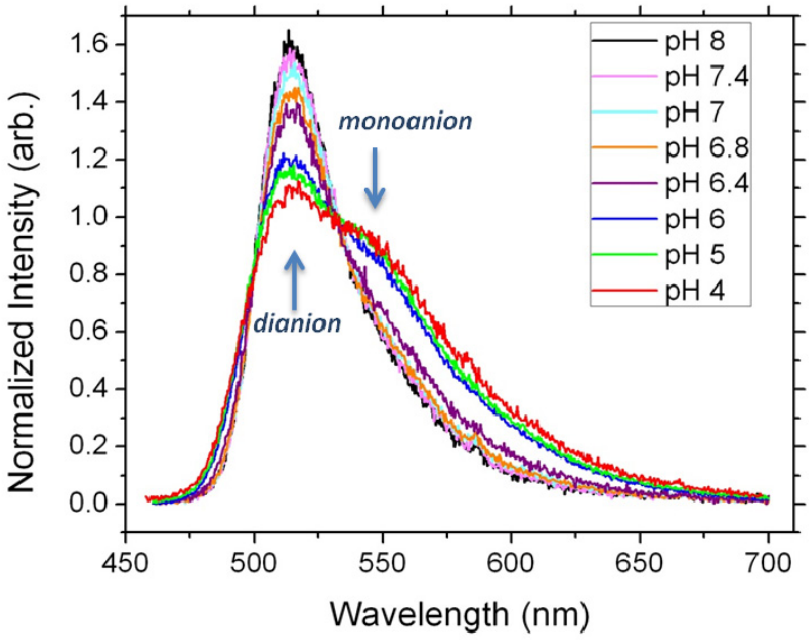

Figure 4.7 Normalized probe tip fluorescence spectra in buffer solutions of different pH.

We have discussed above, that the fluorescence spectra of fluorescein derivatives are usually dominate by emission of the dianion even in acidic solution, due to its much higher quantum yield compared to that of the monoanion. This still holds true for FLAC-acrylamide copolymer. However, by using an excitation wavelength that is on resonance with the absorption maximum of the monoanion (440nm, Figure 4.4), we can enhance the monoanion emission by boosting its absorptivity. As evident from the emission spectra

normalized to the mid-point of the monoanion and dianion peaks, the monoanion emission becomes comparable to that of the dianion for acidic pHs.

The intensity ratios at 515 nm and 610 nm were used to construct the calibration curve of the nanoprobe, which showed a sharp transition between pH 5-9 (Figure 4.8). The intensity ratios of other wavelengths can also be used to quantify pH as long as the ratios are large enough to five accurate calibrations in the physiological range. Although different sensors have mildly different spectra and calibration curves, which may be credited to the difference in dye distribution in the copolymer and the geometry of the end facet of the nanowire.

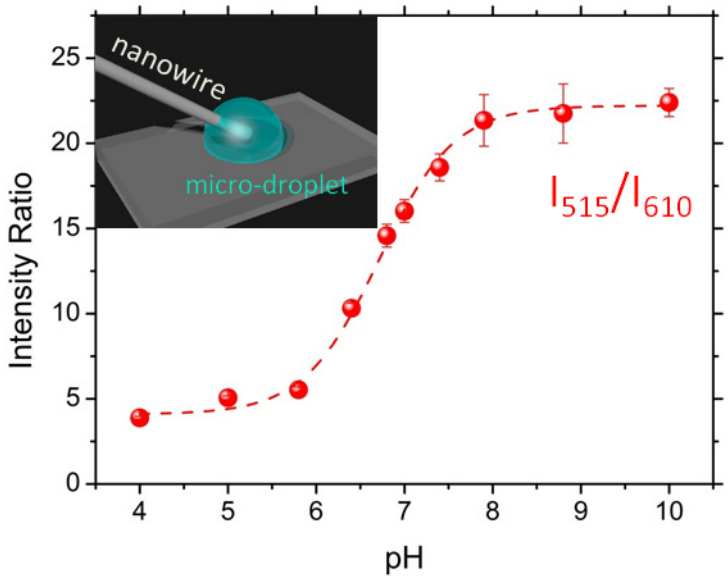

Figure 4.7 Calibration curve of the dye-coated nanoprobe in a microdroplet containing buffer solution at different pH. Inset indicates the schematic showing the measurement set-up with the nanowire tip immersed in the mircrodroplet of buffer solution)

The laser power used in the experiment is only 3 mW, and that drop to well below 1 mW at the tip of the nanowire, depending on the coupling efficiency at the nanowire junction, as well as the laser-fiber coupling efficiency at the opposite end. Under such small laser power, no evidence of photo-bleaching was observed after repeated experiments over a long time period.

4.5 **Conclusions**

In this chapter, we discussed one application of the optical nanowire probe as a pH sensor through surface photopolymerization. The nanoprobe pH sensors exhibit internal calibration, photostability and reversibility. The pH-sensitive nanoprobe was able to report the pH change in the picoliter sized micro-droplet containing buffer solution at different pH with the excitation of blue light waveguided on the nanoprobe. The miniaturization of the sensor not only permits small sample volume and offers high

special resolution, but also permits a fast response time and offers high temporal resolution because the analytes have immediate access to the dye on the sensor tip.

Chapter 5
Nanowire-based Single Cell Endoscopy

Nanostructured smart probes that can be safely internalized into biological cells hold enormous potential since selective targeting[154], efficient gene or drug delivery[155-158], sensing molecular dynamics and imaging fingerprints[159-168] are in critical demand for understanding complex biological events and theranostics. However, our effort to use them for optical communication cross the cellular membrane at the subwavelength level remains very limited.

In this chapter, we will show that the optical nanoprobe demonstrated in Chapter 3 can guide and confine visible light into intracellular regions selectively. The optical nanoprobe can deliver payloads into the cell with a high spatiotemporal precision, illuminate intracellular compartments and detect optical signals from the subcellular regions with high spatial resolution. This chapter will also discuss the cytotoxicity induced by intracellular insertion and illumination of the optical nanoprobe. Like the endoscope used in medicine that can directly look and examine the interior of the human body, this minimally invasive optical nanoprobe could become a powerful tool for nanoscale payload delivery, imaging, and probing in single living cells.

5.1 **Instrumental Design of the Nanowire-based Single Cell Endoscopy**

Optical nanoscopy breaking the diffraction barrier has been recently introduced to study chemistry, biology, and physics in the intracellular molecular processes[169-171]. Although the capabilities of current optical techniques have now reached the subcellular level, the high-precision optical imaging systems they rely on are not only complex and expensive, but also bulky and immobile, thus limiting the use of such nanoscopes to research laboratories. Introduction of nanophotonic component into simple, low-cost, bench-top optical setups would miniaturize spectroscopic analyses to the nanoscale, making them particularly useful for studying chemical and biological events inside single cells and their substructures. Recent efforts has been made to develop fluorescence sensing techniques based on submicron tapered optical fibers in living biological specimen[172-175], however, due to the relatively large overall sizes (300~500 nm) and conical shapes, they still have a high risk of rapturing the cellular membrane and the illumination volume remains large. Nevertheless, the fiber-optic fluorescence imaging technique still provides unique features feasible for portable handheld optical systems and flexible endoscopes with minimally invasive in-situ monitoring/imaging in the opaque biological objects (e.g. tissue)[176]. Integration of the nanophotonic probes into the fiber-optic imaging system could allow us to manipulate the nanoscale light inside the living cells for the photo-active biological processes[177,178]and bioanalytical techniques[179,180].

It has been demonstrated in our laboratory that free-standing subwavelength dielectric nanowire waveguides can efficiently shuttle ultraviolet and visible light in air and fluidic media[181,182]. The nanowires have several key features that make them promising for applications to control and study intracellular environments. First, their relatively small dimension (100~250 nm) and flexibility would minimize the invasiveness of the nanowires once they are introduced into the cells. Secondly, due to their higher refractive index (n = 2.1~2.2) than that of the conventional optical fiber (n = ~1.5), the nanowires function as efficient subwavelength optical waveguides in high-index physiological liquids and/or living cell environments (n = 1.3~1.5). The waveguiding also enables highly localized excitation and detection at the very tip of the nanowire. Lastly, the oxide surface of nanowires can be readily decorated with a variety of molecules to enable payload delivery and specific sensing inside the cells. Recently, there have been increasing efforts in interfacing nanowire arrays with living cells to modulate physicochemical properties of the cell and deliver biomolecules into the subcellular enviornments[183-185]. Depending on their diameter, length and density, the nanowires were able to be safely placed in the cell interior cross the membrane and did not disturb cell proliferation and differentiation.

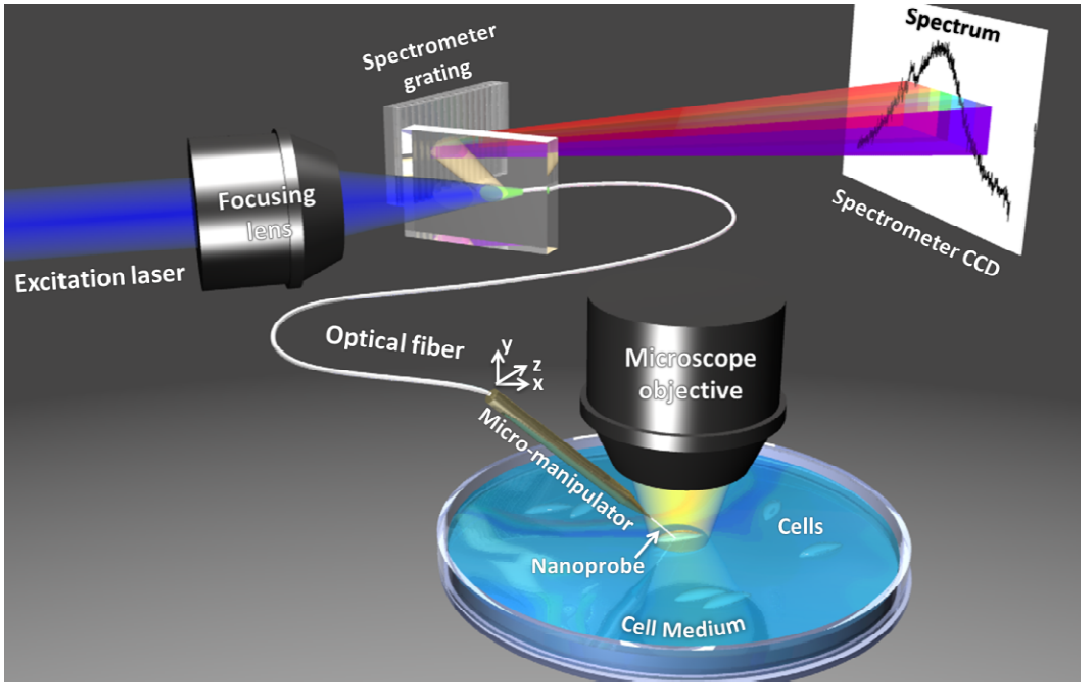

Figure 5.1 Schematic illustration of the nanowire-based cell endoscope system. The nanoprobe, consisting of a nanowire waveguide fixed on the tapered tip of an optical fiber, can be inserted into a single living cell at designated positions through a 3-axis micro-manipulating system for spot delivery of payloads. The nanoprobe can be optically coupled to either an excitation laser to function as a local light source for sub-cellular imaging, or a spectrometer to collect local optical signals.

Combining all the advantages of subwavelength nanowire waveguides and fiber-optic fluorescence imaging, we designed a novel nanowire-based cell endoscope system that allowed us to look and probe inside the single cells and spatiotemporally deliver payloads into the intracellular sites with minimal perturbation of the cellular system.
Figure 5.1 illustrated the proposed construction of the nanowire-based optical probe for single cell endoscopy. The nanoprobe, which is fabricated according to the procedures in Chapter 3, consists of a SnO_2 nanowire waveguide that is mechanically bound and optically coupled to the tapered tip of an optical fiber. The nanoprobe is mounted on a 3-axis micro-manipulating system and can move with minute (0.1 μm) steps in x,y and z directions. The nanowire at the tip of the micromanipulator controlled nanoprobe can be inserted into designated positions of a single living cell in cell culture medium. The other end of the optical fiber is coupled either to an excitation laser focused on the fiber tip for subcellular illumination, or to a spectrometer for local optical signal collection.

5.2 **Cytotoxicity of the Nanowire Probe**

One important motivation of using nanowires as probes for single-cell endoscopy is their minimal invasiveness, as previously demonstrated for Si and GaP nanowire arrays[183-185]. The fine diameters of the nanowires would allow them to penetrate the lipid membrane without damaging cellular functions. In order to study the biocompatibility of our SnO_2 based nanowire optical probes, a series of cytotoxicity tests were first performed at the single-cell level.

HeLa cells were seeded into 35 mm petri-dish with grids and cultured overnight (22,000 cells per dish) at 37^{o}C in the presence of 10% FBS. For all the cytotoxicity tests, single cells were randomly chosen from the grid Petri dish. The positions of each cell tested were documented and dark field images were taken on the cell and its surrounding area for references. The nanoprobes used in the tests were mounted on a 3-axis micromanipulator to ensure precision control over the insertion position.

For the nanoprobe insertion cytotoxicity test, an unmodified nanoprobe was slowly inserted into the cytoplasm for 1 min (Table 5.1, Row 1). For the payload delivery cytotoxicity test, an unmodified nanoprobe was slowly inserted into the cytoplasm, and the insertion region was immediately irradiated with the focused HeCd laser (325 nm, 0.4 mW/cm^2) for 1 min (Table 5.1, Row 3). The nanoprobe was retracted from the cell right after the irradiation. Cytotoxicity of the focused laser irradiation without nanowire insertion was also tested, with the same power density and beam size (Table 5.1, Row 2). For the local illumination cytotoxicity test, an unmodified nanoprobe was slowly inserted into the cytoplasm (Table S1, Row 4) or placed close to the cell membrane (Table 5.1, Row 5), and the tip illumination from the nanoprobe was immediately turned on for the duration of 1 min. The 442nm blue HeCd laser was coupled to the nanoprobe through the optical fiber providing the tip illumination. The input laser power to the optical fiber was 0.4mW and an average output laser power of 10μW was measured from the tip of the nanoprobe. The nanoprobe was immediately removed after the 1 min irradiation. After the procedure, the petri dish was incubated for 10 hrs at 37^{o}C in the presence of 10% FBS

and the cell viability was evaluated using the Calcein live cell assay (Invitrogen). Phase contrast and fluorescent images were taken on the each cell tested for correlation.

Laser wavelength (nm)	Power density of focused laser (mW/cm^2)	Laser input into optical fiber (mW)	Nanowire Insertion Time (min)	Laser Radiation Time (min)	Cell viability
-	-	-	1	-	8/8 (100%)
325	0.4	-	-	1	5/5 (100%)
325	0.4*	-	1	1	10/10 (100%)
442	-	0.4**	1	1	5/5 (100%)
442	-	0.4	0***	1	5/6 (83.3%)

Table 5.1 Nanoprobe and laser cytotoxicity in a single living HeLa cell. All data were acquired with nanoprobe inserted or laser focused on the cytoplasm and the size of the nanowires used in this study are between 150-300nm in diameter.
* For all QD delivery experiments, laser power density of $0.4mW/cm^2$ and radiation time of 1 min were used as a standard operation condition.
** For all local illumination experiments, input laser power of 0.4 mW was used for the optical fiber. An average output laser power of 10 μW was measured from the nanowire end of the optical fiber.
*** In this case, the nanowire probe was placed in close proximity, but not touching, the cell membrane (non-contact mode).

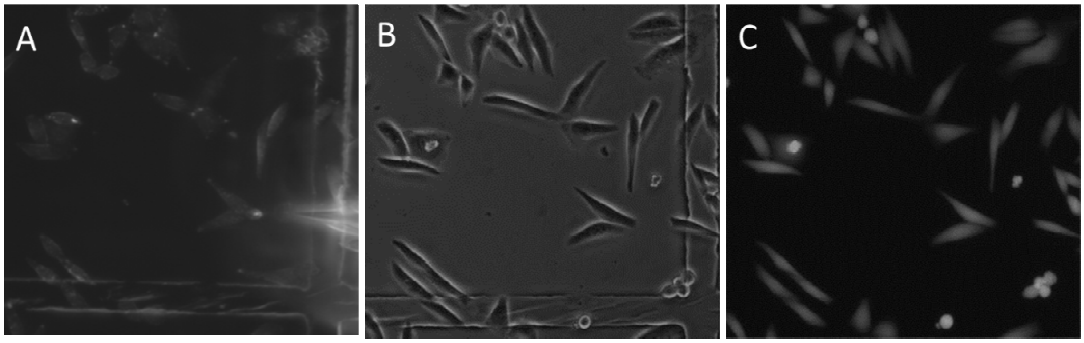

Figure 5.2 Cytotoxicity of the nanoprobe insertion and illumination in a single living HeLa cell. A, Dark-field image of the nanoprobe insertion and illumination. The nanoprobe is introduced into the cytoplasm illuminating the micro-scaled region for 1 min with the waveguided blue light (442 nm). **B and C,** Toxicity of the cell 10 hrs after the nanoprobe insertion and illumination. Phase contrast image of the cell treated with the nanoprobe. (b). Fluorescence image of the cell treated with the nanoprobe after staining with live cell assay dye, Calcein (c).

The experimental results of the cytotoxicity tests were summarized in Table 5.1 and the typical optical and fluorescence images of cells before and after nanoprobe insertion and

illumination were presented in Figure 5.2. Nanoprobe insertion into the cytoplasm and the illumination on the intracellular environment of HeLa cell with the waveguided blue light did not induce any significant cytotoxicity for the experimental conditions required for the subsequent spot cargo delivery and endoscopy studies. The nanoprobe illumination of an average power of 10 μW at 442 nm was proved to be unharmful to the cellular functions due to the small illumination volume (down to picoliter) and short illumination duration (1 min).

5.3 **Spot-delivery of Quantum Dots into a Living Cell with Nanowire Probe**

Having proved the safety of nanoprobe use in single cells, we next investigated the feasibility of delivering payloads into specific intracellular sites with the functionalized nanoprobe. Carbon and boron nitride nanotube-based delivery systems have been reported previously[186,187], where payloads (e.g. QDs) are attached to the nanotube via disulfide bond linkers which are cleavable in the reducing environment of the cytosol. A major limitation for this passive delivery system is the long insertion time (20-30 mins) and the lack of temporal control over the delivery process. Instead, we used photo-cleavable linkers (Figure 5.3A), which can be cleaved by low power UV radiation for a duration that is 20-30 times shorter.

To attach quantum dots on the bare SnO_2 nanowire, the nanowire was first aminated by soaking the nanowires in 2% 3-Aminopropyltriethxysilane (APTES, Sigma-Aldrich) ethanol solution overnight and then rinsing with ethanol several times. The aminated nanoprobe was then immersed in a 0.5 mg/mL PBS solution of photocleavable crosslinker NHS-PC-LC-Biotin (Ambergen) for 1 hr and rinsed with PBS several times. The tip of the biotin-modified nanoprobe was carefully dipped into a droplet (2 μL) of PBS solution of streptavidin-modified QDs (Qdot® 655 streptavidin conjugate, Invitrogen) on a PDMS substrate. In order to confine QDs attachment to the tip of the nanowire, the nanoprobewas controlled by the micromanipulator and the insertion process was monitored under microscope. The tip was immersed in the droplet for ~30 mins before it was rinsed with PBS to remove noncovalently absorbed QDs. Figure 5.3B shows the TEM image of the tip of a SnO_2 nanowire coated with QDs (λ_{em}=655nm) and its photoluminescence (PL) spectrum.

To test the quantum dot conjugated photoactive nanoprobe for precision controlled payload delivery. HeLa cells were seeded into 35 mm petri-dish with grids and cultured overnight (22,000 cells per dish) at 37^{o}C in the presence of 10% FBS. The nanoprobe mounted on the micromanipulator was slowly inserted into the nucleus or cytoplasm. The insertion region was immediately irradiated with the focused 325 nm HeCd laser at 0.4 mW/cm^2 for 1 min, and then the probe was removed from the cell. The fluorescence of QDs translocated into the cell was imaged under 442 nm laser excitation.

Figure 5.3C displays the dark field (DF) and fluorescent images of the QD-conjugated nanoprobe, showing that QDs were selectively coupled to the very tip of the nanowire. The photoactive nanoprobe was able to release QDs into intended intracellular sites (nucleus or cytoplasm) within 1 min (Figure 5.3D and 5.3E) of simultaneous nanowire

insertion and focused UV laser irradiation (325 nm, 0.4 W/cm^2). The photo-activation at this level had no significant effects on cell viability (see Table 5.2).

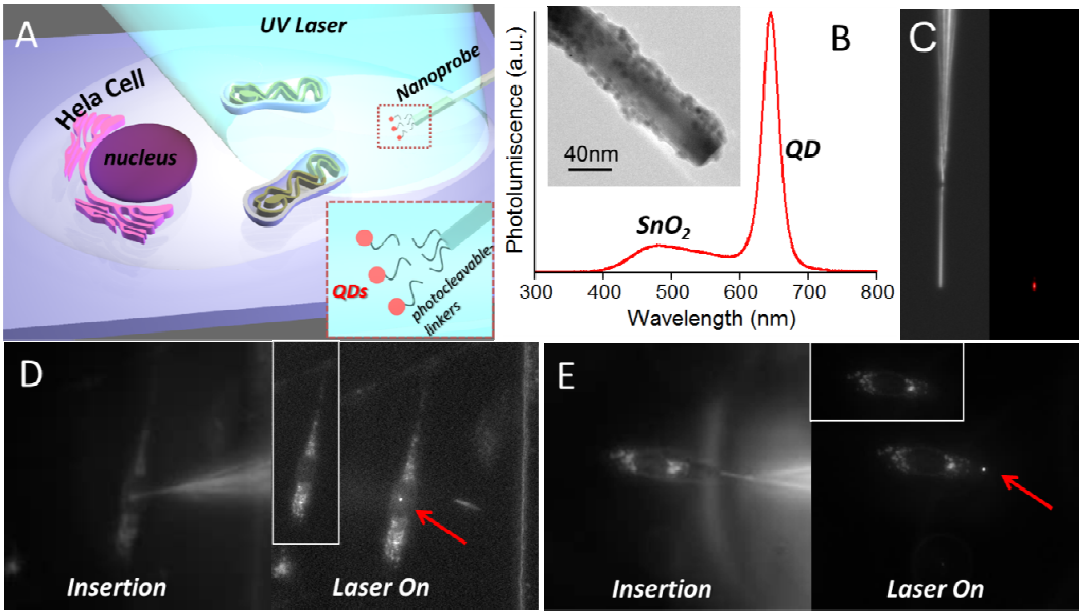

Figure 5.3 Spatiotemporal delivery of quantum dots (QDs) into a single living HeLa cell. A, Schematic of the spatiotemporal delivery of QDs into a living cell using a photoactivable nanoprobe. Inset shows QDs were conjugated to the nanoporbe via photocleavble linkers. **B,** Photoluminescence (PL) spectrum of the QD (em. 655 nm)-conjugated SnO_2 nanoprobe. The nanowire-QD region of nanoprobe was directly excited with the focused HeCd laser (325 nm). Inset shows transmission electron microscope image of the QD-conjugated SnO_2 nanoprobe. **C,** Dark-field (left panel) and fluorescence (right panel) images of the QD-conjugated SnO_2 nanoprobe. **D,** Dark-field image showing the nanoprobe inserted into the cell nucleus (left panel). Dark-field/fluorescence image taken after focused UV irradiation (325nm, 1 min) on the nanoprobe tip, showing the QD fluorescence in the cell nucleus under 442nm laser excitation (right panel). **E,** Dark-field image showing the nanoprobe inserted into the cytoplasm (left panel). Dark-field/fluorescence image taken after focused UV irradiation (325nm, 1 min) on the nanoprobe tip, showing the QD fluorescence in the cell cytoplasm under 442nm laser excitation (right panel). Insets in (D) and (E) are dark-field images of the two cells when the 442nm excitation laser was turned off, respectively.

Control experiments were performed with two types of photo-inactive nanoprobes: QD-conjugated nanoprobe via a disulfide bond linker that can be cleaved in the reducing environment of the cytoplasm, and QD-conjugated nanoprobe with non-cleavable linker that cannot be cleaved chemically or optically.

To fabricate the disulfide linker QD-conjugated nanoprobe, an aminated nanoprobe was first immersed in 0.5 mg/mL PBS solution of sulfosuccinimidyl

6-(3'-[2-pyridyldithio]-propionamido) hexanoate crosslinker (Sulfo-LC-SPDP, Thermo Scientific) for 1 hr and rinsed with PBS. The amine group on the surface of QD (Qdot® 655 ITK™ amino (PEG), Invitrogen) was then converted to sulfhydryl group using 2-Iminothiolane•HCl (Traut's Reagent, Thermo Scientific) and dispersed in PBS. The tip of the Sulfo-LC-SPDP-modified nanoprobe was then dipped into a small droplet (2μL) of the sulfhydryl-modified QDs solution and immersed for 30 min. To ensure the QD attachment only to the tip of the nanoprobe, the position of the nanoprobe was controlled by the micromanipulator and monitored under microscope. The derived QD-conjugated nanoprobe was then rinsed with PBS to remove noncovalently attached QDs.

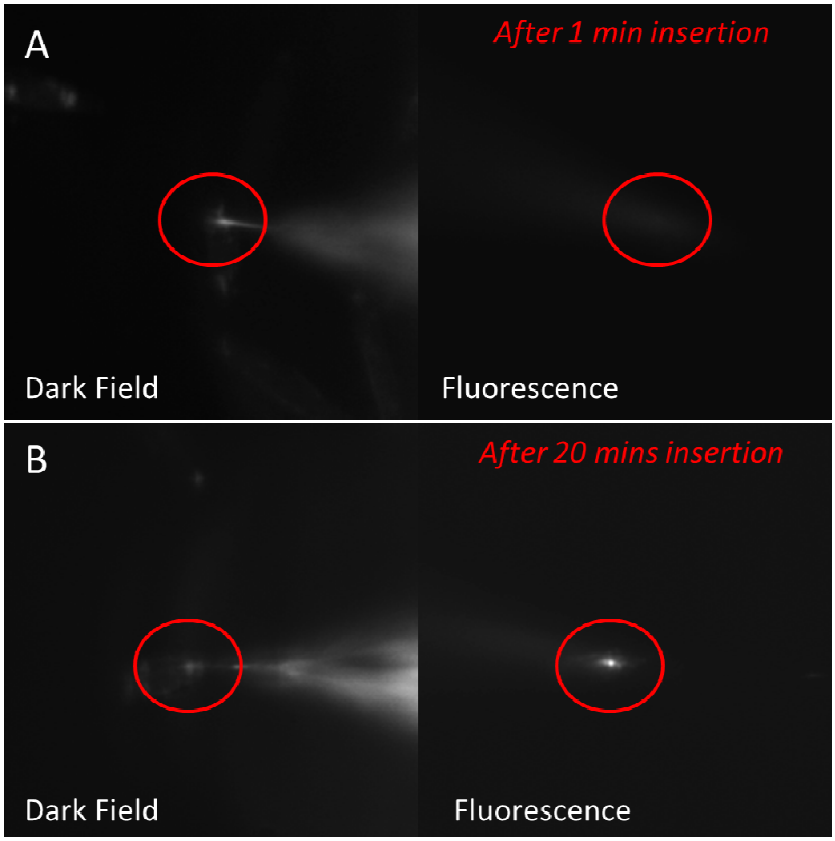

Figure 5.4 Passive delivery of quantum dots (QDs) into a single living HeLa cell with disulfide bond (S-S) linkers. A. Dark-field image showing the nanoprobe coated with QDs via S-S linker inserted into the cytosol of a living HeLa cell (left panel). Fluorescence image of the cell after probe insertion for duration of 1 min showing no QD signal (right panel). **B.** Dark-field image showing the nanoprobe coated with QDs through S-S bond linker inserted into the cytosol of a living HeLa cell (left panel). Fluorescence image of the cell after probe insertion for a duration of 20 mins showing an oval shaped QD fluorescence signal as indicated by the red arrow (right panel). Note that this passive delivery method requires relatively long insertion time (20 min) and causes the non-specific release of QDs (from all parts of the probe immersed in cytosol).

The passive delivery experiment was then conducted by slowly inserting the disulfide linker QD conjugated nanoprobes into the nucleus or cytoplasm with the micromanipulator for duration of 1 min and 20 mins and then retracted from the cell. Figure 5.4 shows the dark-field images of QD conjugated disulfide linker nanoprobes during their insertion into the cytoplasm of two individual living cells, and the fluorescence image of the cell after 1 min (Figure 5.4A) and 20 mins (Figure 5.4A) insertion, respectively. QD fluorescence was observed for 20 mins insertion, whereas for 1 min insertion, which is the time duration required for releasing QD for photoactive linker, no QD fluorescence was detected. The dissociation of the disulfide linker in cytoplasm is a much slow process than the cleavage of the photocleavable linkers by low-intensity UV radiation.

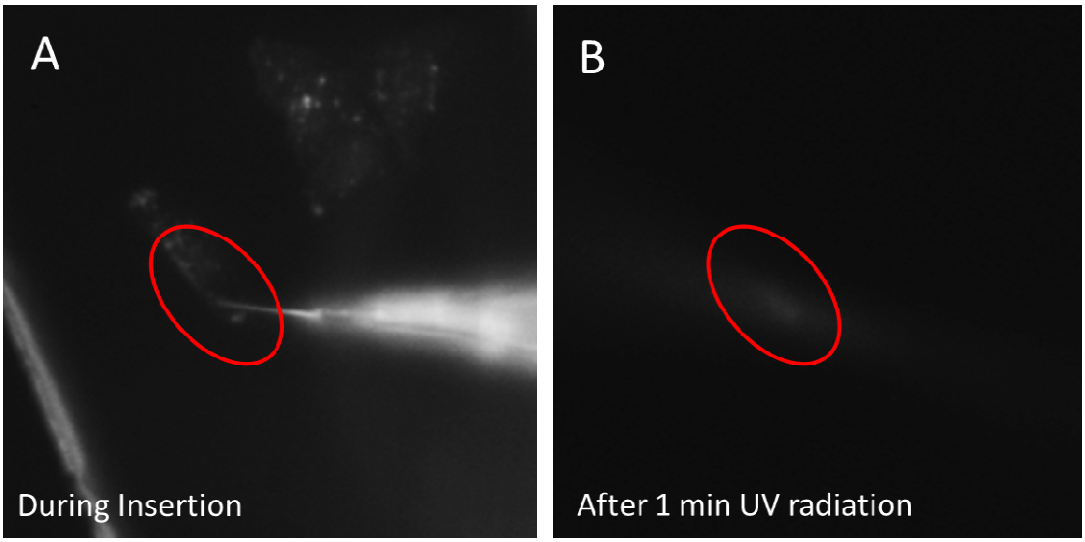

Figure 5.5 Quantum dot delivery into a HeLa cell with QD-conjugated nanoprobe via photo-inactive linkers. A, Dark-field image showing the non-photocleavable linker QD-conjugated nanoprobe inserted into the cell. **B,** Fluorescence image of the cell after UV radiation for 1 min, showing no QDs was present in the cell after the attempt. A 442nm focused and a 532nm long-pass filter was used for the QD fluorescence imaging.

To fabricate the non-cleavable linker QD-conjugated nanoprobe, the aminated nanoprobe was reacted in 0.5 mg/mL PBS solution of Sulfo-NHS-LC-Biotin (Thermo Scientific) for 1 hr and rinsed with PBS several times. The tip of the biotin-modified nanoprobe was then dipped into a small droplet (2μL) of the streptavidin-modified QDs (Qdot® 655 streptavidin conjugate, Invitrogen) solution and immersed for 30 min. To ensure the QD attachment only to the tip of the nanoprobe, the position of the nanoprobe was controlled by the micromanipulator and monitored under microscope. The derived QD-conjugated nanoprobe was then rinsed with PBS to remove noncovalently attached QDs. The control experiment with the non-cleavable linker QD-conjugated nanoprobes was performed according to the same procedure of the disulfide linker nanoprobe for the duration of 1 min.

Figure 5.5 and 5.6 show that 1 min-insertion of photo-inactive nanoprobe (conjugated via non-cleavable linkers) and 3 min-insertion of photo-active nanoprobe without UV irradiation and with UV irradiation did not result in QD release, demonstrating that the QD delivery was specific to the photo-activation. The QD delivery set up could be further integrated by fabricating the nanoprobe with a UV transparent optical fiber, so that the required UV excitation can be coupled directly through the nanoprobe, enabling QD release through the nanowire tip emission.

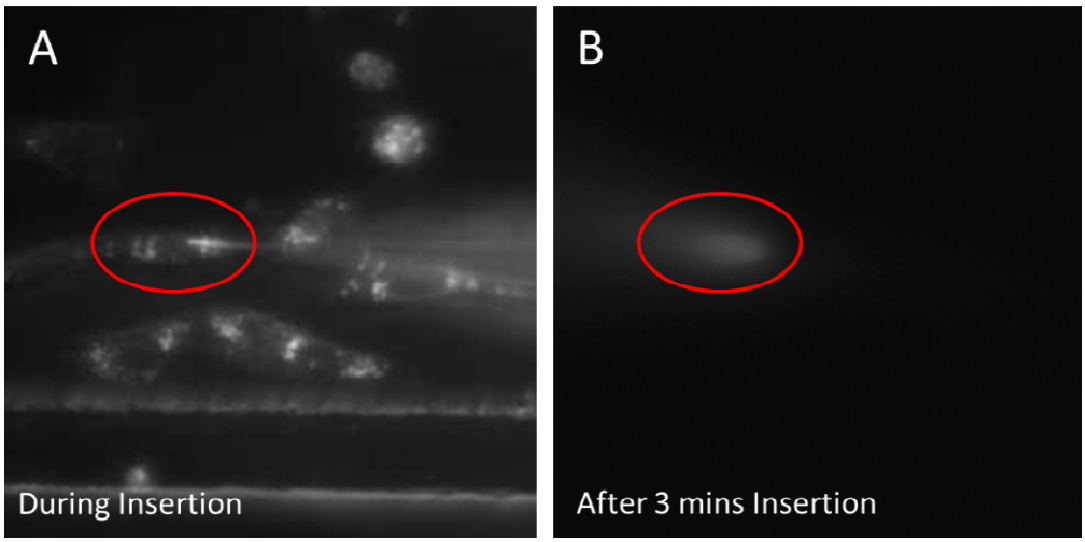

Figure 5.6 Quantum dot (QD) delivery into a single living HeLa cell without irradiation. A, Dark-field image showing the photoactive QD-conjugated nanoprobe inserted into the cell. **B,** Dark-field image along with the excitation by the focused blue laser showing that no QDs were delivered into the cell after the insertion for 3 min without irradiation (photoactivation). A 532nm long-pass filter was used for the QD fluorescence imaging.

5.4 High Resolution Sub-cellular Illumination with Nanowire Probe

We next explored the feasibility of high resolution subcellular imaging and tracking of fluorescent species with waveguided nanoprobe illumination (Figure 5.7A).

For subcellular QD imaging, two clusters of QDs were delivered side by side with ~2 μm separation in the cytoplasm of a living HeLa cell with a photo-active QD conjugated nanoprobe described in Figure 5.3. An unmodified nanoprobe was placed close to the two QD clusters without direct contact with the cell membrane. The nanoprobe was mounted on the micromanipulator to offer precision control over the nanoprobe position. The distal end of the optical fiber was coupled to 442nm blue HeCd laser with an input power of 0.4mW through a single mode fiber coupler. The highly directional laser beam from the nanoprobe, which is coupled to a 442 nm blue laser, can selectively excite the fluorescence of only one of the two QD clusters while leaving the other one dark (Figure 5.7B and C). This nano-flashlight can work in either “contact” mode when the nanowire

is inserted into the cell, or the non-invasive "non-contact" mode, leaving the cell completely intact.

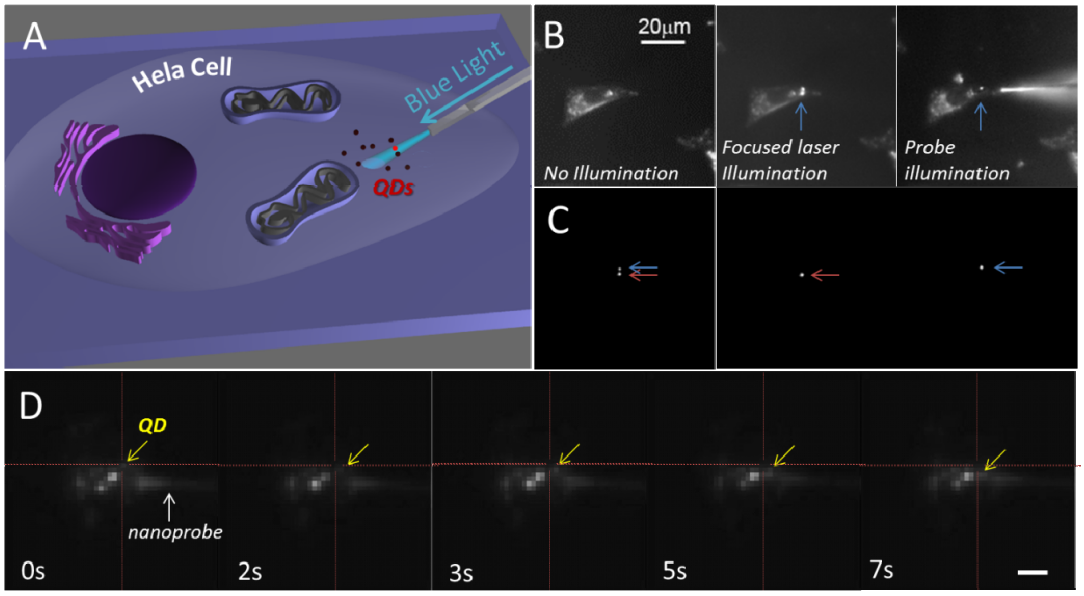

Figure 5.7 Subcellular imaging and tracking of quantum dots (QDs) in a single living HeLa cell. A, Schematic of the subcellular imaging and tracking of QDs in a living cell using a nanoprobe. **B and C,** Dark-field images along with QD fluorescence (B) showing the imaging of two distinct clusters of QDs by the nanoprobe illumination (442 nm HeCd laser waveguided through the probe). Each cluster of QDs was delivered into the cell using the photoactivable nanoprobe as described in figure 3. Two clusters of QDs were adjacently located each other (~2 μm) and highly localized illumination by the nanoprobe was able to separately image each cluster of QDs. Fluorescence images (**C**) of QDs showing the spatial resolution of the local illumination by the nanoprobe. **D,** Fluorescence images showing the tracking of QD movement in the subcellular region during the time period of 0-7 s using the nanoprobe illumination. Yellow arrows mark the current position of the QD in each image and the crosses of the dotted lines mark the initial position of the QD at t=0s. Cells were pre-treated with the aminated QDs for 1 hr before the nanoprobe illumination. A 532 nm long-pass filter was used to screen the excitation laser for the fluorescent imaging. Scale bar is 5 μm.

For subcellular QD tracking, cells were pre-treated with the aminated QDs for 1 hr and rinsed several times with PBS. The nanoprobe was placed close to the cytoplasm where multiple clusters of QDs were loaded. The movement of the QDs (clusters) in the subcellular region was locally monitored over time with the nanoprobe illumination. The nanoprobe illumination allowed tracking the movement of one of the QD clusters (yellow arrow) in the subcellular region (~ 10 μm^2) (Figure 5.7D). The light confined and waveguided on the nanoprobe could be further used to sense change of molecular kinetics in the intracellular substructures (e.g. mitochondria).

5.5 Local Optical Signal Collection with Nanowire Probe

An inverse process of waveguided illumination from the tip of the nanowire probe, the collection of fluorescent signal from subcellular region through the nanoprobe was also demonstrated.

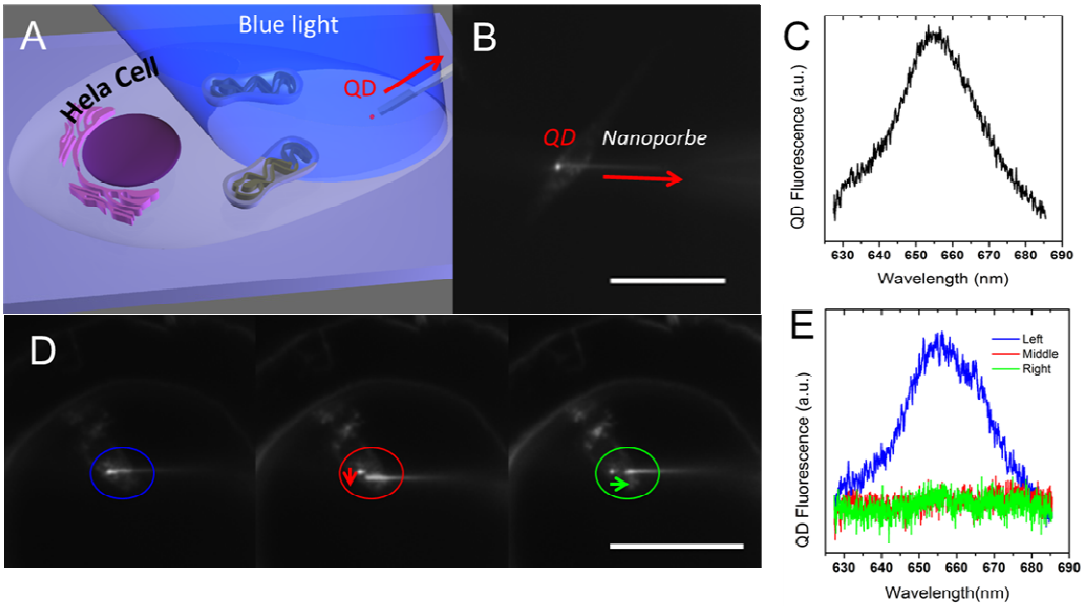

Figure 5.8 Near-field collection of quantum dot (QD) fluorescence in a single living HeLa cell. A, Schematic of the QD fluorescence local detection in a living cell using a nanoprobe. The nanoprobe is placed near the QD (λ_{em}=655nm) that is pre-loaded in the cytoplasm and excited by a blue laser beam. The QD fluorescence was locally collected through the nanowire probe which was coupled to a spectrometer. **B,** Dark-field/fluorescence image of a nanoprobe placed close to a QD cluster in the cytoplasm that was excited by a focused 442nm laser. **C,** Spectrum of the QD fluorescence collected through the nanoprobe, showing a single peak centered at ~655nm. **D,** Dark-field/fluorescence images of a nanoprobe in close contact with a QD cluster in a HeLa cell (left panel), separated vertically by 2μm (middle panel) and horizontally by 6μm from the QD (right panel). The colored circles mark the position of the QD cluster and the tip of the nanoprobe. The colored arrows in the middle and right panels indicate the nanoprobe movement with respect to its position in the left panel. **E,** Spectra of QD fluorescence collected through the nanoprobe corresponding to the 3 images in D respectively. The QD signal faded out fast as the probe was moved from the QD. A 532 nm long-pass filter was used to screen the excitation laser for the fluorescent imaging. Scale Bars=50 μm.

The cells were pre-treated with the aminated QDs for 1 hr and rinsed several times with PBS. QD fluorescence was excited by focused 442 nm blue laser. The nanoprobe was placed close to the QDs in the cytoplasm to pick up local fluorescent signal. The distal end of the optical fiber was connected to a UV-Vis spectrometer and the gratings were

calibrated with 442nm and 650nm laser lines. The location of the nanoprobe was precisely controlled using the micromanipulator during the experiment.

As illustrated in Figure 4A and B, a single QD cluster pre-loaded in the cytoplasm of a living HeLa cell was excited with a focused laser beam, and the tip of a nanowire probe was placed adjacent to the cluster to extract the QD fluorescence, which is back-coupled to the fiber optics. The distal end of the fiber optics was connected to a spectrometer to record the wavelength resolved fluorescence (Figure 4C). The signal collection with the nanoprobe was very sensitive to the distance between the QD cluster and the nanowire tip (see Figure 4 D and E), opening up the possibility for high spatial resolution fluorescence mapping. The tapered tip of the optical fiber did not contribute to signal detection, because the QD fluorescence cannot be extracted through the fiber tip when it was beyond 25 μm from the target QD (Figure 5.9), whereas for our typical nanoprobes, the protruding lengths of the nanowire from fiber tip are at least 50 μm. This local detection technique could make it possible for examining the interior of, non-transparent in particular, living biological objects minimal-invasively, which would be impossible for bulky near-field scanning optical microscope (NSOM) tips.

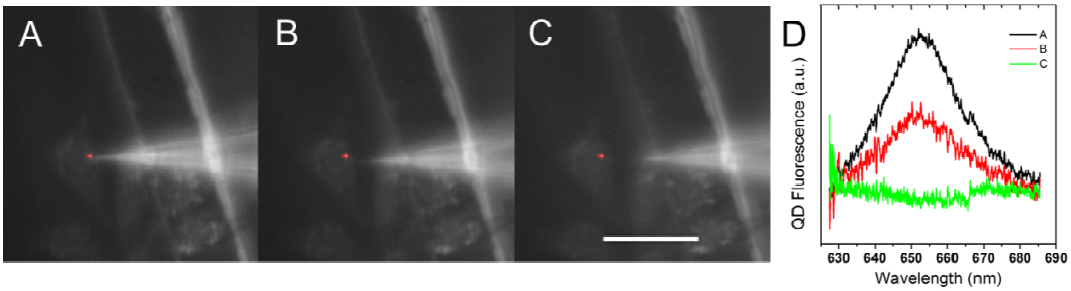

Figure 5.9 Quantum dot fluorescence collection through a tapered optical fiber tip. A, Dark-field image superimposed with the QD fluorescence image of QD-loaded live HeLa cells. A tapered optical fiber (3º taper angle) is placed close to QDs in the cytoplasm. **B-C,** Dark-field/fluorescence image showing the optical fiber retracted by ~ 12 and ~22 μm from the QD. **D,** Spectra of QD fluorescence collected from the tip of optical fiber for A (black curve), B (red curve) and C (green curve), respectively. Signal died out as the fiber is beyond 22 μm in separation with the QD. Scale bar is 50 μm.

5.6 **Conclusions**

We have developed a versatile and biocompatible nanowire-based optical probe for intracellular cargo delivery with high spatiotemporal precision, endoscopy with high spatial and temporal resolution. These nanoprobes are highly flexible and robust, both mechanically and optically, and can endure repeated bending and deformation during cell imaging process. The effective optical coupling between the fiber optics and the nanowire enables highly localized excitation and detection, limiting the probe volume to the close proximity of the nanowire (i.e., down to pico- and femtoliter), making it a promising candidate for high resolution optical imaging, mapping and chemical/biological sensing along with the precision delivery of gene, proteins, and drugs. None the less, this versatile nanotechnique does not rely on any expensive or bulky instrumentation. It only requires micromanipulator and optical microscope that are readily available in most biological labs. Moreover, different functions can be further integrated to make the whole nanoprobe system even more compact. For example, by combining the optical excitation and signal out-couple into the same optical fiber, simultaneous illumination and signal collection could be realized.

Chapter 6
Nanofluidic Diodes based on Nanotube Heterojunctions

Semiconductor diodes and field effect transistors have laid the foundation for modern electronic and optoelectronic industry. The mechanism of tuning charge transport in electronic devices has recently been implemented into the nanofluidic field for the active control of ionic transport in confined geometry[188,189,190,191]. Artificial nanopores and nanofluidic devices have been fabricated for single molecule sensing and configuration study[192,193,194,195,196,197]. These artificial nanochannel/pore devices often passively transport ionic species under electric field, similar to simple electron transport in a *resistor*. Introducing external electrical field to modulate ionic conductivity in nanoscale channels has resulted in p- and n-channel nanofluidic *transistor*s which exhibit rapid modulation of ionic conductance[198,199,200]. It was also being proposed that "pn-junction diode" type nanochannels could function as nanofluidic *diode*s and bipolar transistor diodes[201]. Realization of such nanofluidic diode devices should represent a significant step towards building ionic equivalents of electron devices and integrate circuit. They would also lead to novel ion separation and energy conversion technologies, due to their unique ion transport properties[202,203,204]. Although this concept has recently been demonstrated in molecular junctions[205,206], geometrically or chemically asymmetric channels through diffusion limited patterning[207,208,209], solid state nanofluidic diodes based on intrinsic *pn* ionic junctions, which is geometrically uniform, chemically robust, and compatible with existing lab-on-a-chip technology, have not been demonstrated due to difficulty in designing and fabricating nanotube heterojunctions with opposite surface charge type.

In this chapter, we will discuss the synthesis of longitudinal heterostructured SiO_2/Al_2O_3 nanotubes. The ionic transport through these nanotube heterojunctions exhibits clear current rectification, a signature of ionic diode behavior.

6.1 **Design of Solid State Nanofluidic Diode**

Nanofluidics is attracting increasing attention recently as the dimensions for chemical and biological analytical techniques are being scaled down in order to achieve ultrasensitive or even single molecule level detection. For nanofluidic channels with dimensions smaller than the characteristic length scale for ion screening known as Debye length (λ_D), overlapping of electric double layers of charged channel walls results in a unipolar solution of counter-ions[210,211]. The Debye length, $\lambda_D \propto I^{-1/2}$, I being the total ionic strength, usually ranges between 1 and 100 nm in aqueous solution. In a unipolar

environment, the average concentration of the counter-ions in a nanotube with radius r is then dictated by electro-neutrality, and depends on the surface charge density σ of the channel wall: $C=2|\sigma|/rF$. The polarity of the counter-ions depends on the type of surface charge on the channel. Negative surface charges would yield cation majority carriers in the channel, and vice versa. For example, we have previously demonstrated that surface functionalization within silica nanotubes can switch the nanofluidic transistors from *p-type* field effect nanofluidic transistors, to *n-type* field effect transistors[12].

A nanotube hetetojunction with opposite surface charges on two segments of the channel walls should in principle function as an ionic diode to rectify the ion current. The concept of an ionic analog of semiconductor p-n junction originates in "bipolar membranes" [212-214] by interfacing oppositely charged ion-exchange membranes into physical contact. Introducing such "pn-junction" type nanochannels in fluidic systems has led to the proposal of nanofluidic diodes and bipolar junction transistors (BJTs)[201]. The diode behavior has recently been observed in chemically or geometrically asymmetric channels[207,208]. These early demonstrations have been made possible through surface functionalization of the selected segments within the same single nanochannel. No nanofluidic diodes, however, have been demonstrated so far based on intrinsic *pn*-junction ionic channel.

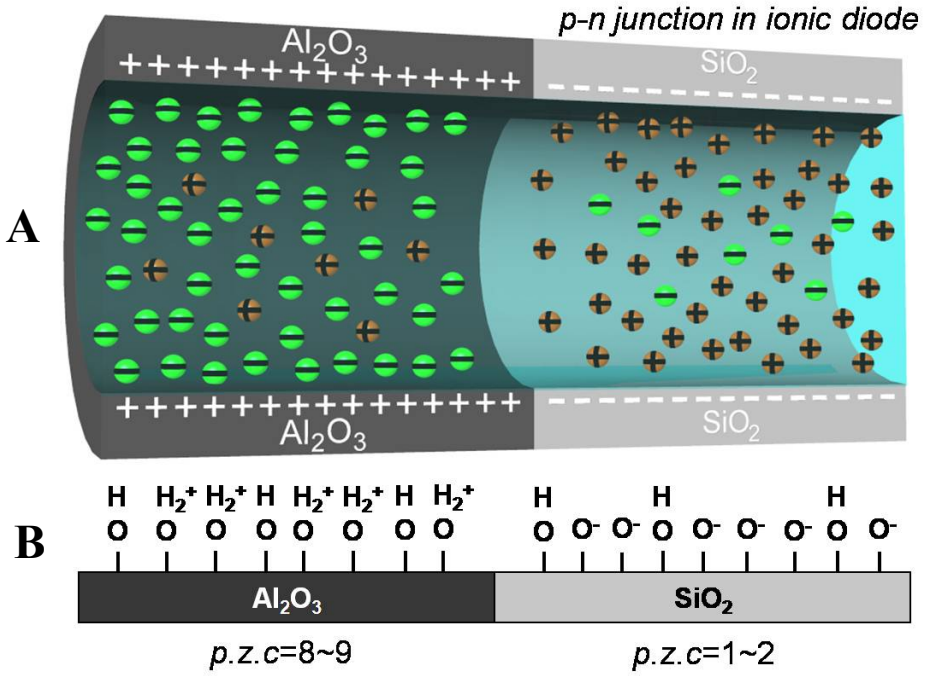

Figure 6.1 Schematics of a nanotube heterojunction. **A,** Schematic illustration of ion distribution in a nano-ionic diode consisting of longitudinally heterostructured oxide nanotube. **B,** Inner surface structure of a nanofluidic diode. It shows the origin of the opposite surface charges on the inner surface of the tube at neutral or mild acidic pH values.

It has been demonstrated previously that SiO_2 nanotubes serve as the *p-type* ionic channel in which the majority charge carriers are cations in unipolar region[199,200]. This is based on the surface chemistry of the metal oxide surface in contact with an aqueous solution and is determined by the dissociation of the hydroxyl groups. The general equilibrium can be expressed as: $M\text{-}OH_2^+ \rightarrow M\text{-}OH + H^+ \rightarrow M\text{-}O^- + 2H^+$, which shifts to the right as pH increases. For each oxide surface, there exists a pH value known as point of zero charge (*p.z.c.*), where the surface hydroxyl groups are undissociated and the surface has zero net charge. This *p.z.c.* value depends on the electronic nature of the metal-oxygen bond and the stoichiometry of the surface. SiO_2 surface has a *p.z.c.* of 1-2[215], so the surface carries net negative surface charge at neutral pH. Al_2O_3, on the other hand, has a *p.z.c.* of 8-9[215], which means at $pH=7$ the surface chemistry is dominant by $Al\text{-}OH + H^+ \rightarrow Al\text{-}OH_2^+$, and the surface carries net positive surface charge. Hence an Al_2O_3 nanotube will behave as an n-type nanofluidic channel, which allows the transport of anionic majority species under unipolar condition. A longitudinal heterojunctioned nanotube, with half of tube being SiO_2 and the other half Al_2O_3, if can be made, should function as *pn* ionic diode and exhibit ionic current rectification (Figure 6.1).

6.2 Heterojunction Nanotube Synthesis

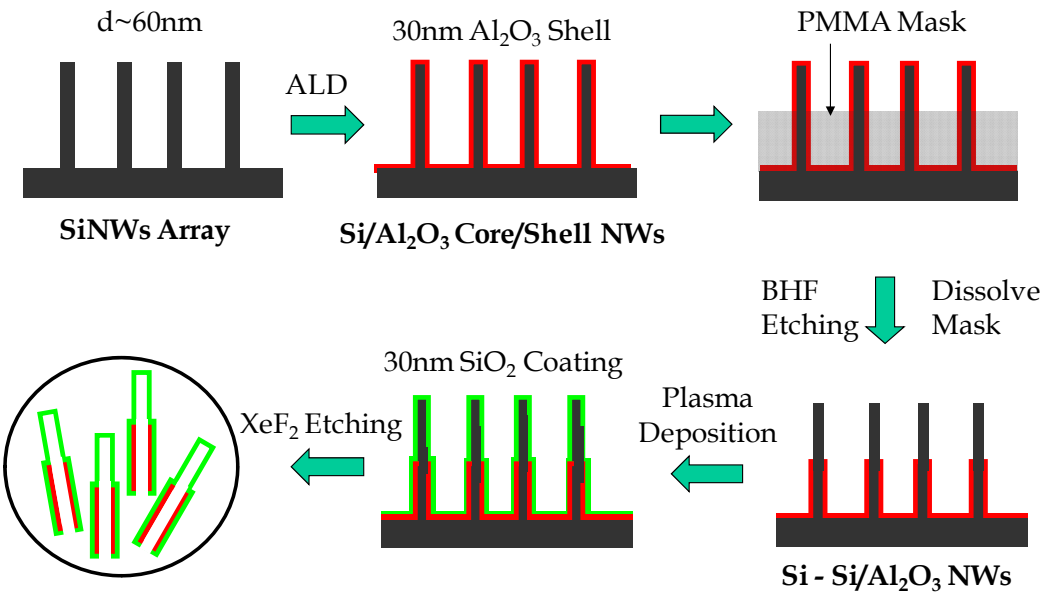

Figure 6.2 Process flow for the fabrication of SiO_2-Al_2O_3 diode nanotube array

We have designed and successfully synthesized the proposed Al_2O_3/SiO_2 heterojunction nanotube as the target building block for nanofluidic p-n diodes. A synthetic strategy towards Al_2O_3/SiO_2 heterojunction nanotubes was developed, using silicon nanowires as templates and a simple fabrication process to integrate single nanotube fluidic channel into nanofluidic diode device. The synthetic procedure of heterostructured Al_2O_3/SiO_2 nanotubes is schematically illustrated in Figure 6.2. Using vertical silicon nanowire arrays as templates[216], heterojunctions SiO_2/Al_2O_3 nanotubes arrays can be made through

multiple steps of conformal atomic layer deposition (ALD), protection/de-protection and selective etching.

Silicon nanowire arrays were prepared using chemical vapor deposition (CVD) epitaxial growth using silicon tetrachloride ($SiCl_4$, Aldrich, 99.99%) as the silicon source. Hydrogen (10% balanced by argon) is used to reduce $SiCl_4$ at high temperature (810-850˚C). Gold Nanoparticles (Ted Pella, Inc, 50nm) was deposited on Si (111) substrates to initiate the growth of epitaxial silicon nanowire array via the vapor-liquid-solid (VLS) growth mechanism. The vertical silicon nanowire array was first coated with Al_2O_3 by Atomic Layer Deposition (ALD) at 200˚C in a flow reactor. ALD is a film deposition technique that produces highly conformal, uniform and controlled thin films. Precursor gases for the Al_2O_3 deposition, $Al(CH_3)$ (trimethylaliuminum [TMA]) and H_2O are alternately pulsed into the reactor and then purged away, resulting in a self-limiting growth process that constructs a film one monolayer at a time. The growth rate at 200˚C in the ALD reactor used is calibrated to be 1.2Å/cycle, so 250 cycles are deposited to yield a 30nm Al_2O_3 film on the SiNWs.

PMMA (polymethyl methacrylate, M.W. 35k, 5% in Ethanol) solution was then drop-casted on the SiNW array as a mask to protect the bottom half of SiNWs from subsequent etching. The thickness of the PMMA mask was controlled by oxygen plasma etching till 2/5 of the total lengths of the SiNWs are exposed. The substrate was then etched in 1:5 Buffered Hydrofluoric Acid (BHF) bath to remove the Al_2O_3 coating on the exposed part of the array. The etching process was monitored with SEM to make sure of the complete removal of the oxide layer on the top half of the SiNWs. After etching, the PMMA mask was removed with CH_2Cl_2 and the substrate was then re-coated with SiO_2 by RF Plasma Sputtering. Finally, the core-shell nanowires were broke off from the substrate and transferred to a fused silica substrate/or a TEM grid. The substrate with the core-shell nanowires were then loaded into a Xetch® Xenon Difluoride Etching System to etch away the Si cores and release Al_2O_3/SiO_2 di-block nanotubes. XeF_2 etching is an all gas phase, room-temperature, isotropic silicon etching process that has very high selectivity to many oxides thin films including SiO_2 and Al_2O_3 (~2000:1). It thoroughly removed the Si nanowire template while leaving the oxide coating intact and the inner surface of the resultant nanotubes smooth.

Figure 6.3A shows the scanning electron microscope (SEM) image of vertical $Si\text{-}SiO_2/Al_2O_3$ nanowire array on a Si 111 substrate. The bottom halves of the Si nanowires are conformally coated with Al_2O_3 by atomic layer deposition, while the top halves are pure Si nanowire whose original Al_2O_3 coating has been selectively removed by wet etching. A sharp diameter modulation is clearly visible at the junction. The transmission electron microscope (TEM) image (Figure 6.3B) of the final heterojunction oxide nanotubes after removal of the Si core also shows a distinct wall thickness contrast at the junction. The thinner part of the tube consists of pure SiO_2, whereas the thicker part is a coaxial core-shell structure of Al_2O_3/SiO_2 wall with Al_2O_3 being the inner wall. The nanotubes, though have a sharp modulation in the wall thickness at the Al_2O_3/SiO_2 junction, form a smooth and homogeneous inner surface throughout the lengths of the

nanotubes, as can be seen in the close-up scanning TEM image in Figure 6.3C (left). EDAX elemental mapping (Figure 2c, right panel) gives explicitly the distributions of Al, Si and O elements over this junction. The dashed line outlined the shape of the heterojunction. It can be seen that Al atoms (top graph, Figure 6.3C, right panel) only exist at the upper section of the junction and only on the inner layer (~30 nm) of the nanotube wall. There is no Al signal from either the outer layer or the whole lower section of the junction. Si signals (middle, Figure 6.3C, right panel) appear on both sections. For the upper half, Si only reside in the ~50 nm thick outer layer, closely wrapping around the Al-abundant shell. For the lower half of the junction, the tube wall is

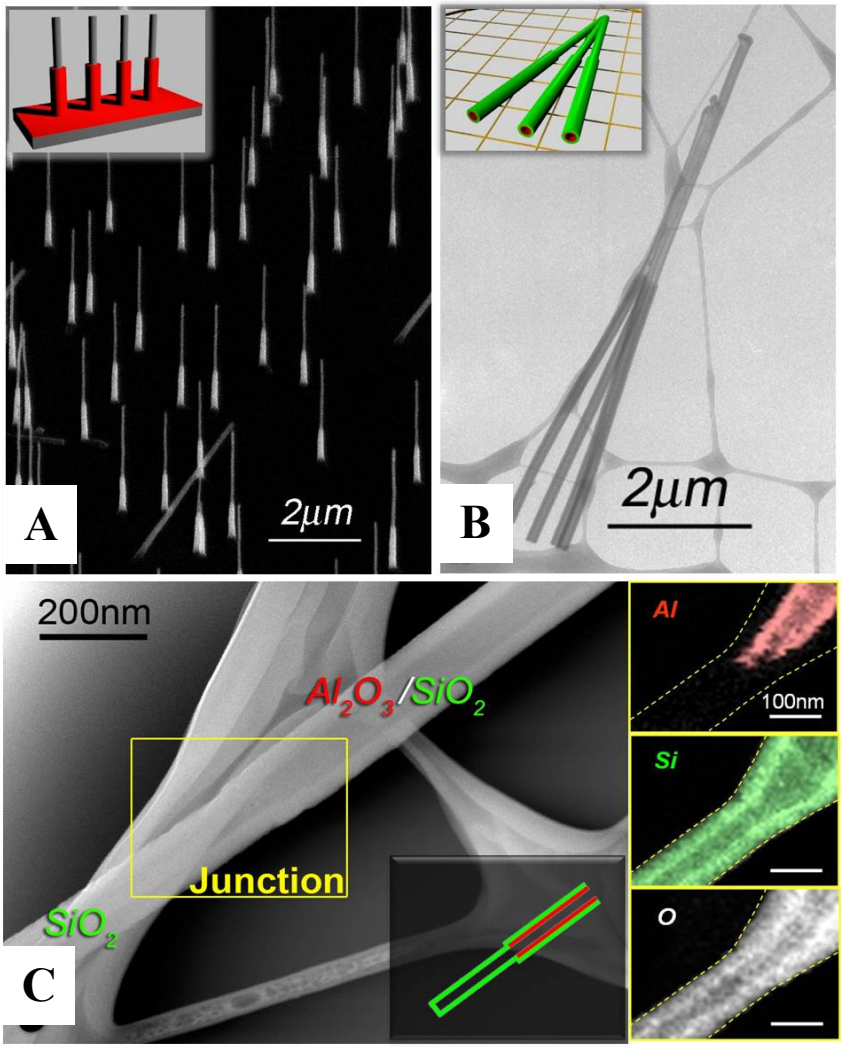

Figure 6.3 of the heterojunction nanotubes. **A,** SEM image of Si-Si/Al_2O_3 nanowire array on Si 111 substrate (Inset: cartoon of the nanowire array). **B,** Representative TEM image of diode nanotubes (Inset: cartoon of the diode nanotubes on a TEM grid). **C,** STEM picture of a single SiO_2/Al_2O_3 junction on a heterostructure nanotube and the elemental mapping of Al, Si and O on the junction (right panels) (Inset: cartoon of the cross section of a heterojunction nanotube).

composed exclusively of Si and O. This mapping result shows unambiguously that the inner surfaces of the as-made nanotubes are indeed half Al_2O_3-half SiO_2 with distinct heterojunctions formation as designed.

6.3 Charge Distribution

The inherent charge discontinuity for the inner surface of the as-made heterojunction nanotubes was first confirmed by fluorescent mapping with ionic dyes selectively absorbed inside the nanotubes. To visualize the surface charge polarity in the Al_2O_3/SiO_2 heterojunction nanotubes, we introduced two fluorescent dyes that carry opposite charges in neutral pH: Fluorescein and Rhodamine 6G (R6G). Fluorescein and Rhodamine 6G are both laser dyes with high quantum yield and high photostability in aqueous solution. Fluorescein is a week carboxyl acid with $pK_a=3.31$[149]. At neutral pH, it carries a negative charge which can bind selectively to the positively charged Al_2O_3 surface through electrostatic interaction. On the contrary, Rhodamine 6G (R6G) has an amino group that is protonated at neutral pH, and bears a positive charge that can be absorbed selectively onto the negatively charged SiO_2 surface. Should there be a switch in surface charge polarity in the Al_2O_3/SiO_2 heterojunction nanotubes, the two types of charged dye molecules in a low ionic strength environment would selectively diffuse into and reside in the segment of the nanotubes with opposite surface charges. Consequently, the surface charge on the Al_2O_3 and SiO_2 segments of the nanotubes could be distinguished optically by the distinct fluorescent emissions of the two dyes.

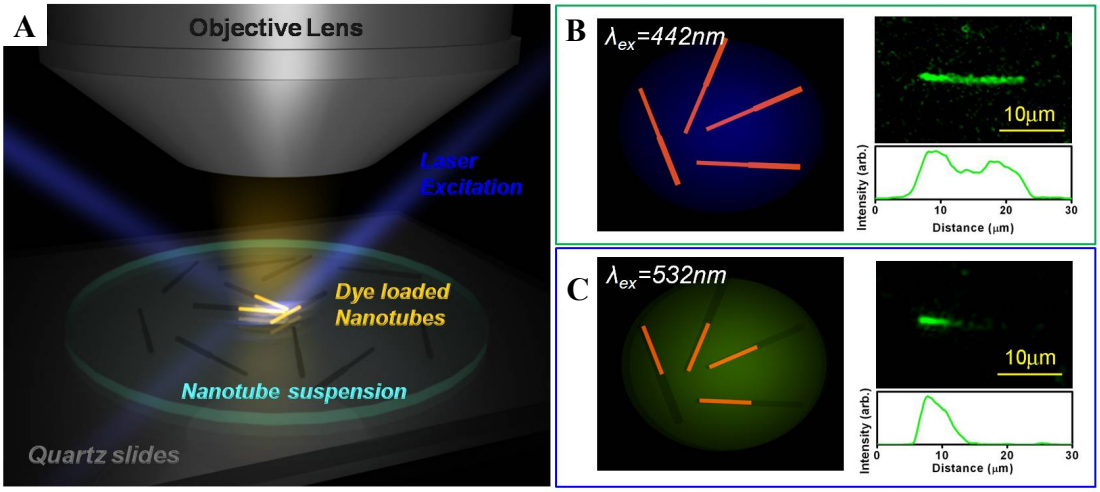

Figure 6.4 Optical imaging of ion distribution in heterojunction nanotubes. **A,** Schemetic of the fluorescence measurement setup. **B** and **C,** Fluorescent micrographs and intensity profiles of a single diode nanotube loaded with fluorescent dye molecules with opposite net charges (R6G with net positive charges and fluorescin with net negative charges) under 442nm laser excitation (**B**) and 532nm laser excitation (**C**) respectively.

The feasibility of probing surface charge polarity with charged dye molecules was first demonstrated with pure SiO_2 and Al_2O_3 nanotubes. The dye loading procedure is so designed to ensure a unipolar environment within the nanotubes: 10 μL of 10 mM dye solution was dropcasted on pure SiO_2 or Al_2O_3 nanotubes supported on a fused silica substrate. Under this ionic strength, the Debye screening length at the metal oxide surface was about 3nm, and surface charges were completely shielded by counter-ions once diffusion equilibrium is reached, so that the concentration of dye ions in the nanotube was dictated by bulk concentration. The nanotubes were then washed 3 times in 20 ml deionized water bath for 5 mins each time to reduce the bulk dye concentration and the ionic strength, so that the system moves into a unipolar condition. After this step, the fluorescent background from the bulk solution was suppressed/eliminated; and the counter-ion concentration inside nanotubes became governed by the surface charge density of the nanotubes and co-ions are expelled from the nanotubes. The wet quartz substrate with dye loaded nanotubes was then capped with a quartz coverslip for imaging.

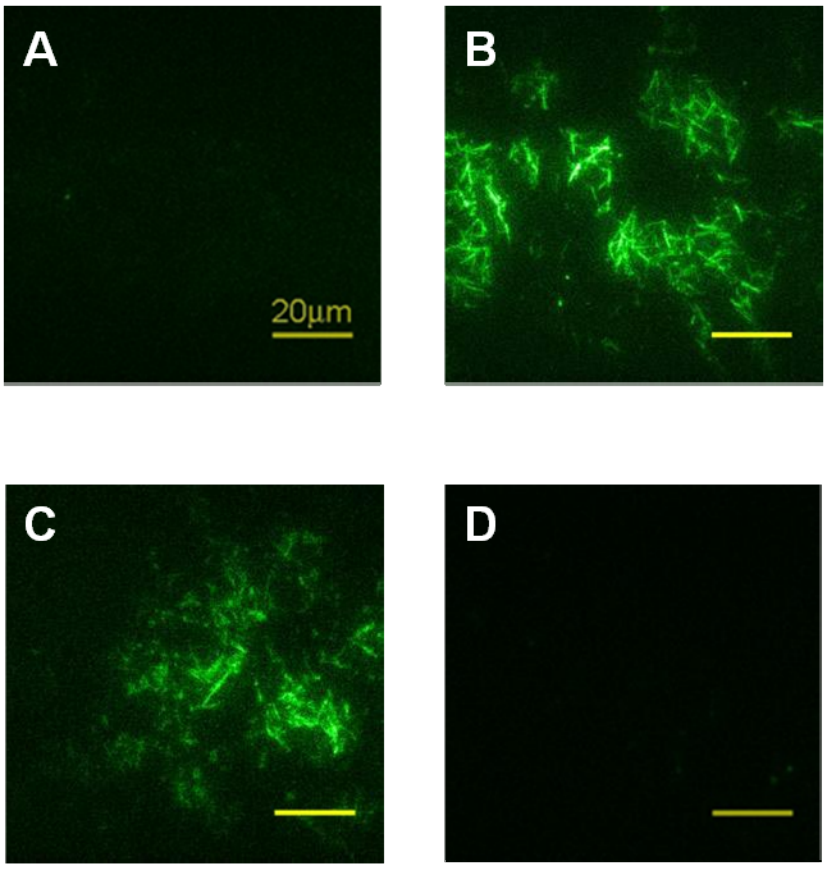

Figure 6.5 Fluorescent micrographs of dye-loaded pure SiO_2 and Al_2O_3 nanotubes under 442nm laser excitation. **A,** Pure SiO_2 tube loaded with Fluorescein. **B,** Pure SiO_2 tube loaded with R6G. **C,** Pure Al_2O_3 tube loaded with Fluorescein. **D,** Pure Al_2O_3 tube loaded with R6G.

The fluorescence measurement setup is shown in Figure 6.4A: The excitation laser was brought in from the side and focused on the nanotubes. The fluorescent signals from the absorbed dyes are collected by a 50x objective and captured by an ultra-sensitive CCD camera. Incident excitation beam scattered off the sample was blocked by notch filters of the corresponding laser wavelengths. Figure 6.5 shows the fluorescent images from pure SiO_2 and Al_2O_3 nanotubes loaded with either R6G or Fluorescein under 442nm laser excitation. Only SiO_2 nanotubes loaded with R6G and Al_2O_3 nanotubes loaded with Fluorescein shows fluorescence that outlines the shape of nanotubes, whereas SiO_2 nanotubes loaded with Fluorescein and Al_2O_3 nanotubes loaded with R6G remained dark. This result confirmed that SiO_2 and Al_2O_3 carry opposite surface charges under neutral pH.

To demonstrate the surface charge discontinuity in heterojunction nanotubes, cationic R6G and anionic Fluorescein was subsequently loaded into the SiO_2/Al_2O_3 nanotubes and washed/diluted using the method described above. A dual laser excitation (He:Cd laser at 442nm and Nd:YAG laser at 532nm) was used to distinguish the emissions from the two laser dyes. R6G fluorescence can be effectively excited at both 442nm and 532nm, whereas Fluorescein has an absorption cut-off at 520nm, and can only be excited at 442nm. Figure 6.4B and C shows the fluorescent images of a single 15μm long heterojunction nanotube under different excitation wavelengths. The upper image (Figure 6.4B) was collected when the nanotube was illuminated at 442nm. Both Fluorescein and R6G showed strong fluorescence, outlining the entire nanotube. The lower image (Figure 6.4C) was collected when the nanotube was excited by 532nm laser. Here only R6G was excited and only the SiO_2 half of the nanotube was lit up. The fluorescence intensity profile along the length of the nanotube also showed an abrupt intensity drop to the background level in the middle of the nanotube, where the heterojunction was expected. This segmented emission confirmed the surface charge polarity switch within the nanotube as designed.

6.4 **Nanotube Diode Device Fabrication**

Nanofluidic diode devices interfaced with microfluidic channels were fabricated using a modified procedure (Figure 6.6). Si nanowires, which will later template the diode nanochannel, were grown laterally from the side walls of micro-trenches that were pre-fabricated on Silicon-on-insulator (SOI) wafers according to a well-established procedure developed in our group[38]. The whole substrate was then coated with 30nm conformal Al_2O_3 layer by ALD. Photoresist were patterned by photolithography to protect the Al_2O_3 coating on one half of the microtrenches and any bridging nanowire while the Al_2O_3 layer on the rest of the substrate was removed by BHF etching. After dissolving the photoresist mask, SiO_2 were deposited on the substrate with RF plasma sputtering. The substrate was then put on a glass slide and packaged in polydimethylsiloxane (PDMS). Holes were then opened on top of the Si pads on both sides of the microtrenches that have bridging nanowires. The top oxide directly beneath the holes was removed by CF_4 anisotropic Reactive Ion Etching (Plasma-Thermal Parallel Plate Plasma Etcher). And the substrate was immediately loaded into XeF_2 etching

chamber to remove the Si pads and nanowires and open SiO_2 microfluidic channels and diode nanofluidic channels. Ag/AgCl electrodes were used in the microfluidic channels on either side of the nanofluidic channels for applying electrical bias. SEM images of a single bridging SiNW at different stage of fabrication was given in Figure 6.7. Fig 6.8 is

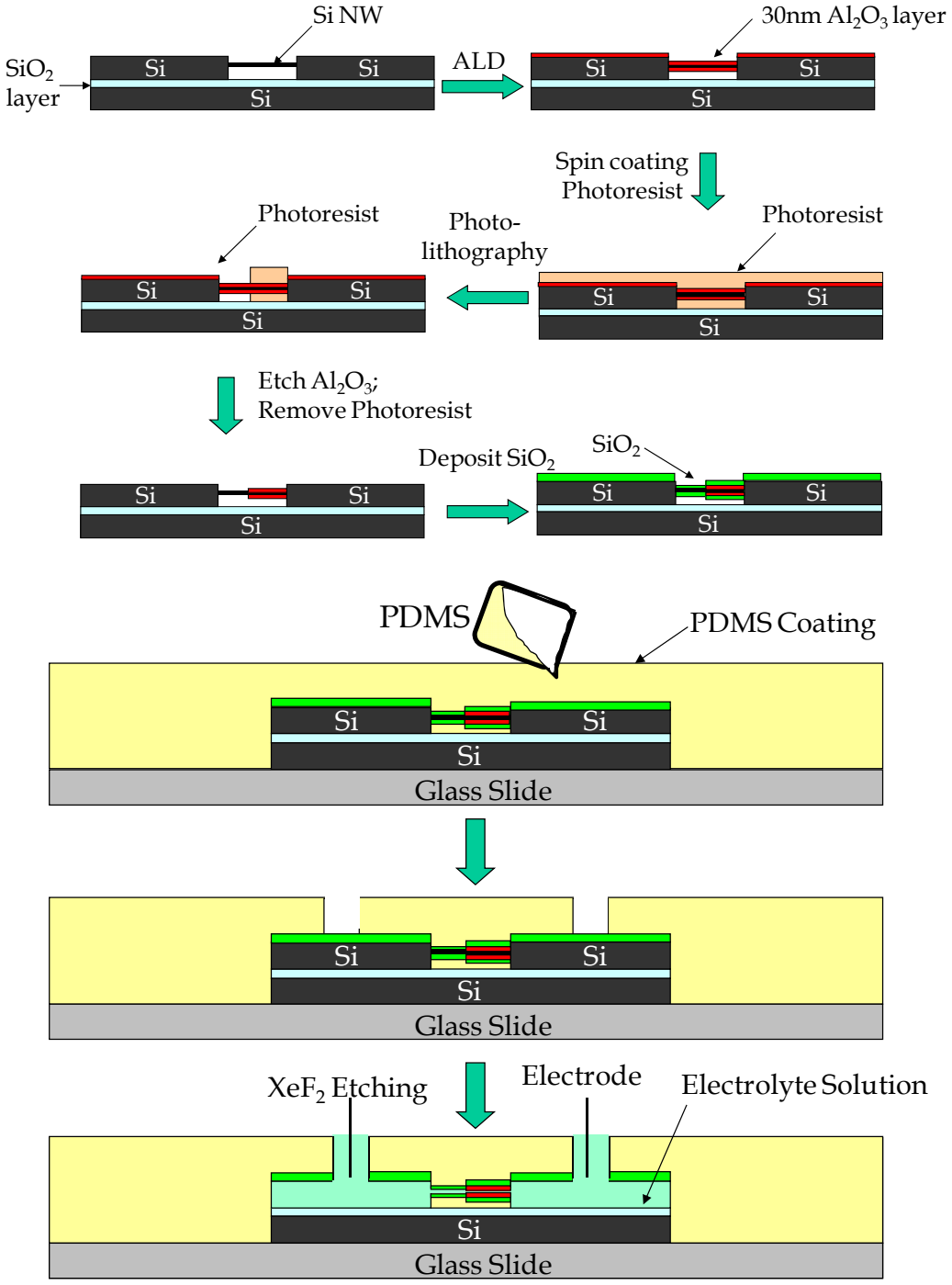

Figure 6.6 Process flow for the fabrication of SiO_2-Al_2O_3 diode device.

an optical image showing the structure of the final diode device while it was being filled by Deionized water.

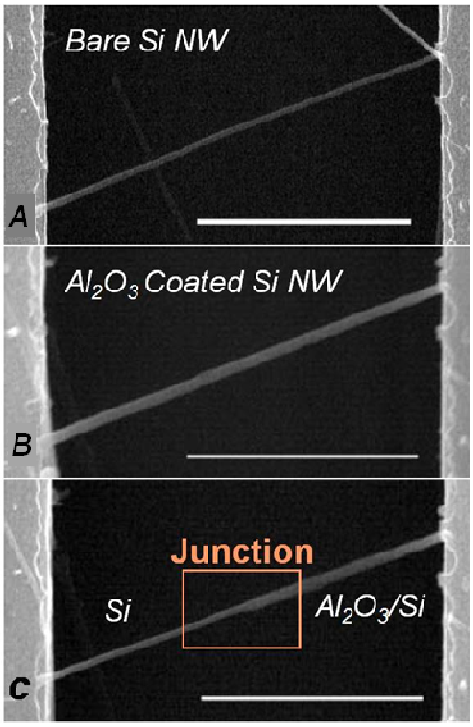

Figure 6.7 SEM images of a Si nanowire bridging the side walls of a 5μm microtrench at different stage of nanotube diode device frabrication. A. As-grown SiNW. **B**. The SiNW coated with a 30nm ALD Al_2O_3 layer. **C**. The Si-Al_2O_3/Si junction formed after removing photoresist mask and etching in BHF solution.

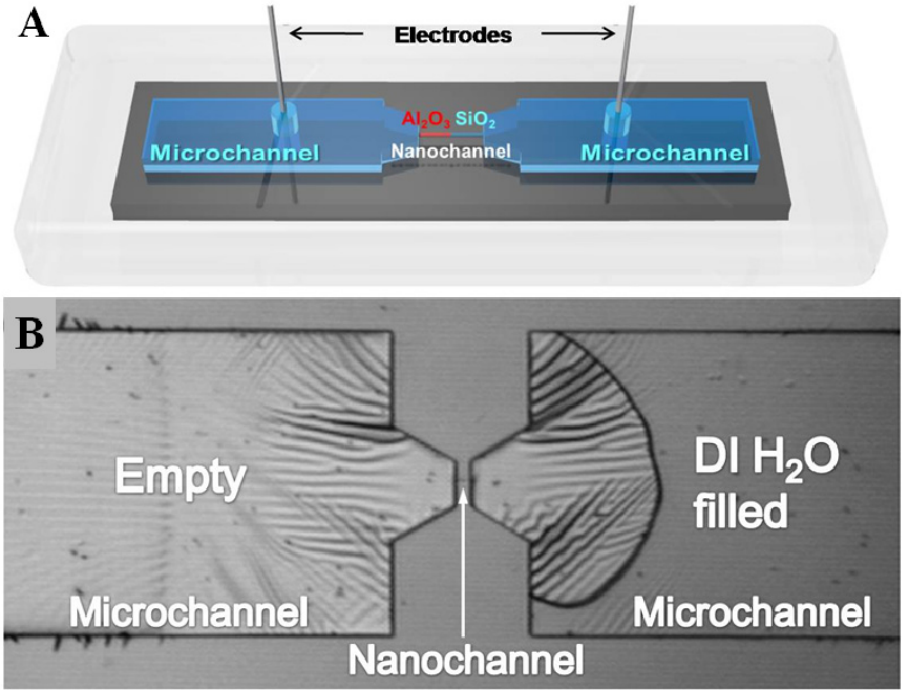

Figure 6.8 Nanofluidic diode device. A. Schematic of the nanotube diode device. **B**. Optical micrograph of a nantube diode device being filled by deionized water.

Figure 6.8A shows a schematic of a finished Nanofluidic diode devices interfaced with microfluidic channels. Figure 6.8B is an optical image showing the structure of the final diode device while it was being filled by deionized water. This final nanofluidic device consists of a heterojunctions SiO_2/Al_2O_3 nanotube connected by two large microfluidic reservoirs at the both ends.

6.5 **Diode Performance**

Previously we have demonstrated that silica nanotubes can serve as p-channel nanofluidic transistors because of their intrinsic negative surface charges[200]. Similarly, alumina nanotubes should serve as n-channel nanofluidic transistors because of their intrinsic positive surface charges. Figure S5 shows the measured ionic conductance of pure Al_2O_3 nanotube devices measured at different concentration of KCl solution under low bias voltage. It shows unipolar characteristics that deviates from the bulk behavior at low concentration, which confirm surface-charge governed transport, in consistent with the SiO_2 nanotube devices reported previously[200,]. The surface charge density can be estimated from the ionic current in the unipolar transport region. It has been demonstrated previously that a SiO_2 nanochannel has a surface charge density of 0.01~0.1C/m^2 [200]. Measurement on pure Al_2O_3 nanotube indicated the ALD grown Al_2O_3 film has a surface charge density of ~0.1C/m^2, consistent with reported values of positively charged Al_2O_3 surfaces[217,218] It should be noted that this value is comparable to that of SiO_2 nanochannels, only with opposite polarity.

Figure 6.9 shows the measured ionic conductance of pure Al_2O_3 nanotube devices measured at different concentration of KCl solution under low bias voltage. It shows unipolar characteristics that deviates from the bulk behavior at low concentration, which confirm surface-charge governed transport, in consistent with the SiO_2 nanotube devices reported previously[13]. The surface charge density can be estimated from the ionic current in the unipolar transport region.

Experimental *I-V* curves obtained at different KCl concentration in ±5V bias range show ionic strength dependent ionic current rectification behaviour (Figure 6.10A). At high KCl concentration (Figure 4c, open diamond), no diode characteristic is observed. This is because under such high ionic strength, $C_{bulk}>>2|\sigma|/rF$, the Debye layer is compressed to within 1 nm and the surface charge are completely shielded by the counter-ions. The surface charge effect on ionic transport becomes negligible, bipolar ionic transport dominates and no current rectification behaviour is expected. At low ionic strength, the Debye length becomes comparable with the nanotube dimension, and the surface effect becomes prominent. Without applied bias along the channel, K^+ ions accumulate in the SiO_2 segment of the nanotube to compensate for the negative surface charge as required by electro-neutrality, whereas Cl^- ions enrich in the Al_2O_3 half (Figure 6.1A). As a positive voltage bias is applied, both K^+ and Cl^- inside the electric double layer are driven towards the junction, results in ion accumulation inside the channel. Continous and large ionic current can thus be maintained. However, under reverse bias, both cations and anions in the electric double layer are driven away from the junction, resulting in concentration depletion in the nanotube, and an energy barrier across the junction and the

ionic current decreases. Figure 4c shows ionic current rectification behaviors at low and intermediate KCl bulk concentration.

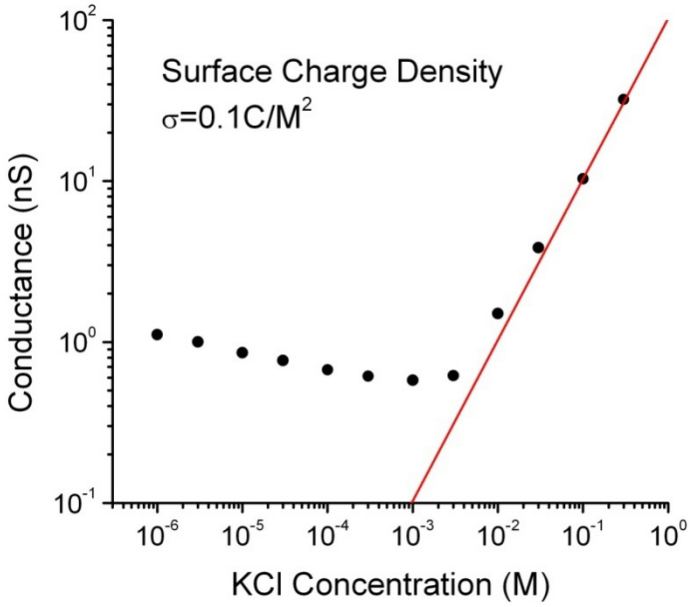

Figure 6.9 The electrical conductance of the pure Al_2O_3 nanotube device. The measured surface charge density of pure Al_2O_3 nanotube was ~0.1C/m^2, comparable to pure SiO_2 nanochanels reported previously (0.01-0.1C/m^2).

Figure 6.10B shows the dependence of rectification ratio on the concentration of bulk KCl solution. The device show slight rectification behavior at low ion concentration ($\leq 10^{-4}$M) with the rectification ratio sits steadily at ~2. The diode characteristic becomes more evident at intermediate ion concentration, and peak at ~3×10^{-3}M, beyond which the rectification ratio drop quickly back to ~2 and continue to decrease till it goes back to the bulk bipolar behavior at high ionic strength. This trend tends to agree with the prediction from the solution of the full 2D Poisson-Nernst-Planck equations[201]. The reduced rectification at low ion concentration can be partially attributed to the concentration polarization at the entrance from the reservoirs to the nanotube, so the potential bias between the two ends of the nanochannel becomes smaller than the bias applied between the two ends of reservoirs. Should this be the case, using longer nanochannel would improve the device performance, since longer nanotubes should be less affected by the concentration polarization. Compared to the 5μm long diode presented in Figure 6.10, a diode channel twice as long shows a distinct enhancement in the rectification ratio at low ionic strength (Figure 6.11), indicating that concentration polarization is partially responsible for the reduced rectification ratio, which can be improved by increasing the aspect ratio of the nanotube[219].

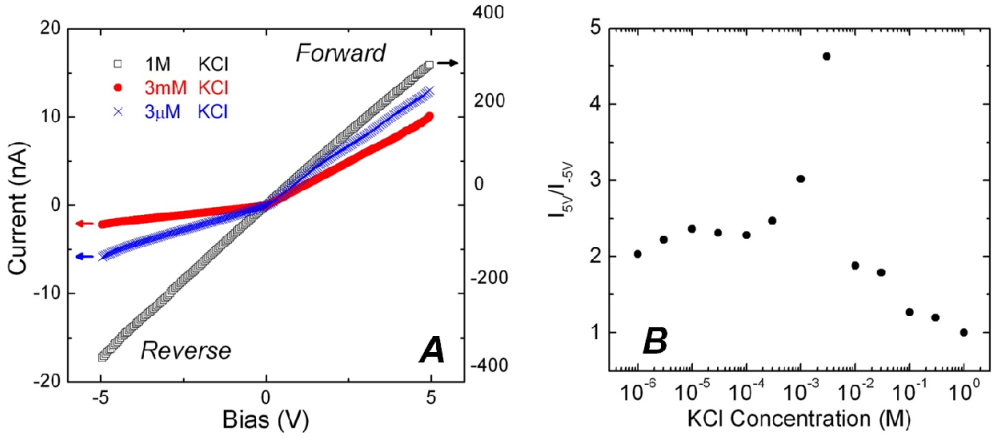

Figure 6.10 Current rectification behavior of a single nanotube diode. A. Current rectification of the nanotube diode under high (1M), medium (3mM) and low (3μM) KCl concentration at neutral pH. **B**. Current ratio of the forward and reverse direction at 5V/-5V at different KCl concentraion.

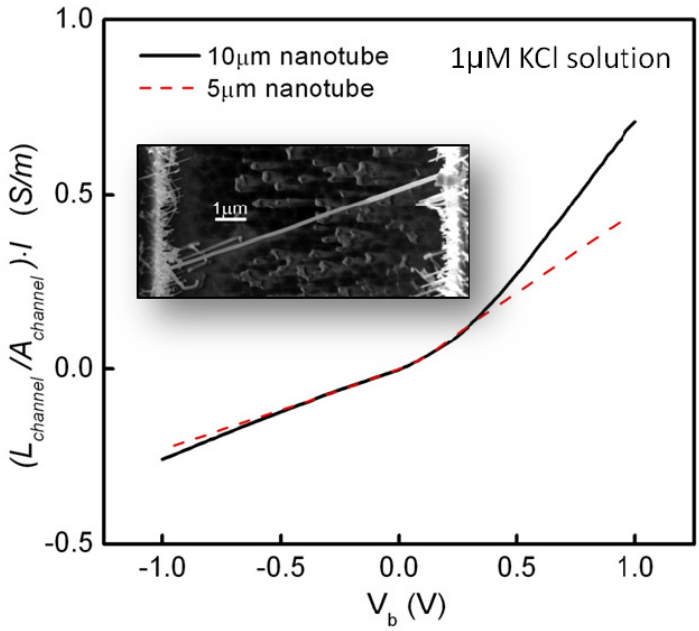

Figure 6.11 The dependence of diode rectification on the length of the nanochannel. The ionic current of a 10μm nanotube diode device normalized to the channel dimension $(L_{channel}/A_{channel})\cdot I$, where I is ionic current measured under bias voltage V_b, $L_{channel}$ is the length of the PN nanochannel and $A_{channel}$ is the area of PN nanochannel cross section) shows a significant increase compared to a typical 5μm nanotube diode device at unipolar concentration region. Inset: SEM images of the 10μm long Si- Al_2O_3/Si nanowire, which was later made into the 10μm nanotube diode device measured.

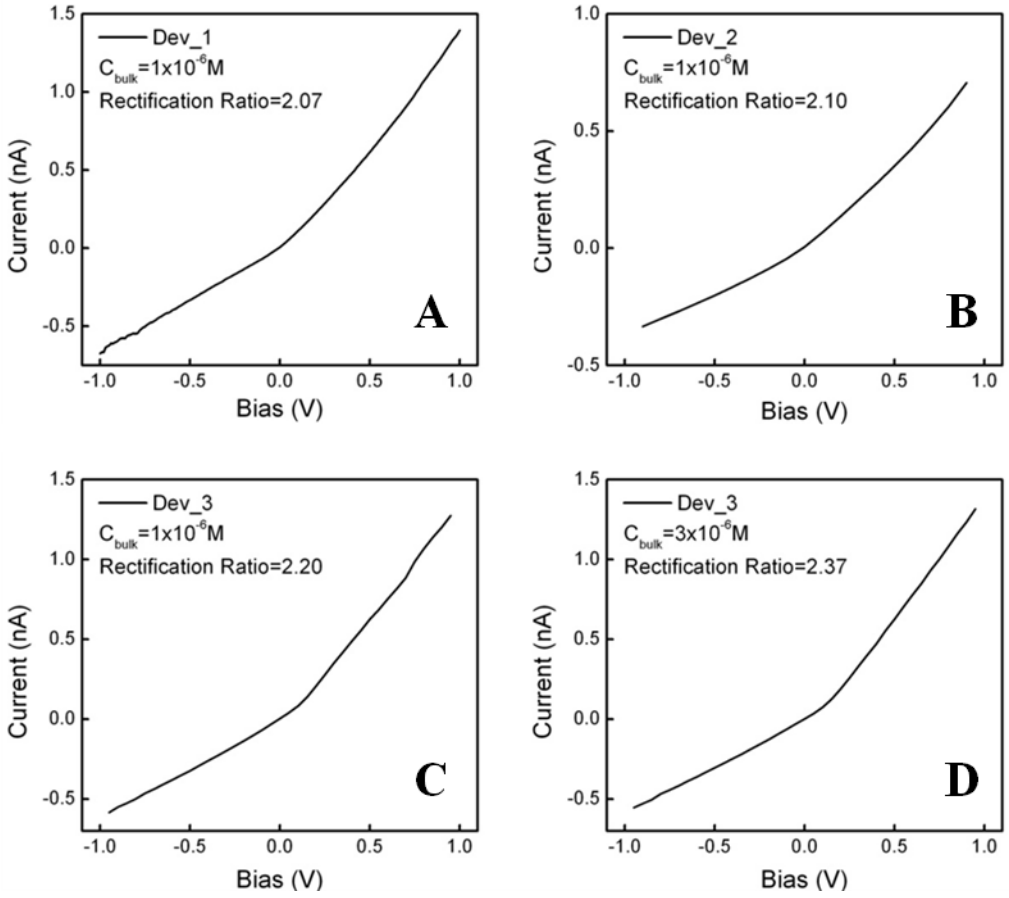

Figure 6.12 Device reproducibility. (a-c) I-V curve of three different nanotube diode devices at 1μM bulk KCl concentration. Current rectification ratios are consistent among devices. (d) I-V curve of Dev_3 at 3μM bulk KCl, consistent with the rectification ratio reported in Figure 6.10.

Figure 6.12 presented I-V curves of 3 other nanotube diode devices at different concentrations. Although the chanel conductances differ for different devices, the ionic rectification ratios rest consistently at ~2:1, which are also similar to the device reported in Figure 6.10.

6.6 **Conclusions**

In this chapter, we have demonstrated the synthesis of the first longitudinal heterostructured SiO_2/Al_2O_3 nanotubes. Comprehensive characterization shows that the nanotubes has heterostructured inner tube walls, as well as a discontinuity of surface charge. These solid state nanofluidic diodes based on intrinsic *pn* ionic junctions, which is geometrically uniform, chemically robust, and compatible with existing lab-on-a-chip technology. The ionic transport through these nanotube heterojunctions exhibits clear current rectification, a signature of ionic diode behavior.

.

Although the experimental trends qualitatively match with the theoretical prediction, the finite rectification ratios in these diode devices deviates from the ideal diode characteristics. Apart from increasing the channel length, further size reduction of such heterojunction nanotubes should also ensure better overlapping of electric double layer, result in a higher built-in potential at the junction and improve the diode performance[201]. In addition, a clear-cut junction enables better control over the ion and electric field distribution at the depletion area and is adopted as an important boundary condition used in all fluidic diode simulations. We believe by improving the junction sharpness, we would also expect enhanced device performance. The development of such nanofluidic devices would enable the modulation of ionic and molecular transport at a more sophisticated level, and lead to large-scale integrated nanofluidic networks and logic circuits.

All images are reproduced with the permission of the American Chemical Society.

Chapter 7
Summary and Future Directions

7.1 **Summary**

Synthetic 1D photonic nanostructures, including semiconductor nanowires and plasmonic metal nanowires has been reviewed in the aspect of their rational synthesize, assembly, novel photonic properties, and biological applications. These nanowires offer a unique toolbox for developing non-invasive multitasking smart optical nanoprobes for subcellular manipulation and studies.

Easy and effective integration of low-loss Ag nanowire plasmonic waveguides and semiconducting subwavelength waveguides (SnO_2 nanoribbons) have been successfully demonstrated on a single nanowire level by bringing them into simple physical contact in crossbar geometry. The plasmonic-photonic coupling was proved to be angle and frequency dependent; small coupling angles and low input frequencies were found in favor of the coupling. The frequency dependent propagation loss was observed in Ag nanowire and was confirmed by quantitative measurement and in agreement with theoretical expectations. A much higher propagation length was measured in chemically synthesized Ag nanowires as compared to those microfabricated polycrystalline Ag waveguides. This was attributed to the high crystallinity and atomically smooth surface of synthetic Ag nanowire which reduce the total propagation loss. Rational integration of dielectric and Ag nanowire waveguide components into hybrid optical-plasmonic routing devices has been demonstrated. This capability is essential for incorporating low-loss Ag nanowire waveguides as practical components into high capacity photonic circuits and optical nanoprobes for single cell endoscopy.

The design and fabrication of the nanoprobe system based on single nanowire waveguides and an optical fiber with tapered tip was demonstrated. These probes are mechanically robust and flexible and can withstand repeated bending, deformation and even buckling without significant deterioration in optical performance, which offers an ideal instrumental platform for out subsequent effort of using these nanoprobes in chemical sensing as well as single cell endoscopy and spot delivery. Influence of optical fibers types and fiber tip tapering technique on the optical coupling efficiency between the nanowire and the fiber tip was investigated and chemical etching of single mode fiber has demonstrated to be the best material for nanoprobe fabrication. By optimizing parameters such as taper cone angle and surface smoothness of the optical fiber, highly effective optical coupling of the tapered single mode optical fiber to both semiconductor and metal nanowire nanoprobes has been achieved. This nanoprobe design requires minimal instrumentation which makes it cost efficient and readily adaptable to average bio-lab environment.

The versatility of the nanoprobe design was first tested by transforming the nanowire probe into a pH sensor with near-field photopolymerization of a copolymer containing pH sensitive dye on the tip of the nanowire. The pH-sensitive nanoprobe was able to report the pH change in the micro-droplet (<10 pL in volume) containing buffer solution at different pH with the excitation of blue light waveguided on the nanoprobe with internal calibration, fast response time and good photostability and reversibility. Such nanoprobe sensors are ideal for high definition spatial and temporal sensing of concentration profile, especially for the kinetic processes in single cell studies for which chemical probes of minute sizes and fast response are desired.

We then extended the scope of the nanowire probe into in-situ single cell imaging. It has been demonstrated that nanowire-based optical probe can deliver payloads into the cell with a high spatiotemporal precision, guide and confine visible light into intracellular compartments selectively and detect optical signals from the subcellular regions with high spatial resolution. The nanoprobe was proven to be biocompatible and the intracellular insertion and illumination of the optical nanoprobe was non-invasive. The effective optical coupling between the fiber optics and the nanowire enables highly localized excitation and detection, limiting the probe volume to the close proximity of the nanowire (i.e., down to pico- and femtoliter), making it a promising candidate for high resolution optical imaging, mapping and chemical/biological sensing along with the precision delivery of gene, proteins, and drugs. None the less, this versatile nanotechnique does not rely on any expensive or bulky instrumentation. It only requires micromanipulator and optical microscope that are readily available in most biological labs. Moreover, different functions can be further integrated to make the whole nanoprobe system even more compact.

In addition, we have demonstrated the synthesis of the first longitudinal heterostructured SiO_2/Al_2O_3 nanotubes. Comprehensive characterization shows that the nanotubes has heterostructured inner tube walls, as well as a discontinuity of surface charge. These solid state nanofluidic diodes based on intrinsic *pn* ionic junctions, which is geometrically uniform, chemically robust, and compatible with existing lab-on-a-chip technology. The ionic transport through these nanotube heterojunctions exhibits clear current rectification, a signature of ionic diode behavior. The development of such nanofluidic devices would enable the modulation of ionic and molecular transport at a more sophisticated level, and lead to large-scale integrated nanofluidic networks and logic circuits.

7.2 **Future Directions**

The future of nanowire-based optical nanoprobe beyond the current stage as described in this dissertation could be towards two major directions.

7.2.1 Multifunctional Integrated Smart Nanoprobe

The feasibility of using nanowire optical probe for spot cargo delivery and subcellular illumination and local signal collection for single living cell study has been separately demonstrated using quantum dot as fluorescent indicator. The logical next step would be combing all these functions in a single multifunctional nanoprobe for precision controlled delivery of cargos that are of biological significance, including DNA, RNA, proteins, polypeptides and drugs, and monitor the cell response in-situ through simultaneous illumination and imaging. Instrumentally, the function integration requires system engineering, but would still rely simple microscopes and micromanipulators and be much more cost and operation friendly than high resolution microscopy such as NSOM and Confocal. Since the nanoprobe only requires microwatts excitation power, LED can be used instead of coherent light source for a more compact, even portable system.

7.2.2 Ag Nanoprobe for Subcellular Imaging, Drug Delivery and Raman Sensing

Ag nanowire has been demonstrated as a highly efficient deep subwavelength plasmonic waveguide with 2D mode confinement. Fabrication of biocompatible Ag nanowire nanoprobe has also been achieved by coupling with a tapered optical fiber tip with relatively high efficiency. One major advantages of developing a new generation of Ag nanoprobe for subcellular studies is its even smaller sizes compared to semiconductor nanowires, which makes it even less invasive to cell membranes. This is especially important to smaller and more delicate cells than the HeLa cancer cell studied previously. Another big bonus is its enhanced electromagnetic field which can be utilized for subcellular surface enhanced raman sensing (SERS) and monitoring, which offers abundant chemical information, of specific proteins during certain kinetic cellular processes. Moreover, cargo delivery with Ag nanowire can be achieved by utilizing the surface thermal effect of the plasmonic waveguide. Target molecules can be linked to the Ag nanowire surface through short double strand DNA in which one strand is bond to metal and the other bond to the target molecule. When light is passed through the Ag nanowire, temperature increase at the metal surface would facilitate the unwinding of the double strand and the release of the target molecule into cytoplasm.

References

1 Michalet, X. *et al.* Quantum Dots for Live Cells, in Vivo Imaging, and Diagnostics. *Science* **307**, 538-544 (2005).

2 Yazawa, M., Koguchi, M. & Hiruma, K. Heteroepitaxial ultrafine wire-like growth of InAs on GaAs substrates. *Appl Phys Lett* **58**, 1080-1082 (1991).

3 Xia, Y. N. *et al.* One-dimensional nanostructures: Synthesis, characterization, and applications. *Adv Mater* **15**, 353-389 (2003).

4 Kuykendall, T., Ulrich, P., Aloni, S. & Yang, P. Complete composition tunability of InGaN nanowires using a combinatorial approach. *Nat Mater* **6**, 951-956 (2007).

5 Sanders, A. W. *et al.* Observation of plasmon propagation, redirection, and fan-out in silver nanowires. *Nano Lett* **6**, 1822-1826 (2006).

6 Ditlbacher, H. *et al.* Silver nanowires as surface plasmon resonators. *Phys Rev Lett* **95**, 257403 (2005).

7 Nayak, K. P. *et al.* Optical nanofiber as an efficient tool for manipulating and probing atomic fluorescence. *Opt Express* **15**, 5431-5438 (2007).

8 Ditlbacher, H. *et al.* Fluorescence imaging of surface plasmon fields. *Appl Phys Lett* **80**, 404-406 (2002).

9 Yin, L. L. *et al.* Subwavelength focusing and guiding of surface plasmons. *Nano Lett* **5**, 1399-1402 (2005).

10 Charbonneau, R., Berini, P., Berolo, E. & Lisicka-Shrzek, E. Experimental observation of plasmon-polariton waves supported by a thin metal film of finite width. *Opt Lett* **25**, 844-846 (2000).

11 Krenn, J. R. *et al.* Non diffraction-limited light transport by gold nanowires. *Europhys Lett* **60**, 663-669 (2002).

12 Lamprecht, B. *et al.* Surface plasmon propagation in microscale metal stripes. *Appl Phys Lett* **79**, 51-53 (2001).

13 Zia, R., Selker, M. D. & Brongersma, M. L. Leaky and bound modes of surface plasmon waveguides. *Phys Rev B* **71**, 165431 (2005).

14 Zia, R., Schuller, J. A. & Brongersma, M. L. Near-field characterization of guided polariton propagation and cutoff in surface plasmon waveguides. *Phys Rev B* **74**, 165415 (2006).

15 Zia, R., Selker, M. D., Catrysse, P. B. & Brongersma, M. L. Geometries and materials for subwavelength surface plasmon modes. *J Opt Soc Am A* **21**, 2442-2446 (2004).

16 Dionne, J. A., Sweatlock, L. A., Atwater, H. A. & Polman, A. Plasmon slot waveguides: Towards chip-scale propagation with subwavelength-scale localization. *Phys Rev B* **73**, 035407 (2006).

17 Dionne, J. A., Lezec, H. J. & Atwater, H. A. Highly confined photon transport in subwavelength metallic slot waveguides. *Nano Lett* **6**, 1928-1932 (2006).

18 Zia, R., Schuller, J. A., Chandran, A. & Brongersma, M. L. Plasmonics: the next chip-scale technology. *Mater Today* **9**, 20-27 (2006).

19 Dickson, R. M. & Lyon, L. A. Unidirectional plasmon propagation in metallic nanowires. *J Phys Chem B* **104**, 6095-6098 (2000).

20 Graff, A., Wagner, D., Ditlbacher, H. & Kreibig, U. Silver nanowires. *Eur Phys J D* **34**, 263-269 (2005).

21 Knight, M. W. *et al.* Nanoparticle-mediated coupling of light into a nanowire. *Nano Lett* **7**, 2346-2350 (2007).

22 Wagner, R. S. & Ellis, W. C. Vapor-liquid-solid mechanism of single crystal growth. *Appl Phys Lett* **4**, 89-90 (1964).

23 Morales, A. M. & Lieber, C. M. A laser ablation method for the synthesis of crystalline semiconductor nanowires. *Science* **279**, 208-211 (1998).

24 Yang, P. D. & Lieber, C. M. Nanorod-superconductor composites: A pathway to materials with high critical current densities. *Science* **273**, 1836-1840 (1996).

25 Wu, Y. Y. & Yang, P. D. Direct observation of vapor-liquid-solid nanowire growth. *J Am Chem Soc* **123**, 3165-3166 (2001).

26 Bjork, M. T. *et al.* One-dimensional heterostructures in semiconductor nanowhiskers. *Appl Phys Lett* **80**, 1058-1060 (2002).

27 Wu, Y. Y. & Yang, P. D. Germanium nanowire growth via simple vapor transport. *Chem Mater* **12**, 605-607 (2000).

28 Molhave, K. *et al.* Epitaxial Integration of Nanowires in Microsystems by Local Micrometer-Scale Vapor-Phase Epitaxy. *Small* **4**, 1741-1746 (2008).

29 Barrelet, C. J., Wu, Y., Bell, D. C. & Lieber, C. M. Synthesis of CdS and ZnS nanowires using single-source molecular precursors. *J Am Chem Soc* **125**, 11498-11499 (2003).

30 Radovanovic, P. V., Barrelet, C. J., Gradecak, S., Qian, F. & Lieber, C. M. General synthesis of manganese-doped II-VI and III-V semiconductor nanowires. *Nano Lett* **5**, 1407-1411 (2005).

31 Johansson, J. *et al.* Structural properties of (111)B-oriented III-V nanowires. *Nat Mater* **7**, 574-580 (2006).

32 Martensson, T. *et al.* Epitaxial growth of indium arsenide nanowires on silicon using nucleation templates formed by self-assembled organic coatings. *Adv Mater* **19**, 1801-1806 (2007).

33 Duan, X. F. & Lieber, C. M. General synthesis of compound semiconductor nanowires. *Adv Mater* **12**, 298-302 (2000).

34 Pan, A. L., Liu, R. B., Sun, M. H. & Ning, C. Z. Quaternary Alloy Semiconductor Nanobelts with Bandgap Spanning the Entire Visible Spectrum. *J Am Chem Soc* **131**, 9502-9503 (2009).

35 Trentler, T. J. *et al.* Solution-Liquid-Solid Growth of Crystalline Iii-V Semiconductors - an Analogy to Vapor-Liquid-Solid Growth. *Science* **270**, 1791-1794 (1995).

36 Kuykendall, T. *et al.* Crystallographic alignment of high-density gallium nitride nanowire arrays. *Nat Mater* **3**, 524-528 (2004).

37 Hochbaum, A. I., Fan, R., He, R. R. & Yang, P. D. Controlled growth of Si nanowire arrays for device integration. *Nano Lett* **5**, 457-460 (2005).

38 He, R. R. *et al.* Si nanowire bridges in microtrenches: Integration of growth into device fabrication. *Adv Mater* **17**, 2098-2102 (2005).

39 Huang, M. H. *et al.* Room-temperature ultraviolet nanowire nanolasers. *Science* **292**, 1897-1899 (2001).

40 Yazawa, M., Koguchi, M., Muto, A., Ozawa, M. & Hiruma, K. Effect of One Monolayer of Surface Gold Atoms on the Epitaxial-Growth of Inas Nanowhiskers. *Appl Phys Lett* **61**, 2051-2053 (1992).

41 Sato, T. *et al.* Site-Controlled Growth of Nanowhiskers. *Appl Phys Lett* **66**, 159-161 (1995).

42 Borgstrom, M. T., Immink, G., Ketelaars, B., Algra, R. & Bakkers, E. P. A. M. Synergetic nanowire growth. *Nat Nanotechnol* **2**, 541-544 (2007).

43 Dick, K. A. *et al.* Failure of the vapor-liquid-solid mechanism in Au-assisted MOVPE growth of InAs nanowires. *Nano Lett* **5**, 761-764 (2005).

44 Martensson, T. *et al.* Nanowire arrays defined by nanoimprint lithography. *Nano Lett* **4**, 699-702 (2004).

45 Ertekin, E., Greaney, P. A., Chrzan, D. C. & Sands, T. D. Equilibrium limits of coherency in strained nanowire heterostructures. *J. Appl. Phys.* **97**, 114325 (2005).

46 Martensson, T. *et al.* Epitaxial III-V nanowires on silicon. *Nano Lett* **4**, 1987-1990 (2004).

47 Tomioka, K., Motohisa, J., Hara, S. & Fukui, T. Control of InAs Nanowire Growth Directions on Si. *Nano Lett* **8**, 3475-3480 (2008).

48 Bakkers, E. P. A. M. *et al.* Epitaxial growth of InP nanowires on germanium. *Nat Mater* **3**, 769-773 (2004).

49 Svensson, C. P. T. *et al.* Monolithic GaAs/InGaP nanowire light emitting diodes on silicon. *Nanotechnology* **19**, 305201 (2008).

50 Mandl, B. *et al.* Au-free epitaxial growth of InAs nanowires. *Nano Lett* **6**, 1817-1821 (2006).

51 Ikejiri, K., Noborisaka, J., Hara, S., Motohisa, J. & Fukui, T. Mechanism of catalyst-free growth of GaAs nanowires by selective area MOVPE. *J Cryst Growth* **298**, 616-619 (2007).

52 Mohan, P., Motohisa, J. & Fukui, T. Controlled growth of highly uniform, axial/radial direction-defined, individually addressable InP nanowire arrays. *Nanotechnology* **16**, 2903-2907 (2005).

53 Mohan, P., Motohisa, J. & Fukui, T. Fabrication of InP/InAs/InP core-multishell heterostructure nanowires by selective area metalorganic vapor phase epitaxy. *Appl Phys Lett* **88**, 133105 (2006).

54 Choi, H. J. *et al.* Self-organized GaN quantum wire UV lasers. *J Phys Chem B* **107**, 8721-8725 (2003).

55 Qian, F. *et al.* Gallium nitride-based nanowire radial heterostructures for nanophotonics. *Nano Lett* **4**, 1975-1979 (2004).

56 Qian, F. *et al.* Multi-quantum-well nanowire heterostructures for wavelength-controlled lasers. *Nat Mater* **7**, 701-706 (2008).

57 Lauhon, L. J., Gudiksen, M. S., Wang, C. L. & Lieber, C. M. Epitaxial core-shell and core-multishell nanowire heterostructures. *Nature* **420**, 57-61 (2002).

58 Algra, R. E. *et al.* Twinning superlattices in indium phosphide nanowires. *Nature* **456**, 369-372 (2008).

59 Wu, Y. Y., Fan, R. & Yang, P. D. Block-by-block growth of single-crystalline Si/SiGe superlattice nanowires. *Nano Lett* **2**, 83-86 (2002).

60 Gudiksen, M. S., Lauhon, L. J., Wang, J., Smith, D. C. & Lieber, C. M. Growth of nanowire superlattice structures for nanoscale photonics and electronics. *Nature* **415**, 617-620 (2002).

61 Bjork, M. T. *et al.* One-dimensional steeplechase for electrons realized. *Nano Lett* **2**, 87-89 (2002).

62 Li, Y., Qian, F., Xiang, J. & Lieber, C. M. Nanowire electronic and optoelectronic devices. *Mater Today* **9**, 18-27 (2006).

63 Dick, K. A. *et al.* Synthesis of branched 'nanotrees' by controlled seeding of multiple branching events. *Nat Mater* **3**, 380-384 (2004).

64 Bierman, M. J., Lau, Y. K. A., Kvit, A. V., Schmitt, A. L. & Jin, S. Dislocation-driven nanowire growth and Eshelby twist. *Science* **320**, 1060-1063 (2008).

65 Zhu, J. *et al.* Formation of chiral branched nanowires by the Eshelby Twist. *Nat Nanotechnol* **3**, 477-481 (2008).

66 Sauer, G. *et al.* Highly ordered monocrystalline silver nanowire arrays. *J Appl Phys* **91**, 3243-3247 (2002).

67 Zong, R. L. *et al.* Synthesis and optical properties of silver nanowire arrays embedded in anodic alumina membrane. *J Phys Chem B* **108**, 16713-16716 (2004).

68 Barbic, M., Mock, J. J., Smith, D. R. & Schultz, S. Single crystal silver nanowires prepared by the metal amplification method. *J Appl Phys* **91**, 9341-9345 (2002).

69 Sun, Y. G. & Xia, Y. N. Large-scale synthesis of uniform silver nanowires through a soft, self-seeding, polyol process. *Adv Mater* **14**, 833-837 (2002).

70 Sun, Y. G., Yin, Y. D., Mayers, B. T., Herricks, T. & Xia, Y. N. Uniform silver nanowires synthesis by reducing AgNO3 with ethylene glycol in the presence of seeds and poly(vinyl pyrrolidone). *Chem Mater* **14**, 4736-4745 (2002).

71 Sun, Y. G., Gates, B., Mayers, B. & Xia, Y. N. Crystalline silver nanowires by soft solution processing. *Nano Lett* **2**, 165-168 (2002).

72 Smith, P. A. *et al.* Electric-field assisted assembly and alignment of metallic nanowires. *Appl Phys Lett* **77**, 1399-1401 (2000).

73 Huang, Y., Duan, X. F., Wei, Q. Q. & Lieber, C. M. Directed assembly of one-dimensional nanostructures into functional networks. *Science* **291**, 630-633 (2001).

74 Messer, B., Song, J. H. & Yang, P. D. Microchannel networks for nanowire patterning. *J Am Chem Soc* **122**, 10232-10233 (2000).

75 Yang, P. D. Wires on water. *Nature* **425**, 243-244 (2003).

76 Tao, A. R., Huang, J. X. & Yang, P. D. Langmuir-Blodgettry of Nanocrystals and Nanowires. *Accounts Chem Res* **41**, 1662-1673 (2008).

77 Ahn, J. H. *et al.* Heterogeneous three-dimensional electronics by use of printed semiconductor nanomaterials. *Science* **314**, 1754-1757 (2006).

78 Ashkin, A., Dziedzic, J. M., Bjorkholm, J. E. & Chu, S. Observation of a single-beam gradient force optical trap for dielectric particles. *Opt Lett* **11**, 288-290 (1986).

79 Grier, D. G. A revolution in optical manipulation. *Nature* **424**, 810-816 (2003).

80 Korda, P., Spalding, G. C., Dufresne, E. R. & Grier, D. G. Nanofabrication with holographic optical tweezers. *Rev Sci Instrum* **73**, 1956-1957 (2002).

81 Pauzauskie, P. J. *et al.* Optical trapping and integration of semiconductor nanowire assemblies in water. *Nat Mater* **5**, 97-101 (2006).

82 Agarwal, R. *et al.* Manipulation and assembly of nanowires with holographic optical traps. *Opt Express* **13**, 8906-8912 (2005).

83 Chiou, P. Y., Ohta, A. T. & Wu, M. C. Massively parallel manipulation of single cells and microparticles using optical images. *Nature* **436**, 370-372 (2005).

84 Jamshidi, A. *et al.* Dynamic manipulation and separation of individual semiconducting and metallic nanowires. *Nat Photonics* **2**, 85-89 (2008).

85 Yan, H. Q. *et al.* Dendritic nanowire ultraviolet laser array. *J Am Chem Soc* **125**, 4728-4729 (2003).

86 Sirbuly, D. J., Law, M., Yan, H. Q. & Yang, P. D. Semiconductor nanowires for subwavelength photonics integration. *J Phys Chem B* **109**, 15190-15213 (2005).

87 Johnson, J. C., Yan, H. Q., Yang, P. D. & Saykally, R. J. Optical cavity effects in ZnO nanowire lasers and waveguides. *J Phys Chem B* **107**, 8816-8828 (2003).

88 Zapien, J. A. *et al.* Room-temperature single nanoribbon lasers. *Appl Phys Lett* **84**, 1189-1191 (2004).

89 Duan, X. F., Huang, Y., Agarwal, R. & Lieber, C. M. Single-nanowire electrically driven lasers. *Nature* **421**, 241-245 (2003).

90 Johnson, J. C. *et al.* Single gallium nitride nanowire lasers. *Nat Mater* **1**, 106-110 (2002).

91 Chin, A. H. *et al.* Near-infrared semiconductor subwavelength-wire lasers. *Appl Phys Lett* **88**, 163115 (2006).

92 Pauzauskie, P. J., Sirbuly, D. J. & Yang, P. D. Semiconductor nanowire ring resonator laser. *Phys Rev Lett* **96**, 143903 (2006).

93 Zimmler, M. A., Bao, J., Capasso, F., Muller, S. & Ronning, C. Laser action in nanowires: Observation of the transition from amplified spontaneous emission to laser oscillation. *Appl Phys Lett* **93**, 051101 (2008).

94 Barrelet, C. J. *et al.* Hybrid single-nanowire photonic crystal and microresonator structures. *Nano Lett* **6**, 11-15 (2006).

95 Maslov, A. V. & Ning, C. Z. Far-field emission of a semiconductor nanowire laser. *Opt Lett* **29**, 572-574 (2004).

96 Van Vugt, L. K., Ruhle, S. & Vanmaekelbergh, D. Phase-correlated nondirectional laser emission from the end facets of a ZnO nanowire. *Nano Lett* **6**, 2707-2711 (2006).

97 Hua, B., Motohisa, J., Kobayashi, Y., Hara, S. & Fukui, T. Single GaAs/GaAsP Coaxial Core-Shell Nanowire Lasers. *Nano Lett* **9**, 112-116 (2009).

98 Skold, N. *et al.* Growth and optical properties of strained GaAs-GaxIn1-xP core-shell nanowires. *Nano Lett* **5**, 1943-1947 (2005).

99 Hua, B., Motohisa, J., Ding, Y., Hara, S. & Fukui, T. Characterization of Fabry-Perot microcavity modes in GaAs nanowires fabricated by selective-area metal organic vapor phase epitaxy. *Appl Phys Lett* **91**, 131112 (2007).

100 Duan, X. F., Huang, Y., Cui, Y., Wang, J. F. & Lieber, C. M. Indium phosphide nanowires as building blocks for nanoscale electronic and optoelectronic devices. *Nature* **409**, 66-69 (2001).

101 Huang, Y., Duan, X. F. & Lieber, C. M. Nanowires for integrated multicolor nanophotonics. *Small* **1**, 142-147 (2005).

102 Zhong, Z. H., Qian, F., Wang, D. L. & Lieber, C. M. Synthesis of p-type gallium nitride nanowires for electronic and photonic nanodevices. *Nano Lett* **3**, 343-346 (2003).

103 Minot, E. D. *et al.* Single quantum dot nanowire LEDs. *Nano Lett* **7**, 367-371 (2007).

104 Law, M. *et al.* Nanoribbon waveguides for subwavelength photonics integration. *Science* **305**, 1269-1273 (2004).

105 O'Brien, J. L., Pryde, G. J., White, A. G., Ralph, T. C. & Branning, D. Demonstration of an all-optical quantum controlled-NOT gate. *Nature* **426**, 264-267 (2003).

106 Ibrahim, T. A. *et al.* All-optical switching in a laterally coupled microring resonator by carrier injection. *IEEE Photonic Tech L* **15**, 36-38 (2003).

107 Tong, L. M. *et al.* Subwavelength-diameter silica wires for low-loss optical wave guiding. *Nature* **426**, 816-819 (2003).

108 Sirbuly, D. J. *et al.* Optical routing and sensing with nanowire assemblies. *P Natl Acad Sci USA* **102**, 7800-7805 (2005).

109 Nakayama, Y. *et al.* Tunable nanowire nonlinear optical probe. *Nature* **447**, 1908-1102 (2007).

110 Fedutik, Y., Temnov, V., Woggon, U., Ustinovich, E. & Artemyev, M. Exciton-plasmon interaction in a composite metal-insulator-semiconductor nanowire system. *J Am Chem Soc* **129**, 14939-14945 (2007).

111 Akimov, A. V. *et al.* Generation of single optical plasmons in metallic nanowires coupled to quantum dots. *Nature* **450**, 402-406 (2007).

112 Pyayt, A. L., Wiley, B., Xia, Y., Chen, A. & Dalton, L. Integration of photonic and silver nanowire plasmonic waveguides. *Nat Nanotechnol* **3**, 660-665 (2008).

113 Yan, R. X., Pausauskie, P., Huang, J. X. & Yang, P. D. Direct photonic-plasmonic coupling and routing in single nanowires. *P Natl Acad Sci USA* **106**, 21045-21050 (2009).

114 Kind, H., Yan, H. Q., Messer, B., Law, M. & Yang, P. D. Nanowire ultraviolet photodetectors and optical switches. *Adv Mater* **14**, 158-160 (2002).

115 Wang, J. F., Gudiksen, M. S., Duan, X. F., Cui, Y. & Lieber, C. M. Highly polarized photoluminescence and photodetection from single indium phosphide nanowires. *Science* **293**, 1455-1457 (2001).

116 Gu, Y. *et al.* Near-field scanning photocurrent microscopy of a nanowire photodetector. *Appl Phys Lett* **87**, 043111 (2005).

117 Hayden, O., Agarwal, R. & Lieber, C. M. Nanoscale avalanche photodiodes for highly sensitive and spatially resolved photon detection. *Nat Mater* **5**, 352-356 (2006).

118 Campbell, J. C. Recent advances in telecommunications avalanche photodiodes. *J Lightwave Technol* **25**, 109-121 (2007).

119 Hayden, O. & Payne, C. K. Nanophotonic light sources for fluorescence spectroscopy and cellular imaging. *Angew Chem Int Ed* **44**, 1395-1398 (2005).

120 Oregan, B. & Gratzel, M. A Low-Cost, High-Efficiency Solar-Cell Based on Dye-Sensitized Colloidal Tio2 Films. *Nature* **353**, 737-740 (1991).

121 Law, M., Greene, L. E., Johnson, J. C., Saykally, R. & Yang, P. D. Nanowire dye-sensitized solar cells. *Nat Mater* **4**, 455-459 (2005).

122 Law, M. *et al.* ZnO-Al2O3 and ZnO-TiO2 core-shell nanowire dye-sensitized solar cells. *J Phys Chem B* **110**, 22652-22663 (2006).

123 Tian, B. Z. *et al.* Coaxial silicon nanowires as solar cells and nanoelectronic power sources. *Nature* **449**, 885-889 (2007).

124 Kim, W., Ng, J. K., Kunitake, M. E., Conklin, B. R. & Yang, P. D. Interfacing silicon nanowires with mammalian cells. *J Am Chem Soc* **129**, 7228-7229 (2007).

125 Hallstrom, W. *et al.* Gallium phosphide nanowires as a substrate for cultured neurons. *Nano Lett* **7**, 2960-2965 (2007).

126 Shalek, A. K. *et al.* Vertical silicon nanowires as a universal platform for delivering biomolecules into living cells. *P Natl Acad Sci USA* **107**, 1870-1875 (2010).

127 Patolsky, F. *et al.* Detection, stimulation, and inhibition of neuronal signals with high-density nanowire transistor arrays. *Science* **313**, 1100-1104 (2006).

128 Murashov, V. & Howard, J. The US must help set international standards for nanotechnology. *Nat Nanotechnol* **3**, 635-636 (2008).

129 Maslov, A. V. & Ning, C. Z. Size reduction of a semiconductor nanowire laser by using metal coating. *Proc SPIE* **6468**, 64680I (2007).

130 Hill, M. T. *et al.* Lasing in metallic- Coated nanocavities. *Nat Photonics* **1**, 589-594 (2007).

131 Oulton, R. F., Sorger, V. J., Genov, D. A., Pile, D. F. P. & Zhang, X. A hybrid plasmonic waveguide for subwavelength confinement and long-range propagation. *Nat Photonics* **2**, 496-500 (2008).

132 Lal, S., Link, S. & Halas, N. J. Nano-optics from sensing to waveguiding. *Nat Photonics* **1**, 641-648 (2007).

133 Ozbay, E. Plasmonics: Merging photonics and electronics at nanoscale dimensions. *Science* **311**, 189-193 (2006).

134 Barnes, W. L., Dereux, A. & Ebbesen, T. W. Surface plasmon subwavelength optics. *Nature* **424**, 824-830 (2003).

135 Krenn, J. R. & Weeber, J. C. Surface plasmon polaritons in metal stripes and wires. *Philos T Roy Soc A* **362**, 739-756 (2004).

136 Maier, S. A. Plasmonics: The promise of highly integrated optical devices. *IEEE J Sel Top Quant* **12**, 1671-1677 (2006).

137 Maier, S. A. *et al.* Local detection of electromagnetic energy transport below the diffraction limit in metal nanoparticle plasmon waveguides. *Nat Mater* **2**, 229-232 (2003).

138 Pan, Z. W., Dai, Z. R. & Wang, Z. L. Nanobelts of semiconducting oxides. *Science* **291**, 1947-1949 (2001).

139 Haber, L. H., Schaller, R. D., Johnson, J. C. & Saykally, R. J. Shape control of near-field probes using dynamic meniscus etching. *J Microsc-Oxford* **214**, 27-35 (2004).
140 Raether, H. *Surface Plasmons on Smooth and Rough Surfaces and on Gratings* (Springer-Verlag, 1988).
141 Novotny, L. & Hafner, C. Light-Propagation in a Cylindrical Wave-Guide with a Complex, Metallic, Dielectric Function. *Phys Rev E* **50**, 4094-4106 (1994).
142 Laroche, T. & Girard, C. Near-field optical properties of single plasmonic nanowires. *Appl Phys Lett* **89**, 233119 (2006).
143 Laroche, T., Vial, A. & Roussey, M. Crystalline structure's influence on the near-field optical properties of single plasmonic nanowires. *Appl Phys Lett* **91**, 123101 (2007).
144 Haber, L. H., Schaller, R. D., Johnson, J. C. & Saykally, R. J. Shape control of near-field probes using dynamic meniscus etching. *J. Microsc.* **214**, 27-35 (2004).
145 Tan, W., Shi, Z. Y. & Kopelman, R. Development of submicron chemical fiber optic sensors. *Anal Chem* **64**, 2985-2990 (1992).
146 Tan, W. H., Shi, Z. Y., Smith, S., Birnbaum, D. & Kopelman, R. Submicrometer Intracellular Chemical Optical Fiber Sensors. *Science* **258**, 778-781 (1992).
147 Leonhard.H, Gordon, L. & Livingst.R. Acid-Base Equilibria of Fluorescein and 2',7'-Dichlorofluorescein in Their Ground and Fluorescent States. *J Phys Chem-Us* **75**, 245-249 (1971).
148 Martin, M. M. & Lindqvist, L. PH-Dependence of Fluorescein Fluorescence. *J Lumin* **10**, 381-390 (1975).
149 Sjoback, R., Nygren, J. & Kubista, M. Absorption and Fluorescence Properties of Fluorescein. *Spectrochim Acta A* **51**, L7-L21 (1995).
150 Haugland, R. P., Spence, M. T. Z., Johnson, I. D. & Basey, A. *The handbook : a guide to fluorescent probes and labeling technologies*. 10th edn, (Molecular Probes, 2005).
151 Munkholm, C., Parkinson, D. R. & Walt, D. R. Intramolecular Fluorescence Self-Quenching of Fluoresceinamine. *J Am Chem Soc* **112**, 2608-2612 (1990).
152 Hicks, G. P. & Updike, S. J. Preparation and Characterization of Lyophilized Polyacrylamide Enzyme Gels for Chemical Analysis. *Anal Chem* **38**, 726-730 (1966).
153 Tazuke, S. & Kimura, H. Surface Photografting .2. Modification of Polypropylene Film Surface by Graft-Polymerization of Acrylamide. *Makromol Chem* **179**, 2603-2612 (1978).
154 Wu, L. Y., Ross, B. M., Hong, S. & Lee, L. P. Bioinspired Nanocorals with Decoupled Cellular Targeting and Sensing Functionality. *Small* **6**, 503-507.
155 Panyam, J. & Labhasetwar, V. Biodegradable nanoparticles for drug and gene delivery to cells and tissue *Adv Drug Del Rev* **55**, 329-347 (2003).
156 Kam, N. W. S., Liu, Z. A. & Dai, H. J. Carbon nanotubes as intracellular transporters for proteins and DNA: An investigation of the uptake mechanism and pathway. *Angew Chem Int Ed* **45**, 577-581 (2006).
157 Park, J.-H., von Maltzahn, G., Ruoslahti, E., Bhatia, S. N. & Sailor, M. J. Micellar hybrid nanoparticles for simultaneous magnetofluorescent imaging and drug delivery. *Angew Chem Int Ed* **47**, 7284-7288 (2008).

158 Cai, D. *et al.* Highly efficient molecular delivery into mammalian cells using carbon nanotube spearing. *Nat Methods* **2**, 449-454 (2005).
159 Lee, S. E., Liu, G. L., Kim, F. & Lee, L. P. Remote optical switch for localized and selective control of gene interference. *Nano Lett* **9**, 562-570 (2009).
160 Lee, S. E. *et al.* Biologically Functional Cationic Phospholipid-Gold Nanoplasmonic Carriers of RNA. *J Am Chem Soc* **131**, 14066-14074 (2009).
161 Alivisatos, A. P., Gu, W. W. & Larabell, C. Quantum dots as cellular probes. *Annu Rev Biomed Eng* **7**, 55-76 (2005).
162 Jin, H. *et al.* Detection of single-molecule H_2O_2 signaling from epidermal growth factor receptor using fluorescent single-walled carbon nanotubes. *Nat Nanotech* **5**, 302-309 (2010).
163 Liu, G. L. *et al.* A nanoplasmonic molecular ruler for measuring nuclease activity and DNA footprinting. *Nat Nanotechnol* **1**, 47-52 (2006).
164 Jun, Y. W. *et al.* Continuous imaging of plasmon rulers in live cells reveals early stage caspase-3 activation at the single molecule level. *P Natl Acad Sci USA* **106**, 17735-17740 (2009).
165 Liu, G. L., Lu, Y., Kim, J., Doll, J. C. & Lee, L. P. Magnetic nanocrescents as controllable surface-enhanced Raman scattering nanoprobes for biomolecular imaging. *Adv Mater* **17**, 2683-2688 (2005).
166 Liu, G. L., Long, Y. T., Choi, Y., Kang, T. & Lee, L. P. Quantized plasmon quenching dips nanospectroscopy via plasmon resonance energy transfer. *Nat Methods* **4**, 1015-1017 (2007).
167 Choi, Y. H., Kang, T. & Lee, L. P. Plasmon Resonance Energy Transfer (PRET)-based Molecular Imaging of Cytochrome c in Living Cells. *Nano Lett* **9**, 85-90 (2009).
168 Choi, Y., Park, Y., Kang, T. & Lee, L. P. Selective and sensitive detection of metal ions by plasmonic resonance energy transfer-based nanospectroscopy. *Nat Nanotechnol* **4**, 742-746 (2009).
169 Hell, S. W. Far-field optical nanoscopy. *Science* **316**, 1153-1158 (2007).
170 Eggeling, C. *et al.* Direct observation of the nanoscale dynamics of membrane lipids in a living cell. *Nature* **457**, 1159-1162 (2009).
171 Zhuang, X. Nano-imaging with STORM. *Nat Photonnics* **3**, 365-367 (2009).
172 Tan, W., Shi, Z.-Y., Smith, S., Birnbaum, D. & Kopelman, R. Submicrometer intracellular chemical optical fiber sensors. *Science* **258**, 778-781 (1992).
173 Vo-Dinh, T., Alarie, J.-P., Cullum, B. M. & Griffin, G. D. Antibody-based nanoprobe for measurement of a fluorescent analyte in a single cell. *Nat Biotechnol* **18**, 764-767 (2000).
174 Kasili, P. M., Song, J. M. & Vo-Dinh, T. Optical sensor for the detection of Caspase-9 activity in a single cell. *J Am Chem Soc* **126**, 2799-2806 (2004).
175 Vo-Dinh, T. & Kasili, P. Fiber-optic nanosensors for single-cell monitoring. *Anal Bioanal Chem* **382**, 918-925 (2005).
176 Flusberg, B. A. *et al.* Fiber-optic fluorescence imaging. *Nat Methods* **2**, 941-950 (2005).
177 Wu, Y. I. *et al.* A genetically encoded photoactivatable Rac controls the motility of living cells. *Nature* **461**, 104-108 (2009).

178 Andrasfalvy, B. K., Zemelman, B. V., Tang, J. Y. & Vaziri, A. Two-photon single-cell optogenetic control of neuronal activity by sculpted light. *P Natl Acad Sci USA* **107**, 11981-11986 (2010).
179 Lippincott-Schwartz, J. & Patterson, G. H. Development and use of fluorescent protein markers in living cells. *Science* **300**, 87-91 (2003).
180 Bulina, M. E. *et al.* A genetically encoded photosensitizer. *Nat Biotechnol* **24**, 95-99 (2006).
181 Law, M. *et al.* Nanoribbon waveguides for subwavelength photonics integration. *Science* **305**, 1269-1273 (2004).
182 Sirbuly, D. J. *et al.* Optical routing and sensing with nanowire assemblies. *P Natl Acad Sci USA* **102**, 7800-7805 (2005).
183 Kim, W., Ng, J. K., Kunitake, M. E., Conklin, B. R. & Yang, P. Interfacing silicon nanowires with mammalian cells. *J Am Chem Soc* **129**, 7228-7229 (2007).
184 Hallstrom, W. *et al.* Gallium phosphide nanowires as a substrate for cultured neurons. *Nano Lett* **7**, 2960-2965 (2007).
185 Shalek, A. K. *et al.* Vertical silicon nanowires as a universal platform for delivering biomolecules into living cells. *P Natl Acad Sci USA* **107**, 1870-1875 (2010).
186 Chen, X., Kis, A., Zettl, A. & Bertozzi, C. R. A cell nanoinjector based on carbon nanotubes. *P Natl Acad Sci USA* **104**, 8218-8222 (2007).
187 Yum, K., Na, S., Xiang, Y., Wang, N. & Yu, M.-F. Mechanochemical delivery and dynamic tracking of fluorescent quantum dots in the cytoplasm and nucleus of living cells. *Nano Lett* **9**, 2193-2198 (2009).
188 Goldberger, J., Fan, R. & Yang, P. D. Inorganic nanotubes: A novel platform for nanofluidics. *Accounts Chem Res* **39**, 239-248 (2006).
189 Han, J. Y., Fu, J. P. & Schoch, R. B. Molecular sieving using nanofilters: Past, present and future. *Lab Chip* **8**, 23-33 (2008).
190 Mijatovic, D., Eijkel, J. C. T. & van den Berg, A. Technologies for nanofluidic systems: top-down vs. bottom-up - a review. *Lab Chip* **5**, 492-500 (2005).
191 White, H. S. & Bund, A. Ion current rectification at nanopores in glass membranes. *Langmuir* **24**, 2212-2218 (2008).
192 Martin, C. R. & Siwy, Z. S. Learning nature's way: Biosensing with synthetic nanopores. *Science* **317**, 331-332 (2007).
193 Dekker, C. Solid-state nanopores. *Nat Nanotechnol* **2**, 209-215 (2007).
194 Mannion, J. T. & Craighead, H. G. Nanofluidic structures for single biomolecule fluorescent detection. *Biopolymers* **85**, 131-143 (2007).
195 Fan, R. *et al.* DNA translocation in inorganic nanotubes. *Nano Lett* **5**, 1633-1637 (2005).
196 Tegenfeldt, J. O. *et al.* Micro- and nanofluidics for DNA analysis. *Anal Bioanal Chem* **378**, 1678-1692 (2004).
197 Sauer-Budge, A. F., Nyamwanda, J. A., Lubensky, D. K. & Branton, D. Unzipping kinetics of double-stranded DNA in a nanopore. *Phys Rev Lett* **90**, 238101 (2003).
198 Daiguji, H., Yang, P. D. & Majumdar, A. Ion transport in nanofluidic channels. *Nano Lett* **4**, 137-142 (2004).

199 Fan, R., Yue, M., Karnik, R., Majumdar, A. & Yang, P. D. Polarity switching and transient responses in single nanotube nanofluidic transistors. *Phys Rev Lett* **95**, 086607 (2005).

200 Karnik, R. *et al.* Electrostatic control of ions and molecules in nanofluidic transistors. *Nano Lett* **5**, 943-948 (2005).

201 Daiguji, H., Oka, Y. & Shirono, K. Nanofluidic diode and bipolar transistor. *Nano Lett* **5**, 2274-2280 (2005).

202 Pennathur, S., Eijkel, J. C. T. & van den Berg, A. Energy conversion in microsystems: is there a role for micro/nanofluidics? *Lab Chip* **7**, 1234-1237 (2007).

203 Gijs, M. A. M. Device physics - Will fluidic electronics take off? *Nat Nanotechnol* **2**, 268-270 (2007).

204 van der Heyden, F. H. J., Bonthuis, D. J., Stein, D., Meyer, C. & Dekker, C. Electrokinetic energy conversion efficiency in nanofluidic channels. *Nano Lett* **6**, 2232-2237 (2006).

205 Miedema, H. *et al.* A biological porin engineered into a molecular, nanofluidic diode. *Nano Lett* **7**, 2886-2891 (2007).

206 Alcaraz, A. *et al.* A pH-tunable nanofluidic diode: Electrochemical rectification in a reconstituted single ion channel. *J Phys Chem B* **110**, 21205-21209 (2006).

207 Vlassiouk, I. & Siwy, Z. S. Nanofluidic diode. *Nano Lett* **7**, 552-556 (2007).

208 Karnik, R., Duan, C. H., Castelino, K., Daiguji, H. & Majumdar, A. Rectification of ionic current in a nanofluidic diode. *Nano Lett* **7**, 547-551 (2007).

209 Kalman, E. B., Vlassiouk, I. & Siwy, Z. S. Nanofluidic bipolar transistors. *Adv Mater* **20**, 293-297 (2008).

210 Nishizawa, M., Menon, V. P. & Martin, C. R. Metal Nanotubule Membranes with Electrochemically Switchable Ion-Transport Selectivity. *Science* **268**, 700-702 (1995).

211 Stein, D., Kruithof, M. & Dekker, C. Surface-charge-governed ion transport in nanofluidic channels. *Phys Rev Lett* **93**, 035901 (2004).

212 Coster, H. G. L. A Quantitative Analysis of the Voltage-Current Relationships of Fixed Charge Membranes and the Associated Property of "Punch-Through". *Biophys J* **5**, 669–686 (1965).

213 Bassignana, I. C. & Reiss, H. Ion-Transport and Water Dissociation in Bipolar Ion-Exchange Membranes. *J Membr Sci* **15**, 27-41 (1983).

214 Mafe, S. & Ramirez, P. Electrochemical characterization of polymer ion-exchange bipolar membranes. *Acta Polym* **48**, 234-250 (1997).

215 Parfitt, G. D. Surface-Chemistry of Oxides. *Pure Appl Chem* **48**, 415-418 (1976).

216 Fan, R. *et al.* Fabrication of silica nanotube arrays from vertical silicon nanowire templates. *J Am Chem Soc* **125**, 5254-5255 (2003).

217 Kosmulski, M. in *Encyclopedia of surface and colloid science* (ed Arthur T. Hubbard) 1627-1636 (Marcel Dekker, New York, 2002).

218 Sprycha, R. Electrical Double-Layer at Alumina Electrolyte Interface 1. Surface-Charge and Zeta Potential. *J Colloid Interf Sci* **127**, 1-11 (1989).

219 Vlassiouk, I., Smirnov, S. & Siwy, Z. Nanofluidic ionic diodes. Comparison of analytical and numerical solutions. *ACS Nano* **2**, 1589-1602 (2008).

Bibliography

Ruoxue Yan was born in Beijing, China. She attended the Huiwen High School in Beijing, where she joined the top class in science and engineering in her second year. She was also active in extracurricular activities and social services and was an active member of the school orchestra, school radio station and was elected the president of the student union for two consecutive years. In 1998, she graduated with honor for science and engineering, as well as many state and city awards in arts and social sciences. She was then admitted into the Chemistry Department of Tsinghua University, the best research university in sciences and engineering. In 2002, she received her bachelor's degree with honors in chemistry and continued in the Department of Chemistry as a master's degree program student by joining Professor Yadong Li's group to explore the novel nanoscale rare-earth fluorescent materials and explored their interesting up-conversion optical behavior. Her 3 years of research has lead to 2 research papers in prestigious science journals as first author and 4 others as a co-author. In 2005, she received her master's degree in chemistry with highest honors, with accomplishment of her master research thesis – "*Controlled Synthesis, Characterization and Optical Properties of Luminescent Lanthanide Nano-Materials*". In the same year, she began her study in the Ph.D. program in the University of California at Berkeley, where she joined Professor Peidong Yang's group to look for fun particularly in the realm of 1D inorganic nanostructures. In the past five years, her research interests include (1) the nanowire-based biocompatible optical nanoprobe for single cell sensing and endoscopy, and (2) the inorganic nanotube nanofluidics for ion transport control. In the end, these works were recognized by the prestigious *Chinese Government Award for Outstanding Self-Financed Students Abroad*, and also incubated into the completion of this long, but hopefully interesting dissertation.

Publication List

1. **Yan R.X.*,** Park J.H.*, Choi Y.H., Heo C.J., Luke L., Yang P.D. "Nanowire-Based Single Cell Endoscopy" Submitted to Nature Nanotechnology.
2. Yang P.D., **Yan R.X.**, Fardy M. "Semiconductor Nanowire: What's Next?" *Nano Letters* **2010**, 10, 1529.
3. **Yan R.X.**, Pauzauskie P., Huang J.X., Yang P.D. "Direct photonic-plasmonic coupling and routing in single nanowires" *Proceedings of the National Academy of Sciences of The United States of America* **2010**, 106, 21045.
4. **Yan R.X.**, Gargas, D., Yang P.D. "Nanowire photonics" *Nature Photonics* **2010**, 3, 569.
5. Huo, Z. Y., Tsung, C.-K., Huang, W. Y., Fardy, M., **Yan, R. X.**, Zhang, X. F., Li, Y. D., Yang, P. D. "Self-Organized Ultrathin Oxide Nanocrystals" *Nano Letters* **2009**, *9*, 1260.
6. **Yan R.X.***, Liang W.J.*, Fan R. and Yang P.D. "Nanofluidic Diodes Based on Nanotube Heterojunctions." *Nano Letters* **2009**, 9, 3820.
7. Fan R., Seong S., **Yan R.X.** and Yang P.D. "Proton Transport in Mesoprous Slilca Thin Film", *Nature Materials* **2008***,* 7, 303.
8. Liang X., Wang X., Wang L.Y., **Yan R.X.**, Peng Q., Li Y.D. "Synthesis and characterization of ternary $NH_4Ln_2F_7$ (Ln = Y, Ho, Er, Tm, Yb, Lu) nanocages" *European Journal of Inorganic Chemistry* **2006**, 11, 2186
9. Wang L.Y., **Yan R.X.**, Hao Z.Y., Wang L., Zeng J.H., Bao H., Wang X., Peng Q. and Li Y.D. "Fluorescence resonant energy transfer biosensor based on upconversion-luminescent nanoparticles." *Angewandte Chemie-International Edition* **2005**, 44, 6054
10. Zeng J.H., Su J., Li Z.H., **Yan R.X.**, Li Y.D. "Synthesis and upconversion luminescence of hexagonal-phase $NaYF_4$:Yb, Er^{3+}, phosphors of controlled size and morphology" *Advanced Materials* **2005**, 17, 2119
11. **Yan R.X.,** Sun X.M., Wang X., Peng Q. and Li Y.D. "Crystal structures, anisotropic growth and optical properties - Controlled synthesis of Lanthanide Orthophosphate 1D-nanomaterials." *Chemistry-A European Journal* **2005**, 11, 2183.
12. **Yan R.X.** and Li Y.D. "Down/Up-conversion in Ln^{3+}-doped YF_3 nanocrystals." *Advanced Functional Materials* ***2005****,* 15, 763.
13. Wang H.Y., Wang R.J., Sun X.M., **Yan R.X.**, Li. Y.D. "Synthesis of red-luminescent Eu^{3+}-doped lanthanides compounds hollow spheres." *Materials Research Bulletin* **2005**, 40, 911.
14. Shi J.J., **Yan R.X.**, Zhu Y.F. and Zhang X.R. "Determination of NH_3 gas by combination of nanosized $LaCoO_3$ converter with chemiluminescence detector." *Talanta* **2003**,61, 157.